transactions of the ASME
Published Quarterly by
The American Society of
Mechanical Engineers
Volume 93 • Series C • Number 3
AUGUST 1971

journal of heat transfer

EDITED and PUBLISHED quarterly at the offices of The American Society of Mechanical Engineers, United Engineering Center, 345 E. 47th St., New York, N. Y. 10017. Cable address, "Mechaneer," New York. Second-class postage paid at New York, N. Y., and at additional mailing offices.

CHANGES OF ADDRESS must be received at Society headquarters seven weeks before they are to be effective. Please send old label and new address.

PRICES: To members, $15.00, annually; to nonmembers, $30.00. Single copies, $10.00 each. Add $1.50 for postage to countries outside the United States and Canada.

INDEXED by the Engineering Index, Inc.

257 **Efficient Solution Processes for Finite Element Analysis of Transient Heat Conduction** (69-WA/HT-32)
R. H. Gallagher and R. H. Mallett

264 **Heat Transfer to the Insulator Wall of a Linear MGD Accelerator** (69-WA/HT-53)
Robert A. Cochran and James A. Fay

271 **Calculation of Incompressible Turbulent Boundary Layers With Mass Transfer, Including Highly Accelerating Flows** (70-HT/SpT-19)
T. Cebeci and G. J. Mosinskis

281 **Highly Accelerated Compressible Laminar Boundary Layer Flows With Mass Transfer** (70-HT/SpT-34)
A. Wortman and A. F. Mills

290 **Forced Convection Heat Transfer From a Cylinder in Carbon Dioxide Near the Thermodynamic Critical Point** (70-HT/SpT-36)
J. R. Green and E. G. Hauptmann

297 **Laminar Film Condensation From a Steam-Air Mixture Undergoing Forced Flow Down a Vertical Surface** (71-HT-E)
V. E. Denny, A. F. Mills, and V. J. Jusionis

305 **Frequency Response of Pool Boiling Plants** (71-HT-A)
P. C. Chiu and K. L. Poon

316 **Discussion on previously published papers**

R. H. GALLAGHER
Professor of Civil Engineering,
Cornell University, Ithaca, N. Y.

R. H. MALLETT
Manager, Continuum Mechanics Research,
Bell Aerospace Co.,
Buffalo, N. Y.

Efficient Solution Processes for Finite Element Analysis of Transient Heat Conduction

Systematic procedures are presented for reducing the order of a matrix differential equation governing transient heat conduction in solids. Two principal aspects of this development are a condensation of the set of gridpoint temperature degrees of freedom using steady-state relations and the introduction of generalized (modal) temperature degrees of freedom to achieve a further reduction. These processes are illustrated in an elementary one-dimensional transient heat conduction problem.

A. Introduction

The matrix methods of analysis based upon finite element idealization originated within structural mechanics. Development of these finite element methods has led to powerful analysis tools for structures and to recognition of their applicability to the analysis of a wide range of problems in mathematical physics. The phenomena studied have included heat conduction [1–4],[1] various fluid flows [5–8], and rarefied gas dynamics [9].

Developments in finite element heat conduction are of particular interest because of the close interaction of thermal and stress analyses in the design of thermostructural hardware. Additionally, finite element heat conduction has intrinsic merit in its amenability to automation and its versatility as regards variations in configuration, sizing dimensions, material properties, boundary conditions, heat generation, and grid refinement.

The treatment of a given type of problem by the finite element method consists of two major component aspects: (1) the formulation of element relationships, and (2) the solution of the complete system. Early efforts [1–3] in finite element heat conduction theory established the theoretical basis and the form of the finite element representations. The relationships for finite element heat conduction, heat capacity, internal heat generation, boundary heat flux, and surrounding medium convection heating matrices have been delineated. These concepts have been transformed into explicit relationships for the many types of elements encountered in practice including one-dimensional, two-dimensional (triangular and quadrilateral), and three-dimensional (tetrahedron) shapes [10].

The second major aspect of finite element analysis, solution of the complete system, remains relatively unexplored. Yet realization of the potential of the method in engineering practice hinges importantly upon the existence of reliable and efficient solution procedures. Particular significance must be attached to solution efficiency as large numbers of time-dependent temperature degrees of freedom arise in consequence of the relative simplicity of an individual finite element.

Efficient solution of the matrix equation governing transient heat conduction is usually sought through careful definition of a numerical technique for direct integration. Herein, consideration is given to additional approaches to improved solution efficiency. Systematic procedures are presented for reducing the order of the set of equations.

The effort required to reduce the governing matrix equation tacitly restricts the applicability of reduction processes to problems requiring infrequent updating of material properties or geometry. Of course, applicability is also restricted to problems for which the analyst has sufficient insight to identify certain temperature degrees of freedom as superfluous over intervals of the total time.

Consideration of reduction processes is extended herein to include the analysis of complete systems as assemblies of component substructures. Substructuring simplifies the specification of a system because it is efficient to confirm a large quantity of data via subsets. Calendar time can be shortened by the distribution of the subsets to several analysts for simultaneous preparation. Additional benefits of the data management type that are derived from substructuring are discussed in reference [11]. Of particular interest in the present context is the definition of substructures so as to facilitate invoking the procedures for reduction of the order of the governing matrix differential equation.

The component aspects of the finite element heat conduction analysis described herein constitute a computational flow from

[1] Numbers in brackets designate References at end of paper.

Contributed by the Heat Transfer Division and presented at the Winter Annual Meeting, Los Angeles, Calif., November 16–20, 1969, of The American Society of Mechanical Engineers. Manuscript received by the Heat Transfer Division July 16, 1969. Paper No. 69-WA/HT-32.

the basic data (e.g., material properties) through to the calculation of temperatures, i.e.,

(*a*) "Consistent" formulation of individual element thermal matrices, based upon variational assumed mode concepts.

(*b*) Definition of major segments of the system as "substructures."

(*c*) "Condensation" of the substructure degrees of freedom using steady-state relations.

(*d*) Application of "component mode synthesis" [12–13] involving modal analysis of the substructures.

(*e*) Connection of substructures in construction of the complete analytical model.

Steps *a* and *b* are discussed in the following two sections. Then, detailed development of steps *c* and *d* is accomplished and an outline is given of step *e*. Finally, numerical solutions are presented for an elementary example to illustrate the principal procedures for reduction of the matrix differential equation governing transient heat conduction.

B. Basic Equations

Development of the matrix differential equation governing finite element heat conduction may proceed in several ways [1, 10, 14]. Approach through "temperature potentials" which are analogous to the potential and kinetic energies of structural mechanics is the most systematic and leads to sparse, symmetric matrices. Adopting this approach, we begin by approximating the temperature field $\Theta(\{x\}, t)$ over a finite element with functions of the form

$$\Theta(\{x\}, t) = \sum_{m=1}^{M} f_m(\{x\})\theta_m(t) = \llcorner f \lrcorner \{\theta\}_e \tag{1}$$

where the $f_m\{x\}$ are "shape functions" and $\theta_m(t)$ are the finite element cornerpoint temperature values that are to be determined.

The heat conductivity and heat capacity "potentials" corresponding to the assumed functions of equation (1) take the form [14]

$$\Phi_{ke} = \int_v \frac{1}{2}\,\theta_m \frac{\partial f_m}{\partial x_i}\, k_{ij} \frac{\partial f_n}{\partial x_j}\,\theta_n dV + \int_s \theta_m f_m \bar{q} dS \qquad m, n = 1, 2, \ldots, M \tag{2}$$

and

$$\Phi_{ce} = \int_v \frac{1}{2}\,\dot{\theta}_m f_m \rho c f_n \dot{\theta}_n dV \qquad m, n = 1, 2, \ldots, M \tag{3}$$

where Φ_{ke} is the volume (V) conduction potential, k_{ij} is the conductivity tensor and $\bar{q}$ is the element boundary (S) heat flux. Equation (3) is the heat capacity potential (Φ_{ce}) which is dependent upon the density ρ and the specific heat capacity c. The standard summation convention on repeated indices is tacitly assumed in equations (2) and (3).

The matrix forms of the finite element potential functions follow immediately from equations (2) and (3), i.e.,

$$\Phi_{ke} = \tfrac{1}{2}\llcorner \theta \lrcorner_e [K]_e \{\theta\}_e - \llcorner \theta \lrcorner_e \{Q\}_e \tag{4}$$

$$\Phi_{ce} = \tfrac{1}{2}\llcorner \dot{\theta} \lrcorner_e [C]_e \{\dot{\theta}\}_e \tag{5}$$

where

$$[K_{mn}]_e = \int_v \frac{\partial f_m}{\partial x_i}\, k_{ij} \frac{\partial f_n}{\partial x_j}\, dV \qquad m, n = 1, 2, \ldots, M \tag{6}$$

$$[C_{mn}]_e = \int_v f_m \rho c f_n dV \qquad m, n = 1, 2, \ldots, M \tag{7}$$

$$\{Q_m\}_e = \int_s -f_m \bar{q} dS \qquad m = 1, 2, \ldots, M \tag{8}$$

and the subscript e denotes reference to a single finite element.

Expression of the finite element temperature potentials in terms of cornerpoint temperature degrees of freedom permits assembly of the individual finite element representations to form a representation for the complete, connected system [14]. This operation may be indicated as

$$\Phi_k = \sum_{e=1}^{r} \Phi_{ke} = \frac{1}{2}\llcorner \theta \lrcorner [K] \{\theta\} - \llcorner \theta \lrcorner \{Q\} \tag{9}$$

$$\Phi_c = \sum_{e=1}^{r} \Phi_{ce} = \frac{1}{2}\llcorner \dot{\theta} \lrcorner [C] \{\dot{\theta}\} \tag{10}$$

in which $\{\theta\}$ denotes the set of gridpoint temperature degrees of freedom for the complete system. The $[K]$, $[C]$, and $\{Q\}$ are the corresponding heat conduction, heat capacity, and heat flux matrices.

The stationary conditions of this variational approach to finite element heat conduction are given by [10]

$$\frac{\partial \Phi_k}{\partial \theta_n} + \frac{\partial \Phi_c}{\partial \dot{\theta}_n} = 0 \qquad n = 1, 2, \ldots, M \tag{11}$$

Nomenclature

$[C]$ = heat capacity matrix
e = subscript denoting reference to a typical finite element
E = subscript denoting reference to a typical substructure
f_m = assumed mode shape of temperature distribution within a finite element
$\{g\}$ = modal amplitude temperature variables
$[K]$ = heat conduction matrix
M = number of gridpoint temperature variables
$\bar{q}$ = prescribed boundary heat flux
$\{q\}$ = final, complete set of temperature variables
$\{Q\}$ = boundary heat flux matrix
r = number of finite elements
R = number of substructures
$[\gamma_{\mathrm{I}}]$, $[\gamma_{\mathrm{II}}]$ = matrices for transformations of variables, equations (28) and (32)
$[\tilde{\Gamma}]$, $[\hat{\Gamma}]$ = matrices for transformations of variables, equations (19) and (33)
$\{\theta\}$ = complete set of gridpoint temperature variables
$\{\tilde{\theta}\}$ = subset of $\{\theta\}$ designated as essential
θ_m = gridpoint temperature intensity associated with assumed mode shape f_m
$\{\tilde{\theta}_\alpha\}$ = temperature variables at gridpoints on the boundary of a substructure
$\{\tilde{\theta}_\beta\}$ = temperature variables at gridpoints interior to a substructure
$\{\tilde{\theta}_{\beta\mathrm{I}}\}$ = interior temperature contribution due to boundary temperature variations
$\{\tilde{\theta}_{\beta\mathrm{II}}\}$ = interior temperature contribution of characteristic functions taken with boundary temperature variation suppressed
$\Theta(\{x\}, t)$ = temperature distribution with spatial dependence $\{x\}$ and temporal dependence t
Φ_c = heat capacity pseudo potential
Φ_k = heat conduction pseudo potential

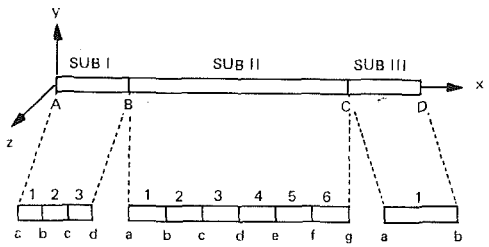

Fig. 1 Division into substructures

Invoking these conditions on the potentials of equations (9) and (10) leads to the matrix differential equation governing transient heat conduction, i.e.,

$$[C]\{\dot{\theta}\} + [K]\{\theta\} = \{Q\} \tag{12}$$

The character of these equations is noteworthy. They will be symmetric in consequence of the forms of the temperature potentials and sparsely populated due to the inclusion in each equation of only the temperatures at cornerpoints of elements which meet at the gridpoint in question. Within these limits, however, there is a high degree of coupling between the coefficients of the temperatures. Furthermore, it may be difficult to achieve a narrow banding of the matrix coefficients in representing a geometrically complex system.

C. Substructuring

The second of the two principal processes presented for reduction of the set of temperature degrees of freedom involves a modal analysis which is generalized so as to accommodate substructuring. Substructuring is the division of the complete system into component groupings of finite elements. This is illustrated in Fig. 1 which discloses the breakdown of the elementary one-dimensional example problem into three segments (substructures) designated Sub I, Sub II, and Sub III.

Generation and assembly of the finite element representations of equations (4) and (5) for each substructure in the manner of equations (9) and (10) leads to substructure potential functions expressible, typically, as

$$\Phi_{kE} = \tfrac{1}{2}\llcorner\theta\lrcorner_E[K]_E\{\theta\}_E - \llcorner\theta\lrcorner_E\{Q\}_E \tag{13}$$

and

$$\Phi_{cE} = \tfrac{1}{2}\llcorner\dot{\theta}\lrcorner_E[C]_E\{\dot{\theta}\}_E \tag{14}$$

where the subscript E denotes reference to a single substructure. Such substructure representations are essentially "super-elements" that, upon further assembly in the manner of equations (9) and (10), yield the objective potential expressions for the complete system, i.e.,

$$\Phi_k = \sum_{E=1}^{R} \Phi_{kE} = \frac{1}{2}\llcorner\theta\lrcorner[K]\{\theta\} - \llcorner\theta\lrcorner\{Q\} \tag{15}$$

and

$$\Phi_c = \sum_{E=1}^{R} \Phi_{cE} = \frac{1}{2}\llcorner\dot{\theta}\lrcorner[C]\{\dot{\theta}\} \tag{16}$$

Motivation for substructuring derives from various considerations as was discussed in section A. The reduction in order of the matrix differential equation for heat conduction which may be achieved through the component mode synthesis [12] of section E provides further motivation for substructuring.

D. Condensation

The basic premise of condensation is that certain temperature degrees of freedom of the system are superfluous over substantial time intervals of the complete time integration. This situation often arises in transient heat conduction in the aftermath of a severe thermal disturbance such as a heat pulse. Another example is the use of a common finite element idealization for thermal and stress analyses which results in gridpoint temperature degrees of freedom that are superfluous to the thermal analysis.

Condensation assumes that the temperature variation across superfluous gridpoints can be closely approximated by steady-state variation. Accordingly, the condensation proceeds by partitioning the heat conduction potential into essential $\{\theta_\alpha\}$ and superfluous $\{\theta_\beta\}$ subsets of temperature degrees of freedom to obtain

$$\Phi_k = \frac{1}{2}\llcorner\llcorner\theta_\alpha\lrcorner, \llcorner\theta_\beta\lrcorner\lrcorner \begin{bmatrix} [K_{\alpha\alpha}], [K_{\alpha\beta}] \\ [K_{\alpha\beta}]^T, [K_{\beta\beta}] \end{bmatrix} \begin{Bmatrix} \{\theta_\alpha\} \\ \{\theta_\beta\} \end{Bmatrix} - \llcorner\llcorner\theta_\alpha\lrcorner, \llcorner\theta_\beta\lrcorner\lrcorner \begin{Bmatrix} \{Q_\alpha\} \\ \{Q_\beta\} \end{Bmatrix} \tag{17}$$

Invoking the stationary conditions for steady-state response yields

$$\begin{bmatrix} [K_{\alpha\alpha}], [K_{\alpha\beta}] \\ [K_{\alpha\beta}]^T, [K_{\beta\beta}] \end{bmatrix} \begin{Bmatrix} \{\theta_\alpha\} \\ \{\theta_\beta\} \end{Bmatrix} = \begin{Bmatrix} \{Q_\alpha\} \\ \{Q_\beta\} \end{Bmatrix} \tag{18}$$

The submatrix $\{Q_\beta\}$ is neglected in solution of this relation for the subset of superfluous temperature degrees of freedom $\{\theta_\beta\}$ to obtain the desired condensing transformation, i.e.,

$$\begin{Bmatrix} \{\theta_\alpha\} \\ \{\theta_\beta\} \end{Bmatrix} = \begin{bmatrix} \ulcorner I \lrcorner \\ -[K_{\beta\beta}]^{-1}, [K_{\alpha\beta}]^T \end{bmatrix} \{\theta_\alpha\} \equiv [\tilde{\Gamma}]\{\tilde{\theta}\} \tag{19}$$

The introduction of this condensation transformation, $[\tilde{\Gamma}]$, into the matrix model given for the system in equations (15) and (16) yields

$$\Phi_k = \tfrac{1}{2}\llcorner\tilde{\theta}\lrcorner[\tilde{K}]\{\tilde{\theta}\} - \llcorner\tilde{\theta}\lrcorner\{\tilde{Q}\} \tag{20}$$

and

$$\Phi_c = \tfrac{1}{2}\llcorner\dot{\tilde{\theta}}\lrcorner[\tilde{C}]\{\dot{\tilde{\theta}}\} \tag{21}$$

where

$$[\tilde{K}] = [\tilde{\Gamma}]^T[K][\tilde{\Gamma}] \tag{22}$$

$$[\tilde{C}] = [\tilde{\Gamma}]^T[C][\tilde{\Gamma}] \tag{23}$$

$$\{\tilde{Q}\} = [\tilde{\Gamma}]^T\{Q\} \tag{24}$$

Equation (24) accounts for the heat flux submatrix $\{Q_\beta\}$ by the application of "equivalent" heat flux contributions at the gridpoints retained $\{\tilde{\theta}\}$.

The above procedure has been applied to problems in structural dynamics [15, 16] and, more recently, structural stability [17, 18]. Its use in transient heat conduction is illustrated in the elementary example problem of section G.

E. Component Mode Synthesis

The previous section advanced a condensation procedure based upon steady-state relationships in which essential gridpoint temperature degrees of freedom were retained. At this point, an additional reduction procedure based upon modal analysis concepts is considered. The modal analysis is presented in a generalized way so as to accommodate substructuring. This reduction process, unlike the condensation procedure, accounts for the transient influence of the specific heat capacity potential and introduces generalized (modal) temperature degrees of freedom. This procedure, termed component mode synthesis in structural dynamics, was pioneered by Hurty [12] but simplifications introduced in reference [13] are incorporated in the present development.

Gridpoint temperature degrees of freedom on the boundary of a substructure, $\{\tilde{\theta}_\alpha\}$, must be retained for the purpose of con-

nection with other portions of the structure or boundaries. However, the temperature degrees of freedom associated with gridpoints in the interior of a substructure $\{\tilde{\theta}_\beta\}$, are candidates for elimination and the temperature potentials of equations (20) and (21) are partitioned accordingly to obtain

$$\Phi_k = \frac{1}{2} \llcorner\!\llcorner \tilde{\theta}_\alpha \lrcorner, \llcorner \tilde{\theta}_\beta \lrcorner\!\lrcorner \begin{bmatrix} [\tilde{K}_{\alpha\alpha}], & [\tilde{K}_{\alpha\beta}] \\ [\tilde{K}_{\alpha\beta}]^T, & [\tilde{K}_{\beta\beta}] \end{bmatrix} \begin{Bmatrix} \{\tilde{\theta}_\alpha\} \\ \{\tilde{\theta}_\beta\} \end{Bmatrix} - \llcorner\!\llcorner \tilde{\theta}_\alpha \lrcorner, \llcorner \tilde{\theta}_\beta \lrcorner\!\lrcorner \begin{Bmatrix} \{\tilde{Q}_\alpha\} \\ \{\tilde{Q}_\beta\} \end{Bmatrix} \quad (25)$$

and

$$\Phi_c = \frac{1}{2} \llcorner\!\llcorner \dot{\tilde{\theta}}_\alpha \lrcorner, \llcorner \dot{\tilde{\theta}}_\beta \lrcorner\!\lrcorner \begin{bmatrix} [\tilde{C}_{\alpha\alpha}], & [\tilde{C}_{\alpha\beta}] \\ [\tilde{C}_{\alpha\beta}]^T, & [\tilde{C}_{\beta\beta}] \end{bmatrix} \begin{Bmatrix} \{\dot{\tilde{\theta}}_\alpha\} \\ \{\dot{\tilde{\theta}}_\beta\} \end{Bmatrix} \quad (26)$$

Now, the subset of temperatures at the interior gridpoints $\{\tilde{\theta}_\beta\}$ is approximated by the sum of two contributions, i.e.,

$$\{\tilde{\theta}_\beta\} = \{\tilde{\theta}_{\beta\mathrm{I}}\} + \{\tilde{\theta}_{\beta\mathrm{II}}\} \quad (27)$$

The first contribution, $\{\tilde{\theta}_{\beta\mathrm{I}}\}$ is derived as the steady-state temperature variations over the interior that are produced by variations in substructure boundary temperature values $\{\tilde{\theta}_\alpha\}$. The complementary second contribution, $\{\tilde{\theta}_{\beta\mathrm{II}}\}$, is derived from a modal analysis of the transient system defined by the complete suppression of boundary temperature variations.

The definition of $\{\tilde{\theta}_{\beta\mathrm{I}}\}$ in terms of interface temperatures $\{\tilde{\theta}_\alpha\}$ is readily established via steady-state considerations as in the condensation of section D, i.e.,

$$\{\tilde{\theta}_{\beta\mathrm{I}}\} = -[\tilde{K}_{\beta\beta}]^{-1}[\tilde{K}_{\alpha\beta}]^T\{\tilde{\theta}_\alpha\} \equiv [\gamma_\mathrm{I}]\{\tilde{\theta}_\alpha\} \quad (28)$$

It is to be noted that this dependence of $\{\tilde{\theta}_{\beta\mathrm{I}}\}$ upon $\{\tilde{\theta}_\alpha\}$ results in an approximate treatment of the heat fluxes $\{\tilde{Q}_\beta\}$.

The temperature contributions relative to the interface, $\{\tilde{\theta}_{\beta\mathrm{II}}\}$, are constructed of characteristic mode shapes for a system wherein the steady-state distribution determined from interface temperatures is regarded as a datum. Applying equation (11) to the governing potentials of equations (20) and (21) under this assumption (i.e., $\{\tilde{\theta}_\alpha\} \equiv \{0\}$) yields a matrix equation of reduced order, say N, as

$$[\tilde{C}_{\beta\beta}]\{\dot{\tilde{\theta}}_{\beta\mathrm{II}}\} + [\tilde{K}_{\beta\beta}]\{\tilde{\theta}_{\beta\mathrm{II}}\} = \{\tilde{Q}_\beta\} \quad (29)$$

Assumption of a solution to the homogeneous part of the form

$$\{\tilde{\theta}_{\beta\mathrm{II}}\} = \sum_{j=1}^{N} \{\psi\}_j e^{-\lambda_j t} \quad (30)$$

leads to a characteristic value problem of the form

$$[\tilde{K}_{\beta\beta}]^{-1}[\tilde{C}_{\beta\beta}]\{\psi\} = +\frac{1}{\lambda}\{\psi\} \quad (31)$$

A modal analysis of equation (31) to obtain η characteristic values λ_j and vectors $\{\psi\}_j$ ($\eta \leqslant N$) yields the objective explicit expression for the $\{\tilde{\theta}_{\beta\mathrm{II}}\}$ in terms of characteristic modes and generalized (modal) temperature degrees of freedom $\{g\}$, i.e.,

$$\{\tilde{\theta}_{\beta\mathrm{II}}\} = [\{\psi\}_1, \{\psi\}_2, \ldots, \{\psi\}_\eta]\{g\} \equiv [\gamma_\mathrm{II}]\{g\} \quad (32)$$

The objective transformation of component mode synthesis may now be constructed in accord with equations (27), (28), and (32) to obtain

$$\begin{Bmatrix} \{\tilde{\theta}_\alpha\} \\ \{\tilde{\theta}_\beta\} \end{Bmatrix} = \begin{bmatrix} \lceil I \rfloor, & [0] \\ [\gamma_\mathrm{I}], & [\gamma_\mathrm{II}] \end{bmatrix} \begin{Bmatrix} \{\tilde{\theta}_\alpha\} \\ \{g\} \end{Bmatrix} \equiv [\hat{\Gamma}]\{q\} \quad (33)$$

The introduction of this transformation into the potential functions of equations (20) and (21) accomplishes the expression of these potential functions in terms of component modes, i.e.,

$$\Phi_k = \tfrac{1}{2}\llcorner q \lrcorner[\hat{K}]\{q\} - \llcorner q \lrcorner\{\hat{Q}\} \quad (34)$$

$$\Phi_c = \tfrac{1}{2}\llcorner \dot{q} \lrcorner[\hat{C}]\{q\} \quad (35)$$

where

$$[\hat{K}] = [\hat{\Gamma}]^T[\tilde{K}][\hat{\Gamma}] \quad (36)$$

$$[\hat{C}] = [\hat{\Gamma}]^T[\tilde{C}][\hat{\Gamma}] \quad (37)$$

$$\{\hat{Q}\} = [\hat{\Gamma}]^T\{\tilde{Q}\} \quad (38)$$

Because of the form of the transformation matrix of equation (33) and the orthogonality of the substructure normal modes, the matrices of equations (36) and (37) assume particularly simple forms. Restoring the partitioning into the subsets of boundary $\{\tilde{\theta}_\alpha\}$ and generalized $\{g\}$ temperature degrees of freedom evident in equation (33) clarifies the special character of final heat conduction and heat capacity matrices, i.e.,

$$[\hat{K}] = \begin{bmatrix} [\hat{K}_{\alpha\alpha}], & [0] \\ [0], & \lceil \hat{K}_{\beta\beta} \rfloor \end{bmatrix} \quad (39)$$

$$[\hat{C}] = \begin{bmatrix} [\hat{C}_{\alpha\alpha}], & [\hat{C}_{\alpha\beta}] \\ [\hat{C}_{\alpha\beta}]^T, & \lceil \hat{C}_{\beta\beta} \rfloor \end{bmatrix} \quad (40)$$

Reduction in the order of the matrix differential equation results from this component mode synthesis procedure when less than the complete set of characteristic modes (i.e., $\eta < N$) are incorporated in the modal transformation of equation (32). For most problems a considerable reduction can be realized at least over portions of the total integration time.

F. Complete System

Section C described the concept of substructuring and, although the subscript E denoting a typical substructure was dropped for reasons of convenience, sections D and E presented the condensation and modal analysis procedures with reference to a typical substructure. Assembly of the resulting reduced expressions for the heat conduction and heat capacitance potentials of equations (34) and (35) proceeds in accord with equations (15) and (16) to form representations for systems comprised of more than one substructure.

It is noteworthy that application of the condensation and modal analysis procedures can be repeated for the assembled structure to achieve a further reduction of the matrix differential equation governing transient heat conduction in the complete system. Explicit consideration is given to the steps of such an extended process in reference [19], although the principal aspects remain the condensation and component mode synthesis procedures.

G. Numerical Results

Baseline Results. The one-dimensional problem chosen to illustrate the matrix reduction processes is shown in Fig. 1 as a unit area of a slab which is bounded by planes $X = 0$ and $X = L$ and is infinite in extent in the Y and Z directions. The temperature of the slab is initially everywhere zero. For $t > 0$ a constant heat flux Q is introduced through the surface $X = 0$ while the surface $X = L$ is maintained at zero temperature. The transient temperature distribution is desired for the case of an insulation material of diffusivity

$$d = 0.000432 \text{ in}^2/\text{sec}$$

This example problem is recommended by its simplicity and the availability of a formal infinite-series solution [20]. While the simplicity of the problem prevents a compelling demonstration of the benefits of the reduction processes, this deficiency is accepted in preference for the clear and concise illustration of the principal reduction procedures.

Approach to the problem is made, as shown in Fig. 1, by a division into three substructures of lengths (L_I/L) = 0.2, (L_II/

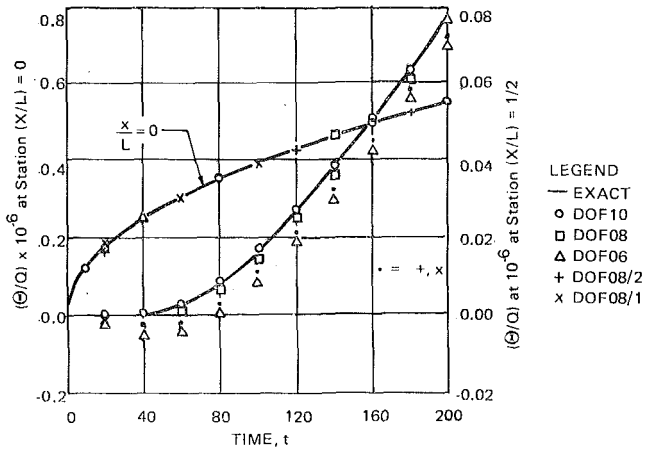

Fig. 2 Short time profiles; Θ/Q vs. t

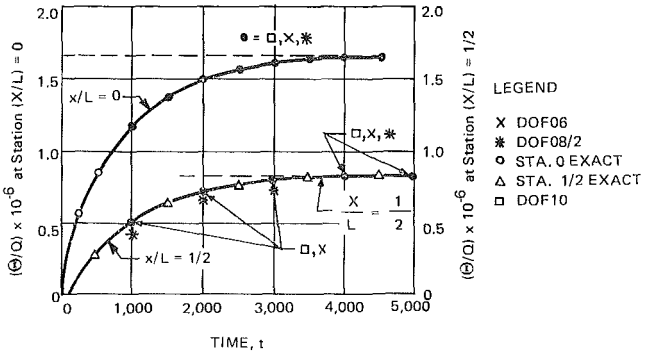

Fig. 3 Long time profiles; Θ/Q vs. t

Table 1 Representative numerical results

		$(\Theta/Q) \times 10^{-6}$					
		EXACT	DOF10	DOF08	DOF06	DOF08/2	DOF08/1
t	20	0.173	0.173	0.173	0.173	0.173	0.173
X/L	0.0						
t	20	0.0	0.0	0.0	-0.001	-0.001	-0.001
X/L	0.5						
t	200	0.553	0.552	0.550	0.545	0.550	0.549
X/L	0.0						
t	200	0.077	0.076	0.074	0.069	0.071	0.070
X/L	0.5						

Table 2 System eigenvalues

EIGEN-VALUE NO.	CASE IDENTIFICATION				
	DOF10	DOF08	DOF06	DOF08/2	DOF08/1
1	0.00107	0.00107	0.00107	0.00107	0.00107
2	0.009	0.009	0.010	0.009	0.010
3	0.028	0.030	0.034	0.030	0.035
4	0.060	0.065	0.078	0.074	0.084
5	0.110	0.144		0.149	
6	0.182	0.186			
7	0.283		0.347*		0.356*
8	0.414	0.467*		0.415*	
9	0.531*				
10	1.031*	1.023*	0.990*	1.005*	0.985*

* These values were obtained last in an eigenvalue routine based upon sweeping and are of questionable accuracy.

$L) = 0.6$, and $(L_{III}/L) = 0.2$. The breakdown of the substructures into finite elements is taken as 3, 6, and 1, respectively.

The first predictions of transient temperature behavior were made without reduction of the 10×10 matrix differential equation which results for the complete system. This case is designated "DOF10." Comparisons of the results with the formal solution of reference [20] are given in Figs. 2, 3, and 4.

Fig. 2 shows that the short time temperature profiles of the heated surface, $(X/L) = 0$, and the midthickness, $(X/L) = 0.5$, are predicted with negligible error. The accuracy of the finite-element predictions of these same behavior quantities over the long period is illustrated in Fig. 3. Specific numerical results are recorded in Table 1.

Complementary results for this same case (DOF10) are given in Fig. 4 which compares the thickness temperature profiles at arbitrarily selected points in time, $t = 20$ and $t = 200$. The high level of accuracy is clear.

A modal analysis of the matrix differential equations was performed to establish a further basis for the comparison of the results of case DOF10 with subsequent cases with reduced sets of degrees of freedom. The equation employed was

$$-\lambda[C]\{\psi\} + [K]\{\psi\} = \{0\} \tag{41}$$

The complete set of 10 characteristic values, λ_j, are recorded in Table 2.

Condensation Results. Attention, as regards the elimination of degrees of freedom, is focused upon substructure Sub II in the results that follow. Evaluation of the results is made on the basis of the behavior of the complete system in all cases.

The set of temperature degrees of freedom in the idealization of Sub II is shown in Fig. 1 to be

$$\{q\}_{II}^T = \llcorner q_B, q_b, q_c, q_d, q_e, q_f, q_C \lrcorner_{II} \tag{42}$$

The temperature degrees of freedom q_B and q_C are associated with the boundary gridpoints of Sub II and must be retained for the purpose of connection to form the complete system. The condensation procedure was applied to obtain two cases characterized by reduced numbers of gridpoint temperature degrees of freedom within Sub II. Firstly, a case designated DOF08 was obtained by the choice of the q_c and q_e temperature degrees of freedom in Fig. 1 as superfluous to obtain the condensed set of independent temperature degrees of freedom

$$\{q\}_{II}^T = \llcorner q_B, q_b, q_d, q_f, q_C \lrcorner_{II} \tag{43}$$

Case DOF06 was constructed by the further designation of q_b and q_f in Fig. 1 as superfluous to obtain

$$\{q\}_{II}^T = \llcorner q_B, q_d, q_C \lrcorner_{II} \tag{44}$$

These specifications of cases DOF10, DOF08, and DOF06 are summarized in Table 3. As noted in Table 3, case DOF08 and case DOF06 represent reductions in the number of degrees of freedom within Sub II to 60 percent and 20 percent, respectively. Yet the loss in accuracy is barely perceptible in the predicted time and thickness profiles plotted in Figs. 2, 3, and 4 and the representative numerical values in Table 1.

The characteristic values determined from modal analyses of cases DOF08 and DOF06 facilitate quantitative evaluation of the equivalence of these cases with the uncondensed case DOF10. These results, shown in Table 2, exhibit a close approximation of the lower eigenvalues. The predictions of the higher characteristic values are less accurate and, of course, some are absent as a result of the condensation. This points out the

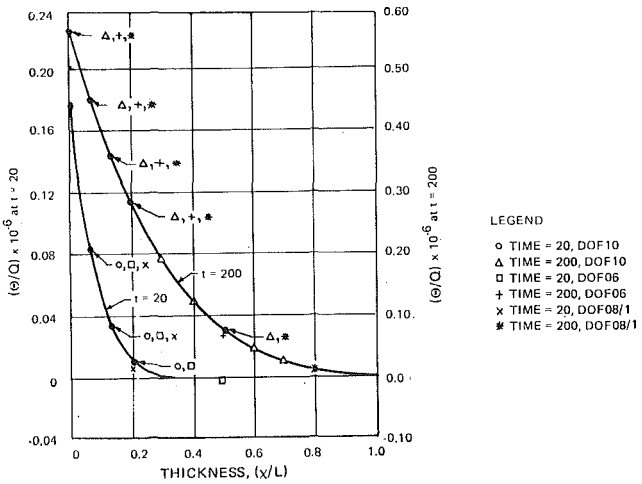

Fig. 4 Thickness profiles; Θ/Q vs. X/L

inevitable degradation of the analytical model which occurs as a consequence of the elimination of degrees of freedom. Thus, some insight into the behavior of the system is essential to the selection of those degrees of freedom to be eliminated by condensation in order to maintain the desired accuracy.

Component Mode Synthesis Results. Two further cases were considered to illustrate the component mode synthesis procedure of section E. Beginning from the condensed matrices of Sub II for case DOF08, with the degrees of freedom

$$\{q\}_{II}{}^T = \lfloor q_B, q_b, q_d, q_f, q_c \rfloor_{II} \tag{45}$$

a modal analysis was conducted in accord with section E to obtain the following alternative set of degrees of freedom

$$\{q\}_{II}{}^T = \lfloor q_B, q_C, g_1, g_2, g_3 \rfloor_{II} \tag{46}$$

The g_1, g_2, and g_3 are the generalized temperature degrees of freedom associated with the characteristic vectors of Sub II.

Predictions of the response of the complete system retaining all three generalized degrees of freedom were the same as case DOF08. Results are presented herein for two cases of reduced degrees of freedom designated DOF08/2 and DOF08/1 wherein only two and one generalized degrees of freedom were retained. The specification of these component mode synthesis cases is summarized in Table 4.

The validity of these analyses is clear in the representative results shown in Figs. 2, 3, and 4. More quantitative comparisons are made in Tables 1 and 2. In the latter, Table 2, the more comprehensive characteristic value comparison substantiates the equivalence of the models indicated in the temperature profiles of Figs. 2, 3, and 4.

H. Summary and Conclusions

Use of the condensation procedure described herein presumes that, at some point in space and time, the finite-element model of the system includes more than enough gridpoint degrees of freedom to predict the conduction of heat. Given this circumstance, the condensation procedure provides for steady-state variation of temperature in the region of gridpoints designated as superfluous thereby eliminating the temperatures at these gridpoints as independent variables. Consequently, the order of the matrix equation governing heat conduction in the system is reduced. This, in turn, reduces the computational effort of the numerical integration.

While the reasons for the condensation and the calculation itself are clear, the appropriate choice of what variables are superfluous at what times is less straightforward. The choice is largely a matter of judgment. The considerations are entirely analogous to those of setting up a gridwork initially. In using

Table 3 Sub II condensation cases

CASE IDENT.	% SUB II DOF* RETAINED	SUB II DOF* RETAINED
DOF10	100%	q_b, q_c, q_d, q_e, q_f
DOF08	60%	q_b, q_d, q_f
DOF06	20%	q_d

* DOF = degrees of freedom

Table 4 Sub II modal coordinate cases

CASE IDENT.	% SUB II DOF* RETAINED	SUB II DOF* RETAINED
DOF08/3	60%	g_1, g_2, g_3
DOF08/2	40%	g_1, g_2
DOF08/1	20%	g_1

* DOF = degrees of freedom

condensation, the analyst is given the opportunity to reconsider the definition of the gridwork in the light of the knowledge accumulated about the behavior. Also, as noted previously, condensation can be used to adapt gridworks created for some other purpose such as thermal stress analysis.

The remarks expressed with reference to condensation apply to the modal analysis of the component mode synthesis process as well. The proper selection of modes for retention is largely dependent upon experience and judgment. Nevertheless, this process offers, in the least, additional flexibility as decisions made at the outset can be modified at subsequent stages of the computation.

The foregoing results are taken to establish the procedural validity of the principal reduction processes presented. Further study is needed to establish guidelines for choosing what, and how many, temperature degrees of freedom can be reduced from a model without significantly compromising its accuracy. These questions imply a question of "when" which suggests a coordination of the reduction processes with the updating of material properties and the reference points for linearization of nonlinear boundary phenomena.

References

1 Nickell, R. E., and Wilson, E., "Application of the Finite Element Method to Heat Conduction Analysis," *Nuclear Engineering Design*, Vol. 4, No. 3, Oct. 1966, pp. 276–286.

2 Visser, W., "A Finite Element Method for the Determination of Non-Stationary Temperature Distribution and Thermal Deformations," *Proceedings of the (First) Air Force Conference on Matrix Methods in Structural Mechanics*, AFFDL TR 66-80, Nov. 1965.

3 Zienkiewicz, O., and Cheung, Y., "Finite Elements in the Solution of Field Problems," *The Engineer*, Sept. 24, 1965.

4 Fujino, T., and Ohsaka, J., "Approximate Studies in Linear, Coupled, Thermoelasticity," *Proceedings of the Second Air Force Conference on Matrix Methods in Structural Mechanics*, Dayton, Ohio, Oct. 1968.

5 Martin, H. C., "Finite Element Analysis of Fluid Flows," *Proceedings of the Second Air Force Conference on Matrix Methods in Structural Mechanics*, Dayton, Ohio, Oct. 1968.

6 Bug, G., and Blair, P., "Finite Element Solution of Flow Around a Two-Dimensional Discoid," paper presented at ASCE National Meeting, New Orleans, La., Feb. 1969.

7 Baker, A. J., "A Numerical Solution Technique for a Class of Two-Dimensional Problems in Fluid Dynamics Formulated with the Use of Discrete Elements," Bell Aerosystems Technical Note TCTN-1005, Jan. 1969.

8 VerHague, J., "A Numerical Method for Incompressible Vis-

cous Flow by Finite Elements," Bell Aerosystems Technical Report No. 2500-927007, May 1969.

9 Bramlette, T. T., and Mallett, R. H., "A Finite Element Solution Technique for the Boltzmann Equation," *Journal of Fluid Mechanics*, Vol. 24, Pt. 1, 1970, pp. 177–191.

10 Batt, J. R., "Formulation of Discrete Element Matrices for Heat Conduction Analysis," Bell Aerosystems Report No. 8500-937003, Aug. 1968.

11 Mallett, R. H., Braun, F. W., and Hunter, D. T., "Structural Analysis Practices for Large Scale Systems," presented at the Second Air Force Conference on Matrix Methods in Structural Mechanics, Dayton, Ohio, Oct. 1968.

12 Hurty, W., "Dynamic Analysis of Structural Systems Using Component Modes," *AIAA Journal*, Vol. 3, No. 4, Apr. 1965.

13 Craig, R. R., and Bampton, M. C., "Coupling of Substructures for Dynamic Analysis," *AIAA Journal*, Vol. 6, No. 7, July 1968.

14 Zienkiewicz, O., and Cheung, Y., *The Finite Element Method*, McGraw-Hill, New York, N. Y., 1968, chap. 10.

15 Guyan, R., "Reduction of Stiffness and Mass Matrices," *AIAA Journal*, Vol. 3, No. 2, Feb. 1965.

16 Uhrig, R., "Reduction of the Number of Unknowns in the Displacement Method Applied to Kinetic Problems," *J. Sound Vib.*, Vol. 4, No. 2, Feb. 1966.

17 Gallagher, R. H., and Yang, H. T. Y., "Elastic Instability Predictions for Doubly Curved Shells," *Proceedings of the Second Air Force Conference on Matrix Methods in Structural Mechanics*, Dayton, Ohio, Oct. 1968.

18 Braun, F. W., and Mallett, R. H., "Stress and Stability Analysis of the Apollo Short Stack Structure, Vol. I: Finite Element Analysis," Bell Aerosystems Technical Report No. 2373-941003, Dec. 1968.

19 Mallett, R. H., Jordan, S., and Batt, J. R., "Manageable Finite Element Models for Large Scale Structural Dynamics Analysis," Bell Aerosystems Technical Report No. 2500-941020, Sept. 1968.

20 Carslaw, H. S., and Jaeger, J. C., *Conduction of Heat in Solids*, Oxford University Press, 1959.

ROBERT A. COCHRAN[1]
Engineer,
Shell Pipe Line Corp.,
Houston, Texas.
Assoc. Mem. ASME

JAMES A. FAY
Professor,
Department of Mechanical Engineering,
Massachusetts Institute of Technology,
Cambridge, Mass. Mem. ASME

Heat Transfer to the Insulator Wall of a Linear MGD Accelerator

An experimental investigation of the rate of heat transfer to the insulator wall of a quasi-steady magnetogasdynamic accelerator is described. The experiments were conducted in an accelerator section attached to the end of a shock tube using argon as the test gas. The measurements are compared with a Hartmann boundary-layer analysis, which correlates the data within the experimental scatter. Based on this theory, estimates of the current shorting through the boundary layer and energy fluxes to the wall are made and compared with the accelerator's overall performance.

1 Introduction

The number of useful applications for high-energy gas streams has become large in recent years. Both for propulsion and laboratory experiments, one suggestion has been to accelerate gas streams using the electromagnetic $\mathbf{j} \times \mathbf{B}$ force. Experiments have been performed in this laboratory [1, 2][2] where currents as high as 50,000 amp were discharged through the gas stream produced by a shock tube in the presence of a transverse magnetic field of up to 2.5 Wb/m^2. It was found [2] that only a small percent of the total energy added to the flow in the accelerator was converted into an increase of kinetic energy. In addition, the increase in the momentum flux was small compared with the integral of the $\mathbf{j} \times \mathbf{B}$ forces throughout the volume of the accelerator. According to one theory [2], the low-velocity region in the Hartmann boundary layer was responsible for the poor performance.

On the insulating walls of the accelerator between the electrodes, a Hartmann boundary layer [3] forms. In this boundary layer the velocity is significantly lower than that in the free stream. The back emf, $\mathbf{u} \times \mathbf{B}$, is therefore less in the boundary layer. For this reason, a considerable amount of the drive current will run along the walls if the conductivity in the boundary layer is high enough. This could account for the poor momentum efficiencies since the $\mathbf{j} \times \mathbf{B}$ force in the boundary layer is balanced by viscous forces and does not increase the momentum of the gas. Similarly, this current will increase the enthalpy in the boundary layer, resulting in large heat fluxes to the wall and low kinetic-energy efficiencies. The purpose of this experiment was to investigate this theory by measuring the heat transfer to the side wall of the accelerator.

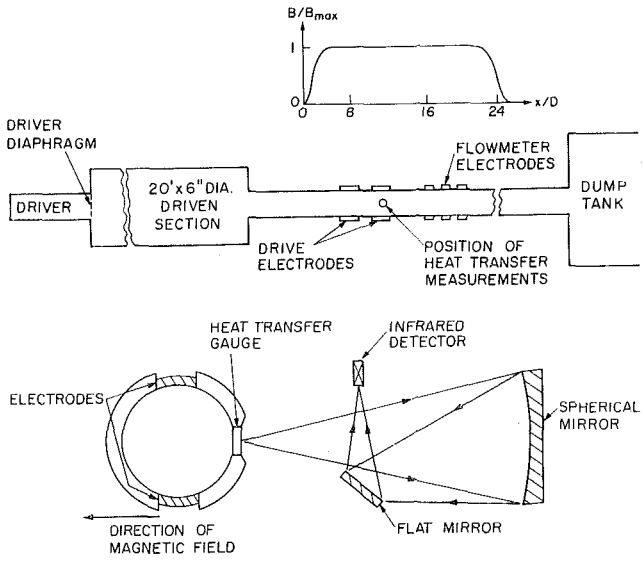

Fig. 1 Schematic of shock tube and heat-transfer system

The experiments were performed in the $1^1/_2$-in-dia accelerator section shown in Fig. 1, which was attached to the end of a 20-ft shock tube. This arrangement, described by Leonard and Fay [2], provides a steady flow of short duration. In the accelerator, the electrode current was limited to values less than 10,000 amp, and the applied transverse uniform magnetic field was kept below 1 Wb/m^2. This makes possible comparisons with simple theories which neglect induced magnetic fields and Hall effects. The heat-transfer measurements were made adjacent the drive electrodes and $1^1/_2$ tube diameters downstream

[1] Formerly Research Assistant, Department of Mechanical Engineering, Massachusetts Institute of Technology, Cambridge, Mass.

[2] Numbers in brackets designate References at end of paper.

Contributed by the Heat Transfer Division and presented at the Winter Annual Meeting, Los Angeles, Calif., November 16–20, 1969, of The American Society of Mechanical Engineers. Manuscript received by the Heat Transfer Division July 17, 1969; revised manuscript received August 10, 1970. Paper No. 69-WA/HT-53.

of the drive electrodes. The measurements were made with a high-speed infrared bolometer, which was proposed by Camac and Feinberg [4] and which is especially attractive for an experiment of this type where there are strong electric and magnetic fields present. It efficiently decouples the electromagnetic effects from those due to heat transfer.

The Hartmann boundary-layer theory, which is proposed in section 4 of this paper, was motivated from the observation that the rate of heat transfer to the wall was independent of time and distance downstream of the current discharge. Since the exact state of the gas is unknown, both an equilibrium and a nonequilibrium solution are considered and compared with the experimental data. In section 5, the accelerator performance is discussed in the light of the heat-transfer measurements.

2 Apparatus

Shock Tube. The combustion-driven shock tube used to produce the gas stream for the accelerator consisted of two sections of different diameters, Fig. 1. The accelerator was located in the smaller-diameter tube. This design allowed longer test times (about 200 μsec) in the accelerator than would have been possible in an ordinary shock tube, providing a quasi-steady flow. The driven section was evacuated by a mechanical pump and had an ultimate vacuum of 10 μ. For all experiments, argon was used as the driven gas at an initial pressure of 1 mm Hg.

Accelerator. The accelerator, Fig. 1, was made of linen-base phenolic tubing and had a $1^1/_2$-in. ID. Square slots were cut in the tubing to receive the brass electrodes which were $1^1/_2$ in. long and $^3/_4$ in. wide. There were two pairs of drive electrodes with a $^3/_4$-in. spacing between them. An internal flowmeter which consisted of three pairs of electrodes, $1^1/_2$ in. apart, was included in the accelerator $3^1/_4$ in. downstream of the drive electrodes to measure the back emf generated by the accelerated flow. From this measurement the average velocity of the flow at the exit of the accelerator was calculated [5]. The current source consisted of a 3000-μF capacitor bank connected as a lumped-parameter transmission line. The transmission line contained five identical units connected in parallel, each of which contained five 100-μF capacitors in parallel and one 0.55-μH inductor. This provided a current discharge from the electrodes which was constant for 200 μsec. The transverse magnetic field was provided by two field coils, one on each side of the shock tube. The magnetic-field profile in relation to the electrode positions is shown in Fig. 1. The current to energize the field coils was supplied by a 4800-μF capacitor bank. The LC circuit rang with a quarter-cycle time of 900 μsec providing a peak magnetic field of 0.9 Wb/m^2, which varied less than 10 percent in the 200-μsec test time. The time for triggering the capacitor banks was given by signals from ionization probes which indicate shock arrival times.

Heat-Transfer System. The heat-transfer system is shown schematically in Fig. 1. The system, described by Friedman and Fay [6], consists of three components: a carbon-coated sapphire gauge placed in contact with the hot gas, an optical system that gathers the radiant energy emitted from the gauge, and an infrared detector that responds to the incident radiation. The output of the detector was amplified by a 1A7 Tektronix preamplifier and displayed on a Tektronix 555 oscilloscope. The heat-transfer gauge consisted of a 0.020-in-thick sapphire window, $^3/_8$ in. in diameter, which was polished on one side and had a 600-grit finish on the other side. On the roughened side a coating of carbon, which was greater than 6000 Å thick, was deposited by the pyrolysis technique [7]. A 500-Å coating of aluminum was evaporated over the carbon coating to reflect radiation from the gas.

When the shock-heated gas passes the front of the gauge, a heat pulse penetrates the carbon coating and heats the carbon–sapphire interface. The detector monitors the temperature–time history of this interface which can be related to the heat transfer incident on the front surface of the gauge. Camac and Feinberg [4] have tabulated the interface temperature history for many heat-transfer–time dependences. For the present experiment two cases are of interest. For the situation where the rate of heat transfer to the wall q as a function of the time t takes the form $q = Q_c/t^{1/2}$, the corresponding wall temperature rise is

$$\Delta T = Q_c \cdot (\pi/k\rho c)^{1/2}, \tag{1}$$

where k, ρ, and c are properties of the crystal. Similarly, if the heat transfer to the wall is independent of time,

$$\Delta T = 2q(t/\pi k\rho c)^{1/2}. \tag{2}$$

In order to calculate Q_c and q from equations (1) and (2), it is necessary to find the absolute temperature rise of the interface as a function of the infrared-detector output voltage. This was done by a calibration experiment [8] similar to that described by Friedman and Fay [6]. Fay and Arnoldi [9] discuss the problem associated with the uncertainty in the value of the sapphire thermal conductivity in the vicinity of the carbon coating. This consideration is of great importance when this method of making heat-transfer measurements is used in experiments with test times on the order of microseconds. For the present experiment,

Nomenclature

A = tube cross-sectional area, m^2
B = magnetic field strength, Wb/m^2
c = electron concentration, kg/kg
c = specific heat, J/kg-deg C
D = diffusion coefficient, m^2/sec
d = tube inside diameter, m
E = electric field, v/m
H = dimensionless Hartmann number
I = total current delivered to the accelerator, amp
J = current flowing in the boundary layer per unit length, amp/m
j = current density, amp/m^2
k = thermal conductivity, w/deg C-m
L = length downstream of heat-transfer gauge, m
m = mass of an electron, kg
$\dot{m}$ = mass flow rate, kg/sec
p = pressure, N/m^2
p^* = sonic pressure, N/m^2
Q_c = convective heat-transfer coefficient, J/m^2-sec$^{1/2}$
q = rate of heat transfer per unit area, w/m^2
T = temperature, deg K
T_e = electron temperature, deg K
t = time after shock passage, sec
U_∞ = free-stream velocity, m/sec
u = velocity parallel to the wall, m/sec
V_0 = voltage across drive electrodes, v
V = free-stream velocity minus velocity parallel to wall, m/sec
v = velocity normal to the wall, m/sec
x, y, z = cartesian position coordinates, m
δ_H = Hartmann boundary-layer thickness
ϵ = ionization energy per ion-electron pair, J
η_{mom} = momentum efficiency
η_{KE} = kinetic energy efficiency
λ = gas thermal conductivity, w/deg C-m
λ_e = electron thermal conductivity, w/deg C-m
λ_r = total reactive thermal conductivity, w/deg C-m
λ^* = total reactive thermal conductivity minus electron thermal conductivity, w/deg C-m
μ = gas viscosity, kg/m-sec
ρ = density, kg/m^3
σ = electrical conductivity, moh/m

Subscripts

w = wall
∞ = free-stream
eq = equilibrium

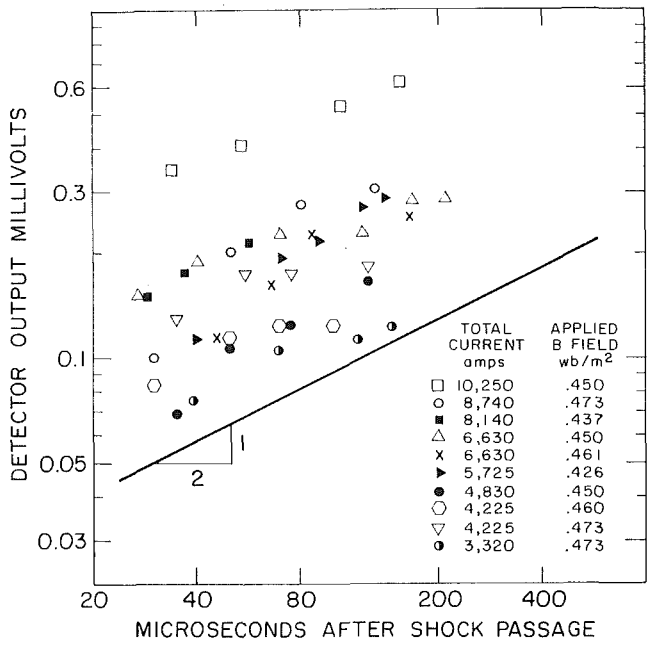

Fig. 2 Infrared detector's output history. Current discharge is from the downstream electrode pair.

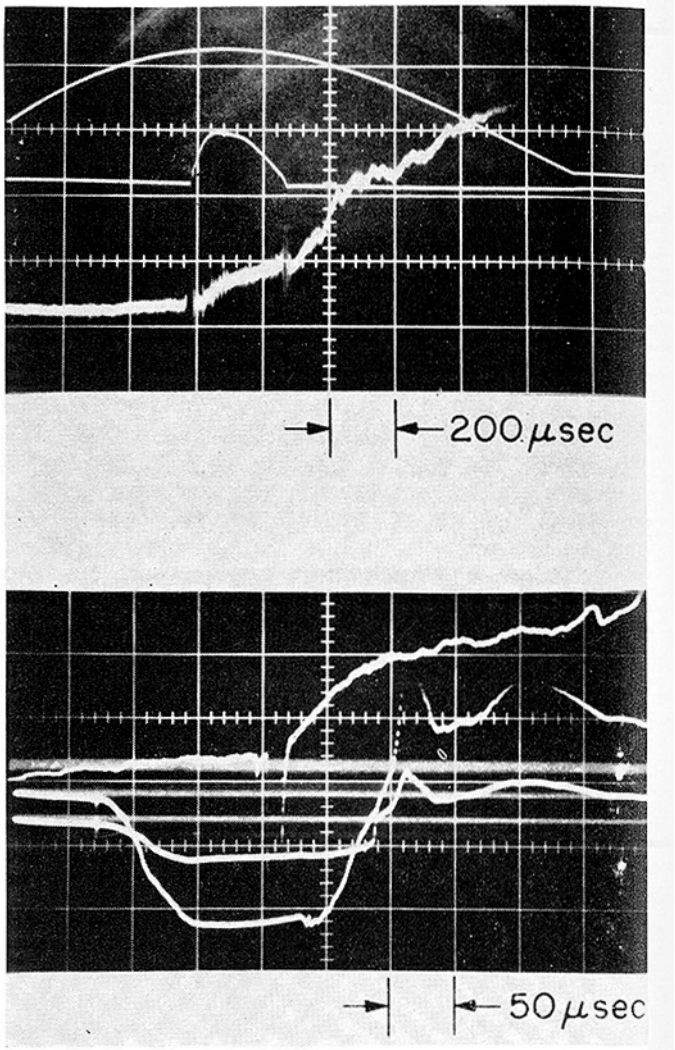

Fig. 3 Typical oscillograms from accelerated runs. Note parabolic rise in infrared detector's output. Top: (top curve) transverse magnetic field, 0.237 Wb/m²/cm; (center curve) total input current, 6030 amp/cm; (bottom curve) infrared detector output. Bottom: (top curve) exploded infrared detector output, 0.15 mv/cm; (bottom curve) spurious signals from downstream ion probes.

with a test time of approximately 200 μsec, the heat pulse penetrates sufficiently far into the sapphire that the value of the thermal conductivity of the sapphire in immediate contact with the carbon coating does not affect the gauge response. Hence the bulk value of thermal conductivity can be used in calculating the heat transfer.

3 Discussion of Experiments

Preliminary Experiments Without Drive Current. Initial experiments were performed without discharging any current from the drive electrodes or imposing the transverse magnetic field in the accelerator. The incident shock Mach number was varied from 9 to 12, and the detector response was a step rise, which is characteristic of a heat input to the gauge which decays as $1/\sqrt{t}$, see equation (1). The convective heating associated with the growing laminar boundary layer behind a shock wave has the form [10]

$$q = Q_c/t^{1/2}, \tag{3}$$

where q is the rate of heat transfer to the wall and Q_c is the convective heat-transfer coefficient. There was no noticeable effect of radiative heat transfer. Since the radiant heating would be independent of time, the gauge response would vary according to equation (2). However, even at the highest Mach numbers, the gauge response was independent of time for 200 μsec after shock passage. A comparison of the present data with that obtained by Waller [7] showed satisfactory agreement and established that the heat-transfer system was operating properly.

The effect of the transverse magnetic field on the convected heat-transfer rate was investigated by holding the initial-shock Mach number at 11 and varying the transverse magnetic field from 0 to 0.6 Wb/m². It was observed that the magnetic field had no noticeable effect on the shape or magnitude of the detector output signal. The step response, characteristic of the laminar boundary layer, persisted for an average of 175 μsec after the shock passage. Hewett [11] has subsequently theoretically investigated this case and found that, for these experimental conditions, the time necessary for the magnetic field to affect the boundary layer and therefore the rate of heat transfer exceeded the experimental test times.

Heat Transfer From Accelerator. For the accelerated runs, the incident-shock Mach number was 11. Heat-transfer measurements first were made with the current discharged from the electrodes $1^1/_2$ tube diameters upstream of the heat-transfer gauge and secondly from the electrodes adjacent the heat-transfer gauge, see Fig. 1. In both cases the detector output was a factor of two or three greater than the measured response for the non-accelerated flow, indicating a significant increase in the wall-temperature rise. It was also observed that, if the total current and magnetic field were held constant, the detector response was independent of whether the current was discharged from the upstream or downstream electrode pair. The detector output versus the time following the shock arrival at the heat-transfer gauge is plotted in Fig. 2, and typical oscillograms from the accelerated runs are included in Fig. 3. As indicated in Figs. 2 and 3, the voltage–time or equivalently the temperature–time histories of the majority of the runs can be correlated, for the duration of the current pulse, as

$$\Delta T = Kt^{1/2}, \tag{4}$$

where ΔT is the temperature rise of the carbon–sapphire interface of the heat-transfer gauge and K is a constant. This response

corresponds to a heat-transfer rate which is independent of time. The value of the heat-transfer rate to the wall was calculated assuming that equation (4) applied to all runs. The detector output at $t = 110$ μsec was divided by the calibration constant of the heat-transfer system to give the interface temperature rise ΔT. Equation (2) was then used to calculate the heat-transfer rate.

The observed independence of the heat-transfer rate on time and distance along the accelerator wall are in qualitative agreement with the prediction of Leonard and Fay [2] that a Hartmann boundary layer existed on the accelerator's side wall. A detailed Hartmann boundary-layer theory follows in the next section for the purpose of making quantitative comparisons. A second possible explanation for the detector response is that it was caused by increased radiative heating. To check this, the detector optical system was masked, and a small pin hole was made in the heat-transfer-gauge coating, allowing radiation to fall directly on the detector. By masking the optical system, it was possible to keep the detector from saturating. Although the response was somewhat erratic, there was no significant difference between the detector response for accelerated runs and nonaccelerated runs. Since for the nonaccelerated runs the radiative heat transfer was negligible compared with the convected heat transfer, it is felt that radiation was not significant for the accelerated runs.

4 Hartmann Boundary-Layer Theory

For a flow in a constant applied magnetic field B and a constant electric field E, the equations of axial momentum and scalar Ohm's law are

$$\rho \frac{\partial u}{\partial t} + \rho u \frac{\partial u}{\partial x} + \rho v \frac{\partial u}{\partial y} = \frac{\partial}{\partial y}\left(\mu \frac{\partial u}{\partial y}\right) + jB - \frac{\partial p}{\partial x}, \quad (5)$$

$$j = \sigma(E - uB), \quad (6)$$

in which the viscous forces normal to the wall, the magnetic induction due to j, and Hall effects are neglected. While the incorporation of Hall effects is straightforward, their inclusion requires that the differential equations be numerically integrated. However, since for the present experiments the Hall parameter is between 0.4 and 1.7 in the free stream, the neglecting of the Hall currents in the boundary layer is a good approximation. The Hartmann flow exists in the steady case where the terms on the left side of equation (5) are negligible. Comparing the second term in equation (5) with the jB term, the Hartmann flow will exist when

$$\rho u \frac{\partial u}{\partial x} \ll jB = \sigma(E - uB)B. \quad (7)$$

Since E is constant across the boundary layer and the current density is small in the free stream, $E = U_\infty B$ in equation (7). Neglecting u in comparison to U_∞, and since u and $\partial u/\partial x$ are of order U_∞ and U_∞/L, respectively, the above inequality can be written as

$$L \gg \rho U_\infty/\sigma B^2. \quad (8)$$

Equation (8) indicates that after the gas has proceeded downstream under the magnetic field a distance L greater than $\rho U_\infty/\sigma B^2$, the interaction length, the convective term can be neglected in comparison to the jB term. Similarly, it can be shown that $\rho \dfrac{\partial u}{\partial t}$ and $\rho v \dfrac{\partial u}{\partial y}$ are both small compared to the jB term at distances greater than the interaction length. For the flow behind a typical incident shock of Mach number 11, $\rho U_\infty/\sigma B^2$, evaluated using free-stream properties and an applied magnetic field of 0.5 Wb/m², is 9 cm. This is approximately equal to two shock-tube diameters. The heat-transfer gauge was located 7 tube diameters downstream from the entrance of the accelerator.

Equation (5) can be further simplified by neglecting $\partial p/\partial x$. As will be shown in section 5, the force associated with the pressure gradient could be comparable with the $\mathbf{j} \times \mathbf{B}$ force in the free stream. However, in the boundary layer where the current density is significantly higher, the effect of the pressure gradient can be neglected. Equation (5) now becomes

$$\frac{\partial}{\partial y}\left(\mu \frac{\partial u}{\partial y}\right) + jB = 0. \quad (9)$$

It is seen that the momentum equation for the Hartmann flow reduces to a static balance between the viscous force and the jB force. The Hartmann boundary-layer thickness δ_H can be estimated from equation (9); i.e.,

$$\mu(U_\infty/\delta_H) = \sigma(U_\infty B^2)\delta_H. \quad (10)$$

Solving for δ_H,

$$\delta_H = \frac{1}{B}\left(\frac{\mu}{\sigma}\right)^{1/2}. \quad (11)$$

The pertinent dimensionless parameter for this flow is the Hartmann number, $H = d/\delta_H$, the ratio of the tube diameter to the boundary-layer thickness. Evaluating properties at free-stream conditions behind a Mach 11 shock, the Hartmann boundary-layer thickness and the Hartmann number are 0.67 mm and 57, respectively, for an applied transverse magnetic field of 0.5 Wb/m². This high value of the Hartmann number indicates that the curvature effects in the 1½-in-dia tube are negligible and that the one-dimensional theoretical analysis is directly applicable to the tube flow of the experiment.

The energy equation appropriate for the Hartmann flow is

$$(\lambda_e T_e')' + (\lambda T')' + \mu(u')^2 + j(E - uB) + \frac{\epsilon}{m}(D\rho c')' = 0, \quad (12)$$

where the convective terms have been neglected. The equation equates the conduction through a fluid particle to the Joule heating, viscous dissipation, and recombination energy released in a fluid particle. $(\lambda_e T_e')'$ and $(\lambda T')'$ represent the heat conduction due to the electron- and gas-temperature gradients, respectively; $\mu(u')^2$ is the viscous dissipation; $j(E - uB)$, the Joule heating; and $\dfrac{\epsilon}{m}(D\rho c')'$, the net ionization energy released by the recombination of the ion-electron pairs. The primes represent derivatives with respect to y, the coordinate normal to the wall.

The boundary conditions at the wall ($y = 0$) are:

$$T = T_w, \quad c = 0, \quad u = 0, \quad T_e = T_{ew}.$$

At the free stream:

$$T = T_\infty, \quad c = c_\infty, \quad T_e = T_{e\infty}, \quad E = U_\infty B, \quad T' = 0, \quad u' = 0, \quad u = U_\infty.$$

Making the substitution $V = U_\infty - u$, and multiplying equation (9) by $(E - uB)/B$ and adding it to equation (12), yields the total energy equation,

$$(\lambda T')' + (\lambda_e T_e')' + (D\rho\epsilon c'/m)' + \mu(V')^2 + V(\mu V')' = 0. \quad (13)$$

Since $[\mu(V^2)']' = 2\mu V'^2 + 2V(\mu V')'$, equation (13) can be integrated to yield

$$\lambda T' + \lambda_e T_e' + \mu\left(\frac{V^2}{2}\right)' + D\rho\epsilon c'/m = 0. \quad (14)$$

Since the exact state of the gas in the tube is unknown, two cases are considered, that of complete thermodynamic equilibrium and that of nonequilibrium. For the equilibrium case, $T_e' = T$, $c = c_{eq}(T)$, the Saha equilibrium concentration at the gas temperature, and equation (14) can be written in the form

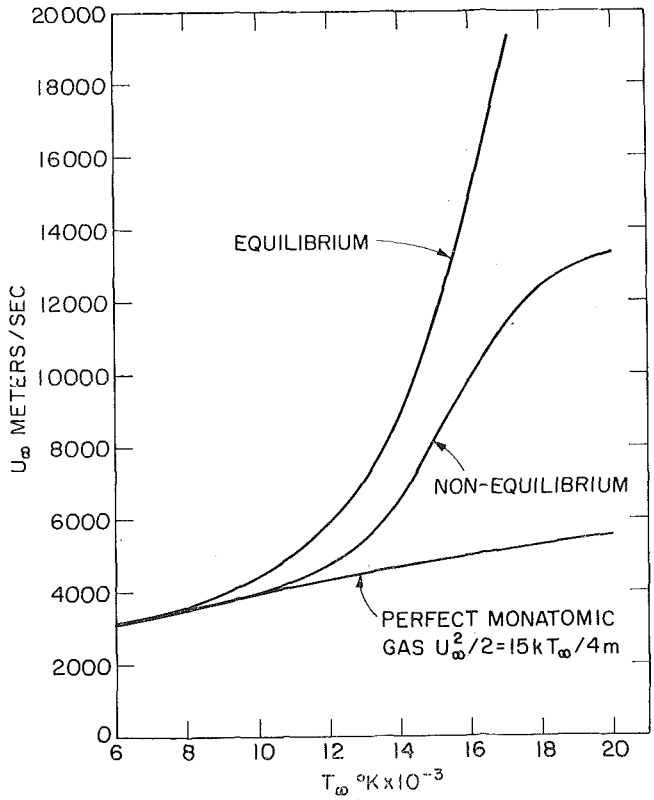

Fig. 4 The free-stream velocity versus the free-stream temperature as predicted by the Hartmann boundary-layer theory for both the equilibrium and nonequilibrium cases. The curve for the monatomic perfect gas is also included.

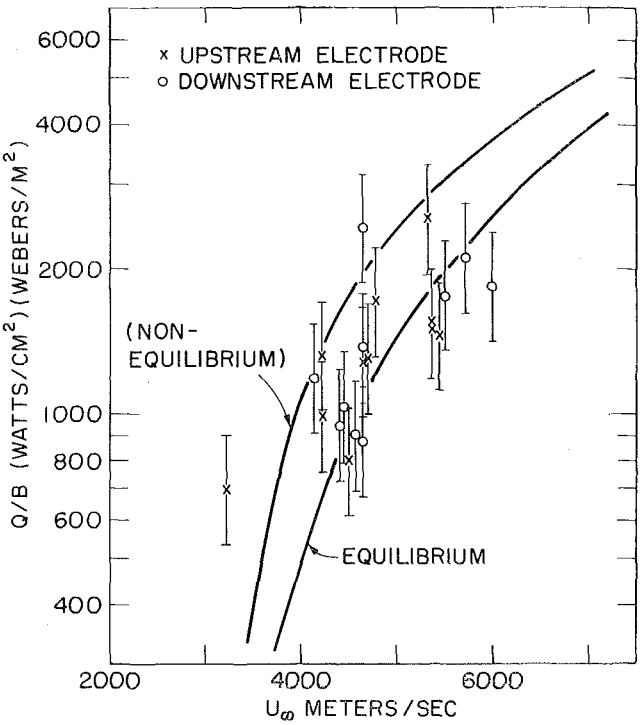

Fig. 5 Heat-transfer rate divided by the applied transverse magnetic field versus the free-stream velocity. Solid curves are the predictions of the Hartmann boundary-layer theory.

$$\lambda_r T' + \mu V V' = 0, \tag{15}$$

where λ_r is the "reactive thermal conductivity." The heat transfer at the wall $(\lambda_r T')_w$ becomes

$$q = -U_\infty(\mu V')_w. \tag{16}$$

To find an expression for $(\mu V')_w$, equation (9) is combined with Ohm's law to yield

$$-(\mu V')' + \sigma B^2 V = 0. \tag{17}$$

Integrating from the wall to infinity,

$$\frac{1}{2}(\mu V')_w^2 = B^2 \int_0^{U_\infty} \mu\sigma V \, dV, \tag{18}$$

and substituting from equation (15), results in the desired relation:

$$(\mu V')_w = -B\left\{2\int_{T_w}^{T_\infty} \sigma\lambda_r dT\right\}^{1/2}. \tag{19}$$

Substituting equation (19) into equation (16),

$$q = \sqrt{2\sigma_\infty\lambda_{r_\infty}T_\infty}\, U_\infty B\left\{\int_0^1 \left(\frac{\sigma}{\sigma_\infty}\right)\left(\frac{\lambda_r}{\lambda_{r_\infty}}\right) d\left(\frac{T}{T_\infty}\right)\right\}^{1/2}, \tag{20}$$

where T_w/T_∞ has been set equal to zero. To relate U_∞ to T_∞, equation (15) is integrated to yield

$$\frac{U_\infty^2}{2} = \left(\frac{\lambda_{r_\infty}}{\mu_\infty}\right) T_\infty \int_0^1 \left(\frac{\lambda_r}{\lambda_{r_\infty}}\right)\left(\frac{\mu_\infty}{\mu}\right) d\left(\frac{T}{T_\infty}\right). \tag{21}$$

For the nonequilibrium case, it is assumed that the electron temperature can be different than the heavy-particle temperature. In particular, the electron-temperature gradient is assumed small and $\lambda_e T_e'$ is set equal to zero. It is further assumed that c, the concentration of electrons, equals $c_{eq}(T)$, the Saha equilibrium concentration at the heavy-particle temperature. This latter assumption is physically a poor assumption, but, since the analysis is meant to give an estimate of the nonequilibrium effects, it is made. Making these substitutions, equation (14) and the heat transfer to the wall become

$$(\lambda_r - \lambda_e)T' + \mu V V' = 0 \tag{22}$$

and

$$q = (\lambda^* T')_w, \tag{23}$$

respectively, where $\lambda^* = \lambda_r - \lambda_e$. Substituting from equations (18) and (22) and assuming that $\sigma = \sigma_\infty$ throughout the boundary layer, results in the desired expression for the heat transfer to the wall:

$$q = \sqrt{2\sigma_\infty\lambda_\infty{}^*T_\infty}\, U_\infty B\left\{\int_0^1 \frac{\lambda}{\lambda_\infty{}^*} d\left(\frac{T}{T_\infty}\right)\right\}^{1/2}. \tag{24}$$

Integrating equation (22) relates the free-stream velocity to the free-stream temperature; i.e.,

$$\frac{U_\infty^2}{2} = \frac{\lambda_\infty{}^*}{\mu_\infty} T_\infty \int_0^1 \left(\frac{\lambda^*}{\lambda_\infty{}^*}\right)\left(\frac{\mu_\infty}{\mu}\right) d\left(\frac{T}{T_\infty}\right). \tag{25}$$

For both cases a simple expression relates the current per unit length along the tube J to the heat-transfer rate calculated by equations (20) and (24). Integrating Ohm's law across the boundary layer,

$$J = \int_0^{\delta_H} \sigma B V dy = \frac{1}{B}\int_0^{\delta_H} (\mu V')' dy = \frac{1}{B}(\mu V')_w \tag{26}$$

$$J = q/BU_\infty.$$

U_∞ is plotted as a function of T_∞ in Fig. 4, for both the equilibrium and the nonequilibrium cases,[3] and q/B is plotted as a function of U_∞ in Fig. 5. The calculations were performed using

[3] For a perfect monatomic gas $U_\infty^2/2 = c_pT_\infty/\mathrm{Pr} = 15kT_\infty/4m$; k is Boltzmann's constant and m is the mass of an argon molecule. This relation is also plotted in Fig. 4.

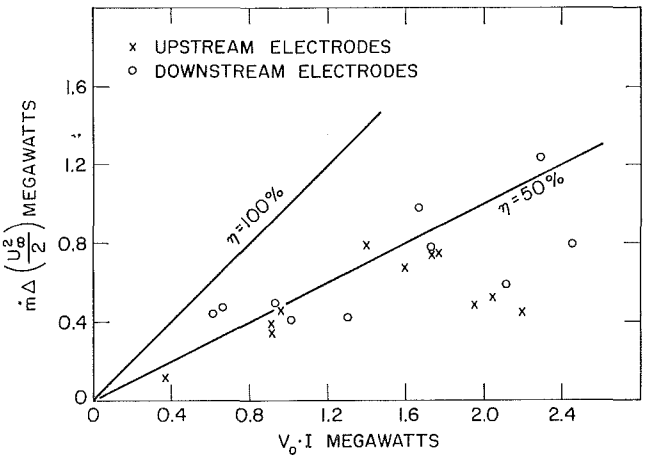

Fig. 6 Kinetic energy efficiency.

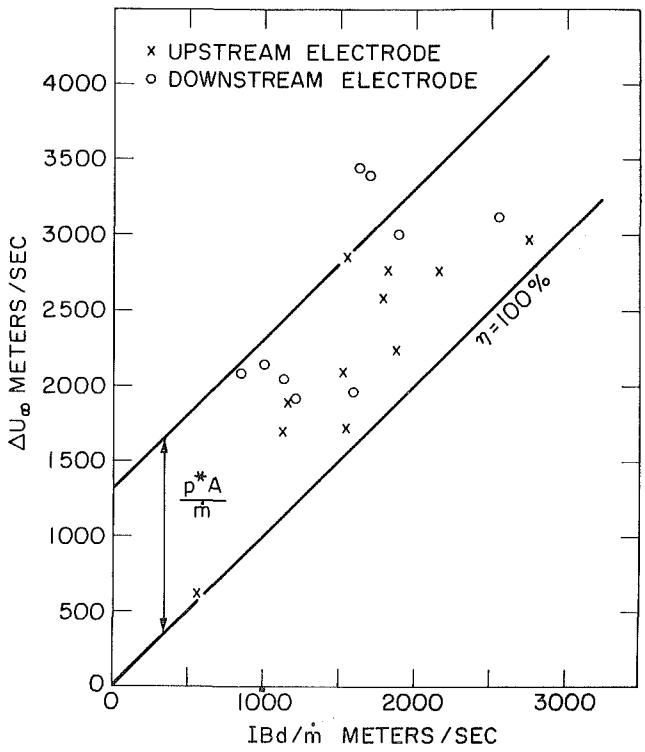

Fig. 7 Momentum efficiency. Only the j × B body force is taken into consideration in the calculation of the efficiency. The 100 percent curve is displaced by an amount $p^*A/\dot{m}$ to take the force due to the pressure drop in the accelerator into consideration.

the transport properties determined by Devoto [12]. For the nonequilibrium case, the Spitzer-Harm thermal conductivity was subtracted from the total thermal conductivity to give λ^*. This reduction of the thermal conductivity for the nonequilibrium case is the primary cause for the difference in the free-stream velocity for the two cases as shown in Fig. 4. For a given U_∞, Fig. 4 predicts a higher free-stream temperature and results in a higher electrical conductivity but in a lower viscosity for the nonequilibrium case. The largest effect resulting in the higher q/B for the nonequilibrium case is a result of the assumption for the nonequilibrium case that the electrical conductivity across the boundary layer is equal to that of the free stream.

The experimental data is plotted in Fig. 5, using the velocity indicated by the internal flowmeter as U_∞. Unfortunately, due to the large scatter in the experimental points, it is impossible to determine which theory best correlates the data. Nevertheless, good general agreement is apparent.

5 Accelerator Performance

The kinetic-energy efficiency for the accelerator is defined as

$$\eta_{KE} \equiv \dot{m}\Delta\left(\frac{U_\infty^2}{2}\right)\Big/ V_0 I, \tag{27}$$

where V_0 is the voltage measured across the drive electrodes, I is the total current, $\dot{m}$ is the mass flow rate, and $\Delta(U_\infty^2/2)$ is the change in kinetic energy per unit of mass in the accelerator. Fig. 6 shows the variation of the kinetic-energy efficiency with the power level. The efficiency lies between 25 and 65 percent and is lowest at high power levels. The losses that cause this low efficiency are heating of the gas, heat transfer to the walls, and heat transfer to the electrodes.

The momentum efficiency is defined as the ratio of the change in momentum through the accelerator to the j × B body force integrated throughout the volume of the accelerator, i.e.,

$$\eta_{mom} \equiv \frac{\dot{m}\Delta U_\infty}{IBd}. \tag{28}$$

Fig. 7 shows that the value of this efficiency is greater than one. This is probably due to a force caused by the pressure drop through the accelerator which is not considered in the simple efficiency defined by equation (28).

To show that the measured change in velocity is less than the maximum theoretical change in velocity, it is assumed that the pressure drop through the accelerator equals p^*, the sonic pressure[4] calculated by Karins [13], for an incident-shock Mach number of 11. This corresponds to the maximum pressure drop through the accelerator since the pressure is highest at the sonic point and since it assumes that the pressure is zero downstream of the accelerator. In Fig. 7 the efficiency is adjusted by $p^*A/\dot{m}$ to take this effect into account. It is seen that the majority of the data points fall below this curve as would be expected.

Because of the uncertainty of the effect of the pressure, the actual efficiency is not clearly discernible. However, if the adjusted curve is assumed to correspond to an efficiency of 100 percent, an average curve drawn through the data corresponds to an efficiency of 70 percent. Apparently the average efficiency lies between 70 and 100 percent. This high average value of the momentum efficiency indicates that the major part of the current discharge went through the gas slug and accelerated the gas rather than flowing through the boundary layer. If a large portion of the current had flowed in the low-velocity boundary layer, the momentum efficiency would be low since the j × B force in the boundary layer is balanced by viscous forces and does not contribute to an increase in the momentum of the flow.

In Fig. 8 the total current flowing through the boundary layers on both sides of the tube for a length of 4 diameters, as predicted by the Hartmann boundary-layer theory, is plotted as a function of the free-stream velocity. The distance 4d was picked as the effective distance for the current flow since this was the average distance between the driving electrodes and the internal flowmeter, Fig. 1. This makes it possible to compare the estimate of the current flow shorting through the boundary layers with that predicted by the momentum balance. Also plotted in Fig. 8 is the total measured current into the accelerator versus the flow velocity measured by the internal flowmeter. It is seen that an average of approximately 17 percent of the total current shorted through the boundary layer over this distance. This agrees with the high value of the momentum efficiency.

To calculate the percent of the total power delivered to the accelerator which could be accounted for by heat losses to the wall, it was assumed that the heat was uniformly transferred to a wall

[4] The flow from the stagnation region in the 6-in. section must achieve a sonic condition as it expands into the 1½-in. tube.

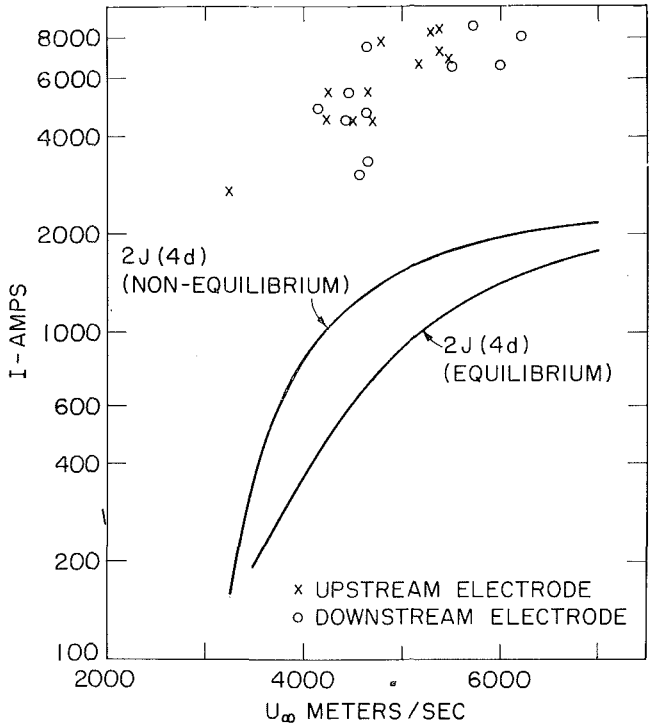

Fig. 8 Total current versus the free-stream velocity. The two curves give the total current flowing in the boundary layers on both sides of the tube for a length along the tube of 4 diameters as predicted by the Hartmann boundary-layer theory. The data corresponds to the total measured current delivered to the accelerator.

area of 182 cm², corresponding to a length of 4 tube diameters. This length was again chosen to make possible the comparison between kinetic energy measurements made at the internal flowmeter and the efficiency plotted in Fig. 6. Using Fig. 5 at a free-stream velocity of 5000 m/sec, the data indicates that q/B is approximately equal to 1600 w/cm²/Wb/m². For an applied magnetic field of 0.5 Wb/m², the total power delivered to the wall is therefore 14.56×10^4 w. By reference to Fig. 6, it can be seen that only about 10 percent of the total power delivered to the accelerator can be accounted for by this loss. This compares poorly with the kinetic-energy efficiency of 40 percent and indicates that the other losses such as heating of the gas and energy fluxes to the electrodes are more important for the conditions investigated here.

6 Conclusions

1 In the absence of any drive current, it was observed that the heat-transfer rate decayed as $1/\sqrt{t}$ and that it was independent of the magnitude of the applied magnetic field.

2 For the accelerated runs, the existence of the Hartmann boundary layer on the side wall of the accelerator is qualitatively substantiated by the observation that the rate of heat transfer is independent of time and distance along the side wall of the accelerator. It is further evidenced by the good quantitative agreement between the Hartmann boundary-layer theory and the measured data.

3 When the heat-transfer measurements were interpreted as a current flow in the boundary layer, it was found that for a length of 4 tube diameters about 17 percent of the total current flowed through the boundary layers. The 17 percent of the total current flowing in the boundary layers reduces the $\mathbf{j} \times \mathbf{B}$ body force in the gas slug by the same amount. This compared with the estimated momentum efficiencies of between 70 and 100 percent and indicates that this loss is an important consideration for explaining the momentum efficiency.

Acknowledgment

This research was supported by NASA Grant NGR-22-009-052 and by the Air Force Office of Scientific Research through Contract AF 44(638)-1396.

References

1 Hogan, W. T., "An Experimental Investigation of a Magnetogasdynamic Accelerator," Magnetogasdynamics Laboratory Report No. 62-1, Department of Mechanical Engineering, M.I.T., Jan. 1962.

2 Leonard, R. L., and Fay, J. A., "Experiments on a Quasi-Steady J × B Accelerator," *AIAA Journal*, Vol. 3, No. 1, Jan. 1965, pp. 115–121.

3 Shercliff, J. A., *A Textbook of Magnetohydrodynamics*, Pergamon Press, New York, 1965.

4 Camac, M., and Feinberg, R., "High Speed Infrared Bolometer," AVCO Everett Research Report 120, March 1962.

5 Croce, P. A., "Shock Tube Induction Flowmeter," *Review of Scientific Instruments*, Vol. 36, No. 11, Nov. 1965, pp. 1561–1564.

6 Friedman, H. S., and Fay, J. A., "Heat Transfer from Argon and Xenon to the End Wall of a Shock Tube," *Physics of Fluids*, No. 11, Nov. 1965, pp. 1968–1975.

7 Waller, M. H., "Shock Tube Side Wall Heat Transfer from High Temperature Monatomic Gases," MS thesis, Department of Mechanical Engineering, M.I.T., May 1965.

8 Cochran, R. A., "Side Wall Heat Transfer Measurements in a Magnetogasdynamic Accelerator," MS thesis, Department of Mechanical Engineering, M.I.T., May 1967.

9 Fay, J. A., and Arnoldi, D. A., "High Temperature Thermal Conductivity of Argon," *Physics of Fluids*, Vol. 11, No. 5, May 1968, pp. 983–985.

10 Mirels, H., "The Wall Boundary Layer Behind a Moving Shock Wave," Reprint from Boundary Layer Research Symposium Freiburg/BR, Aug. 26–29, 1957.

11 Hewett, T. A., "Theory of Flat Plate Heat Transfer in Ionized Monatomic Gases with an Applied Magnetic Field," MS thesis, Department of Mechanical Engineering, M.I.T., May 1968.

12 Devoto, R. S., "Transport Coefficients of Partially Ionized Argon," *Physics of Fluids*, Vol. 10, No. 2, Feb. 1967, pp. 354–364.

13 Karins, C. F., "J × B Acceleration Experiments in a Variable Magnetic Field," MS thesis, Department of Mechanical Engineering, M.I.T., June 1965.

T. CEBECI
Senior Engineer.
Mem. ASME

G. J. MOSINSKIS
Engineer-Scientist.

Aerodynamics Research Group,
Douglas Aircraft Co.,
McDonnell Douglas Corp.,
Long Beach, Calif.

Calculation of Incompressible Turbulent Boundary Layers With Mass Transfer, Including Highly Accelerating Flows[1]

This paper describes a general method for calculating turbulent boundary layers with and without mass addition. The method, as in earlier studies, is based on the eddy-viscosity concept. However, the eddy-viscosity formulation presented in this paper differs from the previous ones in that the previous eddy-viscosity formulation has been generalized to handle flows with mass transfer. A large number of flows computed with this method show good agreement with experiment.

Introduction

In recent years there has been considerable interest in turbulent boundary layers on porous surfaces with either injection or suction through the surface. From a practical point of view, both mass-transfer processes are quite important in problems where it is necessary to protect surfaces exposed to high-temperature gases. In the latter case, for example, distributed injection of a secondary fluid into a boundary layer, which is usually referred to as transpiration cooling, deforms the velocity and temperature distributions through the boundary layer so that the skin friction and heat transfer are reduced. Most of the literature in this area has been restricted to experimental work and has concentrated on measurements of local skin friction, heat-transfer rates, and velocity and temperature profiles for Mach numbers up to 6.7. In addition to the experimental work, there have been a number of theoretical studies in this area. However, most of them are inadequate, and much more work needs to be done.

The present paper is the latest investigation of the accuracy of a prediction method for computing turbulent boundary layers with mass transfer. It is a part of the broad program of development and assessment of a general method for calculating incompressible and compressible turbulent boundary layers with heat and mass transfer. To the authors' knowledge, it is the first detailed study on the subject. So far, this method, which is based on the eddy-viscosity and eddy-conductivity concepts, has been well explored for two-dimensional incompressible flows with and without heat transfer, compressible adiabatic flows, and axisymmetric flows with transverse-curvature effects. In almost all cases, good agreement with experiment was observed [1–4].[2]

As in our previous studies on the subject, we treat the turbulent boundary layer as a composite layer characterized by inner and outer regions. In the inner region, we use an eddy-viscosity expression based on Prandtl's mixing-length theory, and in the outer region we use a constant eddy-viscosity expression modified by an intermittency factor. Although the present approach is also an eddy-viscosity approach, it uses a different eddy-viscosity formulation from the one used in [1–4]. The difference occurs in the inner-region eddy-viscosity expression. Unlike the previous inner eddy-viscosity formula, which used Van Driest's modification of mixing-length theory, the new inner eddy-viscosity formula uses the modification reported in reference [5]. This modification accounts well for the effects of mass transfer and pressure gradient and reduces to Van Driest's modification for nonporous flat-plate flows. It is important to note that such a modification of the inner eddy-viscosity expression was necessary in order to calculate turbulent flows with mass transfer, particularly with injection. For blowing rates F greater than 0.003, the previous eddy-viscosity formulation described in references [1–4] broke down, and calculations could not be made. On the other hand, several comparisons with the generalized eddy viscosity presented in [5] allowed calculations to be made up to blowing rates[3] $F = 0.0095$ and showed good agreement with experimental data. However, before there can be a high level of confidence in the accuracy of this new eddy-viscosity formulation for mass-transfer problems, it is necessary to compute several flows with mass transfer and compare the results with experiment. This is done in this paper.

[1] This work was supported by the McDonnell Douglas Independent Research and Development (IRAD) program.

Contributed by the Heat Transfer Division and presented at the Space Technology and Heat Transfer Conference, Los Angeles, Calif., June 21–24, 1970, of The American Society of Mechanical Engineers. Manuscript received by the Heat Transfer Division March 31, 1970; revised manuscript received October 29, 1970. Based on ASME Paper No. 70-HT/SpT-19.

[2] Numbers in brackets designate References at end of paper.

[3] Higher blowing rates were not attempted, since we could not find any experimental data for comparison.

Description of the Method

The Boundary-Layer Equations. If the normal stress terms are neglected, the incompressible turbulent boundary-layer equations for two-dimensional flow can be written as

$$\frac{\partial u}{\partial x} + \frac{\partial v}{\partial y} = 0 \tag{1}$$

$$u\frac{\partial u}{\partial x} + v\frac{\partial u}{\partial y} = u_e\frac{du_e}{dx} + \frac{\partial}{\partial y}\left[\nu\frac{\partial u}{\partial y} - \overline{u'v'}\right] \tag{2}$$

The boundary conditions are

$$u(x, 0) = 0 \quad v(x, 0) = 0 \quad \text{or} \quad v(x, 0) = v_w \quad \text{(mass transfer)}$$

$$\lim_{y\to\infty} u(x, y) = u_e(x) \tag{3}$$

Eddy-Viscosity Formulation. In order to solve the system (1)–(3), it is necessary to relate $-\overline{u'v'}$ to mean velocity profiles. Here, as in previous studies, we use the eddy-viscosity (ϵ) concept and define

$$-\overline{\rho u'v'} = \rho\epsilon\frac{\partial u}{\partial y} \tag{4}$$

In the eddy-viscosity formulation, as used in previous studies, we treat the boundary layer as a composite layer characterized by inner and outer regions. The existence of these two regions is due to the different response to shear and pressure gradient near the wall. In the inner region we use an eddy viscosity based on Prandtl's mixing-length theory, that is,

$$\epsilon_i = l^2\left|\frac{\partial u}{\partial y}\right| \tag{5}$$

where l, the mixing length, is given by $l = ky$. A modified expression for l is used in (5) to account for the viscous sublayer close to the wall. This modification, suggested by Van Driest [6] and developed by consideration of a Stokes-type flow, is

$$l = ky[1 - \exp(-y/A)] \tag{6}$$

where A is a damping-length constant defined as $26\nu(\tau_w/\rho)^{-1/2}$ and k is an empirical constant equal to 0.4.

The expression given by (6) was obtained by Van Driest for a flat-plate flow with no mass transfer. As it stands, it cannot be used for flows with pressure gradients or for flows with mass transfer. The former is quite obvious, since, for a flow with an adverse pressure gradient, τ_w may approach zero (flow separation). In such a case the mixing-length expression will have a discontinuity, and consequently so will the velocity profiles. For this reason, in [5] the expression given by (6) was modified to account for flows with pressure gradient and mass transfer. This was done by defining A in terms of the friction velocity at the edge of the sublayer rather than its wall value. That is,

$$A = 26\nu\left(\frac{\tau_s}{\rho}\right)^{-1/2} \tag{7}$$

where the subscript denotes sublayer. The sublayer friction velocity was obtained from the momentum equation approximated in the sublayer by the following equation

$$\frac{d\tau}{dy} - \frac{v_w}{\nu}\tau = \frac{dp}{dx} \tag{8}$$

The solution of (8) evaluated at the edge of the sublayer where $y_s = 11.8\nu(\tau_w/\rho)^{-1/2}$ enables the damping-length constant A to be written as

$$A = 26\nu\left(\frac{\rho}{\tau_w}\right)^{1/2}\left\{-\frac{p^+}{v_w{}^+}[\exp(11.8v_w{}^+) - 1] + \exp(11.8\,v_w{}^+)\right\}^{-1/2} \tag{9}$$

With the definition of the damping-length constant given by (9), the expression for inner eddy viscosity, (5), can be written as

$$\epsilon_i = (0.4y)^2[1 - \exp(-y/A)]^2\left|\frac{\partial u}{\partial y}\right| \tag{10}$$

The expression for eddy viscosity in the outer region is based on a constant eddy viscosity ϵ_0,

$$\epsilon_0 = 0.0168\left|\int_0^\infty (u_e - u)dy\right| \tag{11}$$

modified by Klebanoff's intermittency factor [7], γ, approximated by the following formula:

$$\gamma = \left[1 + 5.5\left(\frac{y}{\delta}\right)^6\right]^{-1} \tag{12}$$

The constraint used to define the inner and outer regions is the continuity of the eddy viscosity; from the wall outward, the expression for inner eddy viscosity applies until $\epsilon_i = \epsilon_0$.

Transformation of Boundary-Layer and Eddy-Viscosity Equations. Equations (1)–(3) are singular at $x = 0$. For this reason, they are transformed to a coordinate system that removes the singularity. The application of the Levy-Lees transformation

$$d\xi = \rho\mu u_e dx \qquad d\eta = \frac{\rho u_e}{(2\xi)^{1/2}}dy \tag{13}$$

Nomenclature

A = damping length constant
c_f = local skin-friction coefficient
f = dimensionless stream function
F = blowing parameter, v_w/u_e
H = total enthalpy
K = acceleration parameter, $\frac{\nu}{u_e{}^2}\frac{du_e}{dx}$
l = mixing length
p^+ = pressure gradient parameter, $K\left(\frac{2}{c_f}\right)^{3/2}$
q = local heat-transfer rate per unit area
R_x = Reynolds number, $u_e x/\nu$
R_θ = Reynolds number, $u_e\theta/\nu$
St = Stanton number
u, v = x and y components of velocity
u^* = friction velocity, $\sqrt{\tau_w/\rho}$
$v_w{}^+$ = dimensionless mass-transfer parameter, v_w/u^*
x, y = rectangular coordinates
y^+ = Reynolds number, yu^*/ν
β = dimensionless velocity-gradient term, $\frac{2\xi}{u_e}\frac{du_e}{d\xi}$
γ = intermittency factor
δ = boundary-layer thickness
δ^* = displacement thickness $\int_0^\infty (1 - u/u_e)dy$
ϵ = eddy viscosity
ϵ^+ = ratio of eddy viscosity to kinematic viscosity, ϵ/ν
η = transformed y coordinate
θ = momentum thickness, $\int_0^\infty u/u_e \times (1 - u/u_e)dy$
μ = dynamic viscosity
ν = kinematic viscosity
ξ = transformed x coordinate
ρ = density
τ = shear stress
ψ = stream function

Subscripts

e = outer edge of boundary layer
s = sublayer
w = wall

primes denote differentiation with respect to η

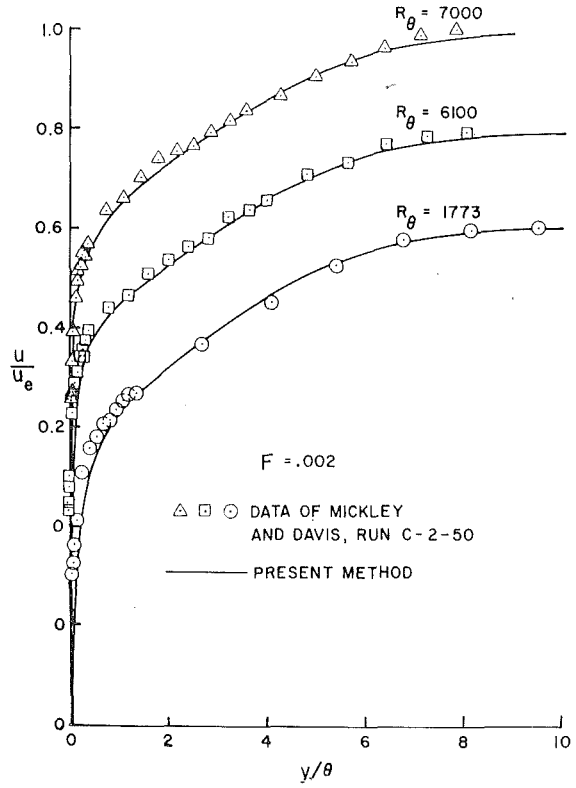

Fig. 1 Comparison of calculated and experimental velocity profiles for the blown boundary layer measured by Mickley and Davis [10]

and the introduction of a dimensionless stream function f related to the usual stream function ψ by

$$\psi(x, y) = (2\xi)^{1/2} f(\xi, \eta) \tag{14}$$

transforms the momentum equation into the following form:

$$[(1 + \epsilon^+)f'']' + ff'' + \beta[1 - (f')^2] = 2\xi\left[f'\frac{\partial f'}{\partial \xi} - f''\frac{\partial f}{\partial \xi}\right] \tag{15}$$

where $f' = u/u_e$.

Similarly, the boundary conditions given by (3) and the eddy-viscosity equations given by (10) and (11) can also be transformed by (13) and (14). These transformed equations as well as the numerical method used to solve (15) subject to (3) are not presented here. The reader is referred to references [8, 9].

Comparison of Calculated and Experimental Results

A prediction method for turbulent flows can be tested only by comparison of results with experimental data; hence the accuracy of such data is important to the evaluation of the method. For this reason, data from several sources on turbulent boundary layers with blowing and suction have been considered, and comparisons of calculated and experimental results have been made for a wide range of mass-transfer rates. Some of these experimental data are for flat-plate flows, and some are for either decelerating or accelerating flows. In the latter case, several comparisons were also made for flows with no mass transfer.

For flows with mass transfer, the experimental data considered in this paper are data due to Mickley and Davis [10], Jonsson and Scott [11], McQuaid [12], Simpson, et al. [13], Tennekes [14], and Julien et al. [15]. All of these data have detailed velocity-profile measurements. Except for the data of McQuaid and Julien, et al., all of them are for flat-plate flows. In these experimental data, skin-friction coefficients were obtained from the velocity profiles and were not measured. In addition, they

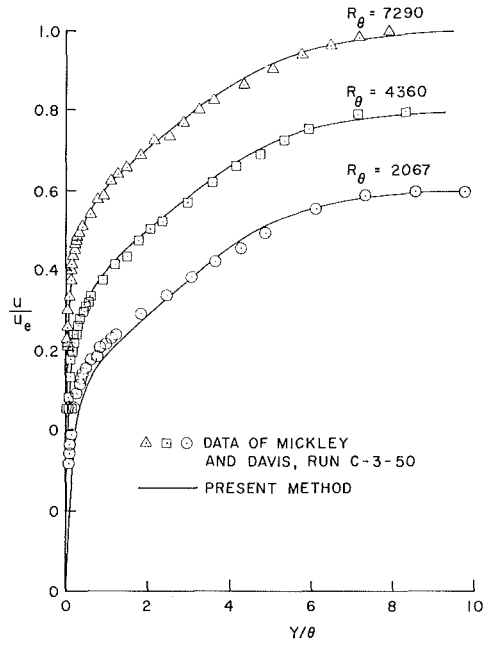

Fig. 2 Comparison of calculated and experimental velocity profiles for the blown boundary layer measured by Mickley and Davis [10]; F = 0.003

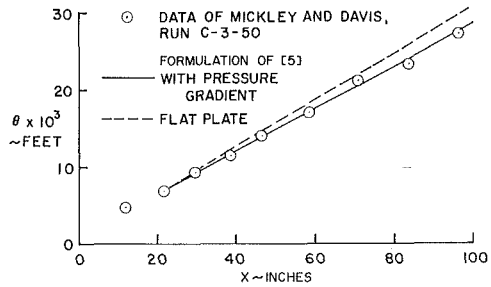

Fig. 3 Comparison of momentum-thickness values for the boundary layer measured by Mickley and Davis [10]; F = 0.003

are all for continuous suction or injection, except for the data of McQuaid that contain discontinuous injection and measured velocity profiles in the regions with and without mass transfer.

Flat-Plate Flows With Blowing. For flat-plate flows with blowing, we have made calculations for the data of Mickley and Davis [10], Jonsson and Scott [11], McQuaid [12], and Simpson et al. [13]. The results are shown in Figs. 1–11.

Figs. 1–4 show the results for the data of Mickley and Davis for two different blowing rates, namely, F = 0.002 and 0.003. As was noted by Stevenson [16] there was a slight pressure gradient for the case F = 0.003. For this reason, calculations were made with and without the pressure-gradient effect for this case. A least-squares curve fit was used to obtain the following smooth velocity distribution from the experimental data:

$$u_e = 48.6 + 0.075x - 0.000396x^2 \tag{16}$$

In (16), u_e is in feet per second and x is in inches.

Fig. 2 shows a comparison of calculated and experimental velocity profiles for three different R_θ values for F = 0.003. These calculations were made by using the velocity distribution given by (16).

The effect of pressure gradient on the calculated momentum-thickness values is shown in Fig. 3. It is quite evident that the calculated θ values agree well with the experimental values when the pressure gradient is taken into account.

Fig. 4 shows a comparison of calculated and experimental local skin-friction values, together with those given by Stevenson

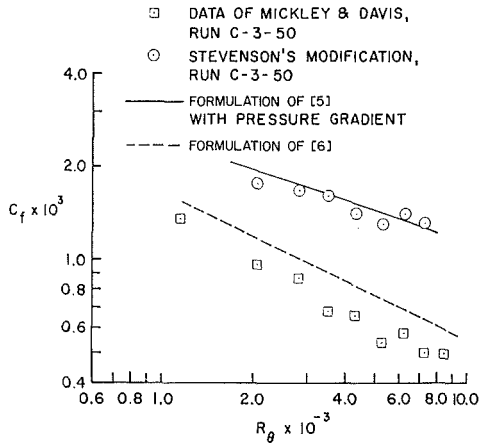

Fig. 4 Comparison of local skin-friction values for the boundary layer measured by Mickley and Davis [10]; $F = 0.003$

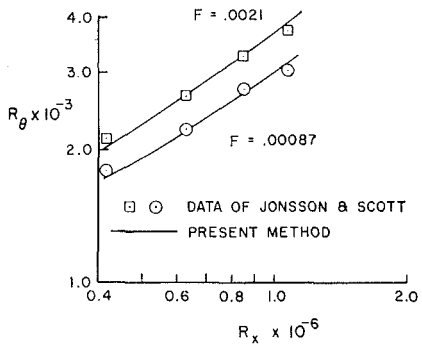

Fig. 5 Comparison of R_θ values for the boundary layer measured by Jonsson and Scott [11]

[16]. In reference [16] Stevenson considered the pressure-gradient effect in the data of Mickley and Davis (which Mickley and Davis had neglected) and, by using the momentum integral equation, demonstrated that when the pressure-gradient effect was considered, the experimental local skin-friction values were much higher than the values estimated by Mickley and Davis.

Calculations were made by using the eddy-viscosity formulation of [5], with damping-length constant given by (9), as well as by using the eddy-viscosity formulation of [6], $A = 26\nu(\rho/\tau_w)^{1/2}$. In both calculations the velocity distribution given by (16) was used. The calculated results obtained by using the present formulation agree quite well with those given by Stevenson and disagree by a factor of two with those obtained by Mickley and Davis.

In reference [11], Jonsson and Scott made an experimental study to investigate the effects of uniform air injection into the turbulent boundary layer on a circular cylinder in axial flow. The blowing-rate parameter F varied from 0 to 0.0021, and the Reynolds number based on free-stream conditions varied from 4.0×10^5 to 10.6×10^5. Fig. 5 shows a comparison of calculated and experimental R_θ values for two blowing rates, $F = 0.00087$ and 0.0021. Fig. 6 shows the velocity profiles for $F = 0.0021$. The agreement in both cases seems to be good.

In reference [12], McQuaid described an extensive series of mean-velocity measurements on the incompressible turbulent boundary layer with distributed injection. He measured boundary-layer developments along a porous flat plate for blowing rates F between 0 and 0.008 at free-stream velocities of 50 and 150 fps. He used the momentum integral equation to obtain the local skin-friction coefficient. As was pointed out by Simpson et al. in reference [13], the reported skin-friction values of McQuaid are very uncertain for these data. The reasons are that (*a*) there is variation in injection velocity over the test surface, (*b*) the usable test section is short, and (*c*) the fact that F is subtracted from the momentum-thickness gradient to obtain the local skin-friction coefficient.

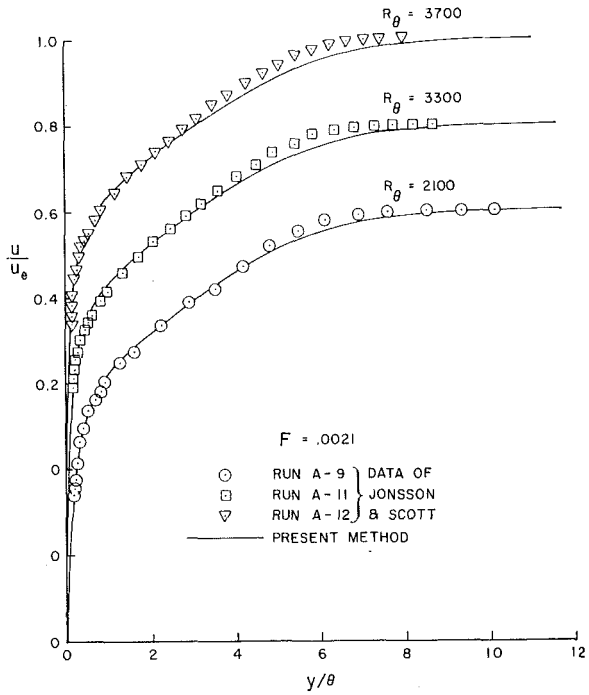

Fig. 6 Comparison of calculated and experimental velocity profiles for the blown boundary layer measured by Jonsson and Scott [11]

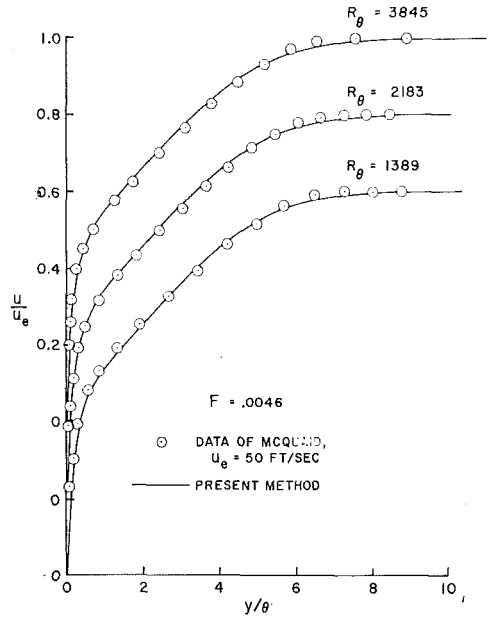

Fig. 7 Comparison of calculated and experimental velocity profiles measured by McQuaid [12]

Fig. 7 shows comparisons of calculated and experimental velocity profiles for three different R_θ values for $F = 0.0046$. Figs. 8 and 9 show the results for a flow involving discontinuous injection. The calculations were started by using the experimental velocity profile at $x = 0.958$ ft and were continued downstream with a uniform injection rate, $F = 0.0034$, up to and including $x = 1.450$ ft. The blowing rate was set to zero at $x = 1.460$ ft and at all subsequent downstream locations. The Δx spacing near the point of discontinuity was taken as follows:

x (ft)	1.450	1.460	1.463	1.4667
F	0.0034	0	0	0

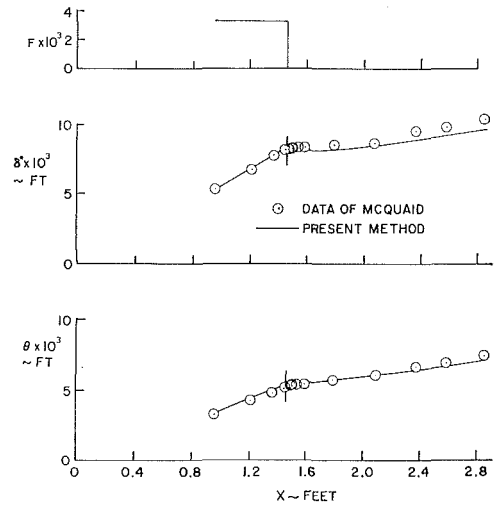

Fig. 8 Comparison of calculated and experimental displacement and momentum thicknesses for the boundary layer with discontinuous injection measured by McQuaid [12]

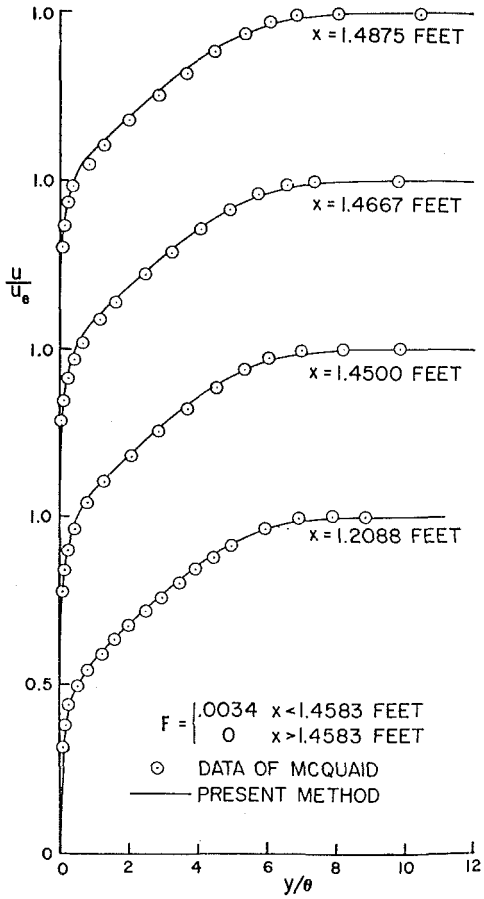

Fig. 9 Comparison of calculated and experimental velocity profiles for the boundary layer with discontinuous injection measured by McQuaid [12

This spacing was selected arbitrarily. The first and the last values of x in the above table correspond to the stations where velocity-profile measurements were reported. Results show that the experimental trends are closely followed by the calculations, including the results for the region after which the mass transfer is zero.

Probably the best experimental data on incompressible turbulent boundary layers with mass transfer are those obtained by Simpson et al. [13]. These measurements were made for a wide

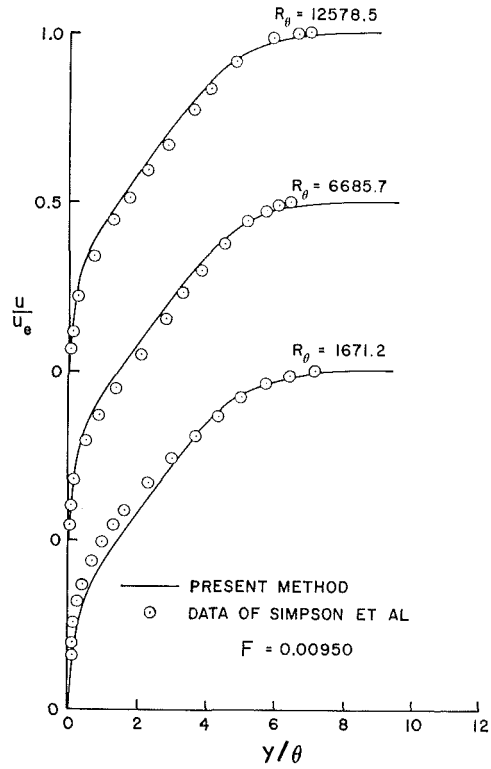

Fig. 10 Comparison of calculated and experimental velocity profiles for the blown boundary layer measured by Simpson, et al. [13]

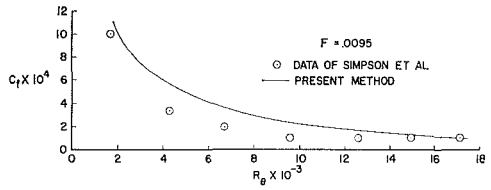

Fig. 11 Comparison of calculated and experimental local skin-friction values for data of Simpson, et al. [13]

range of blowing parameter F at a constant free-stream velocity of 44 fps. The velocity profiles were measured and the local skin-friction values were obtained by using a momentum-integral-equation method and a viscous-sublayer-model method. Both methods were found to give almost the same local skin-friction value. With the exception of 2 out of 95 traverses, the values of skin friction for a given traverse obtained by both methods agreed within the experimental uncertainty.

Figs. 10 and 11 show comparisons of calculated and experimental velocity profiles and skin-friction values, respectively, for the blowing rate $F = 0.00950$. Considering that this is a rather high blowing rate, the agreement is satisfactory.

Flat-Plate Flows With Suction. For flat-plate flows with suction, we have made calculations for the data of Tennekes [14] for two suction rates, $F = -0.00312$ and -0.00429. The results are shown in Figs. 12–14. Fig. 12 presents comparison of calculated and experimental velocity profiles. Calculations were made by using the eddy-viscosity formulation of [5, 6]. The results obtained by using the formulation of [5] show a marked improvement over the formulation of [6] which was restricted to flat-plate flows with no mass transfer.

Figs. 13 and 14 show comparisons of calculated and experimental values of momentum thickness and local skin friction, respectively. The agreement of the former is good, and a slight discrepancy in the calculated and experimental values is probably due to the assumptions made in the u/u_e values very close to the wall in order to obtain the experimental θ values. On

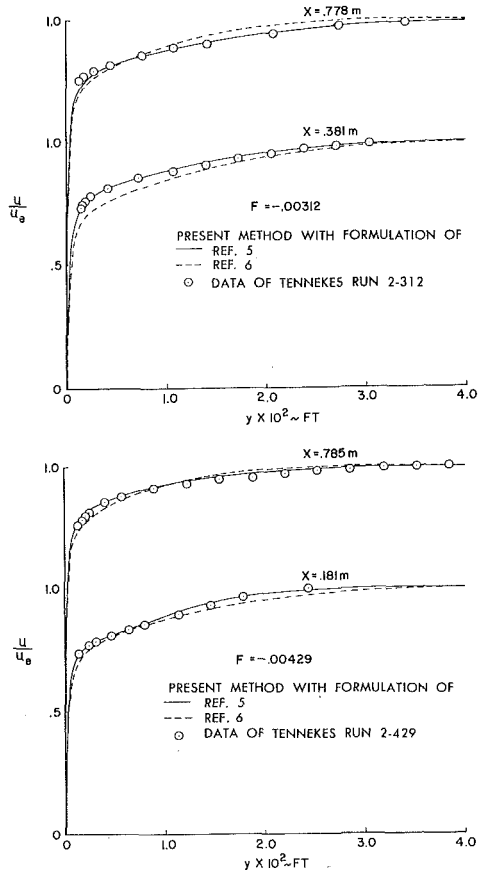

Fig. 12 Comparison of calculated and experimental velocity profiles for the experimental data of Tennekes [14]. The calculations were made with the eddy-viscosity formulation of [5] and [6].

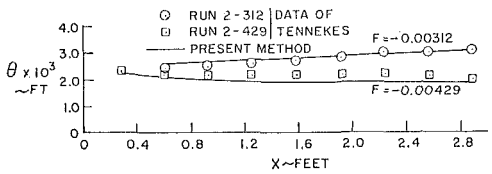

Fig. 13 Comparison of calculated and experimental momentum-thickness values for the experimental data of Tennekes [14]

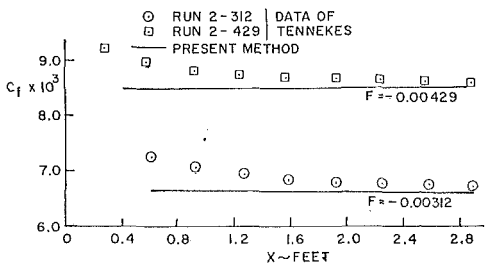

Fig. 14 Comparison of calculated and experimental local skin-friction values for the experimental data of Tennekes [14]

the other hand, at the beginning the agreement in c_f values is not good. However, as the calculations proceed downstream, the discrepancy decreases and the results agree better with the experimental data.

Pressure-Gradient Flows With Blowing. Figs. 15–18 show the results for pressure-gradient flows with blowing. The experimental data are due to McQuaid.

Figs. 15 and 16 show the results for a favorable pressure-gradient flow for a blowing rate of $F = 0.008$. The calculations were started by using the experimental velocity profile at $x =$

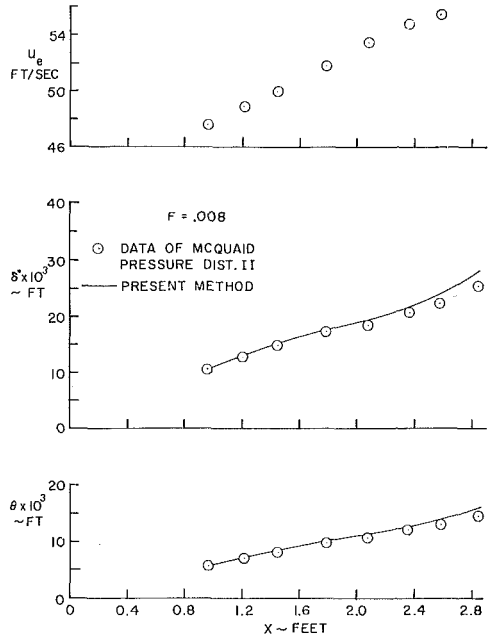

Fig. 15 Comparison of calculated and experimental displacement and momentum thicknesses for the boundary layer in a favorable pressure gradient measured by McQuaid [12]

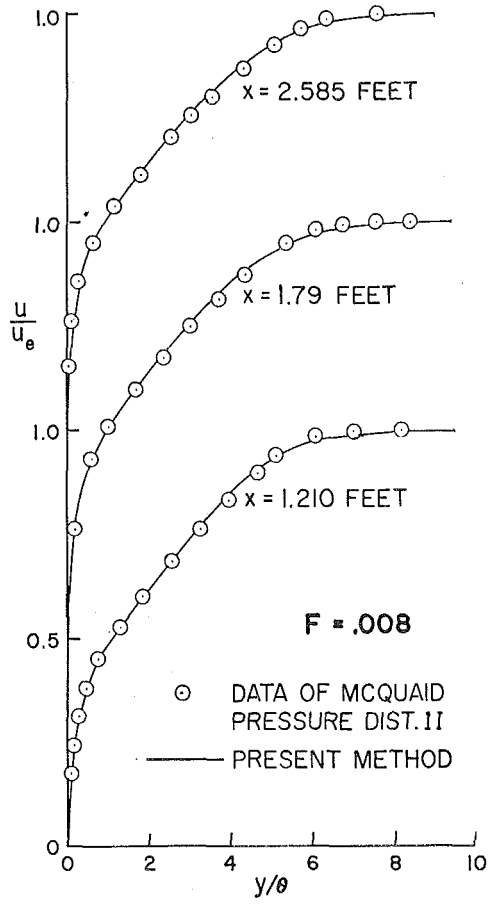

Fig. 16 Comparison of calculated and experimental velocity profiles for the boundary layer in a favorable pressure gradient measured by McQuaid [12]

0.958 ft and were continued downstream with the given blowing rate. It is interesting to note that in Fig. 15 the deviations of the calculated δ^* and θ values from their experimental values are not reflected in the velocity-profile comparisons of Fig. 16.

Figs. 17 and 18 show the results for an adverse pressure-gradient flow with a blowing rate of $F = 0.002$. The calcula-

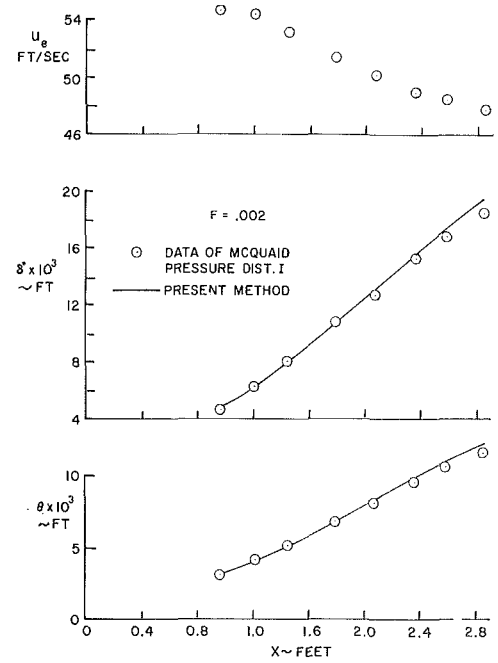

Fig. 17 Comparison of calculated and experimental displacement and momentum thicknesses for the boundary layer in an adverse pressure gradient measured by McQuaid [12]

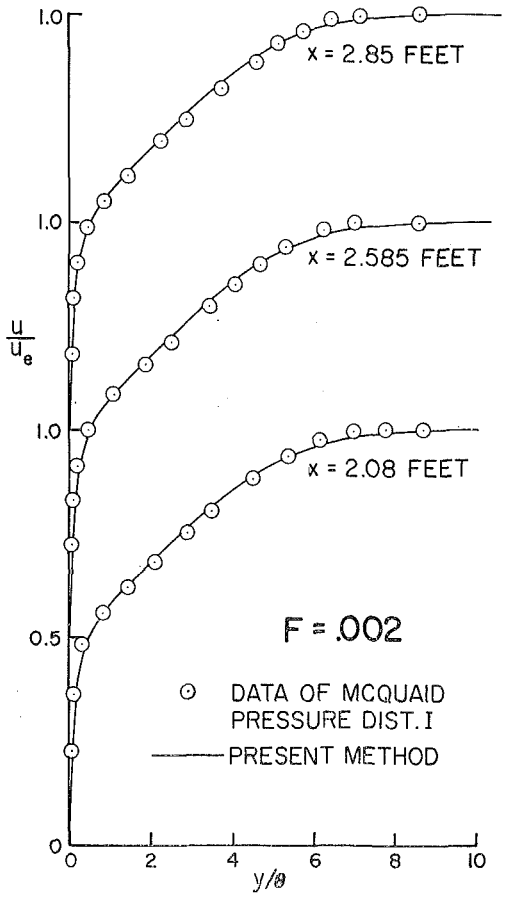

Fig. 18 Comparison of calculated and experimental velocity profiles for the boundary layer in an adverse pressure gradient measured by McQuaid [12]

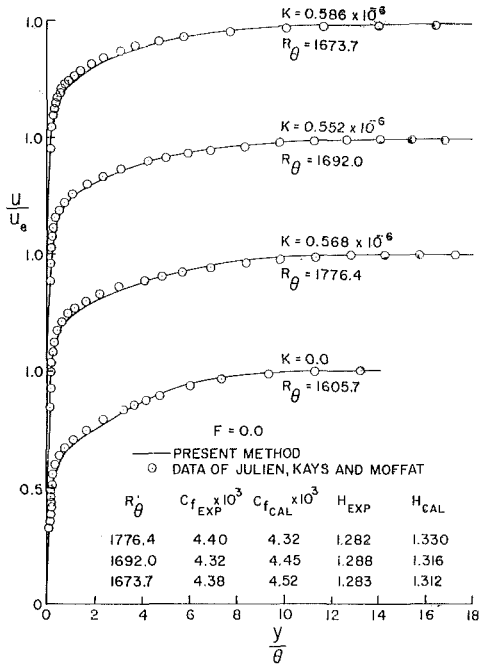

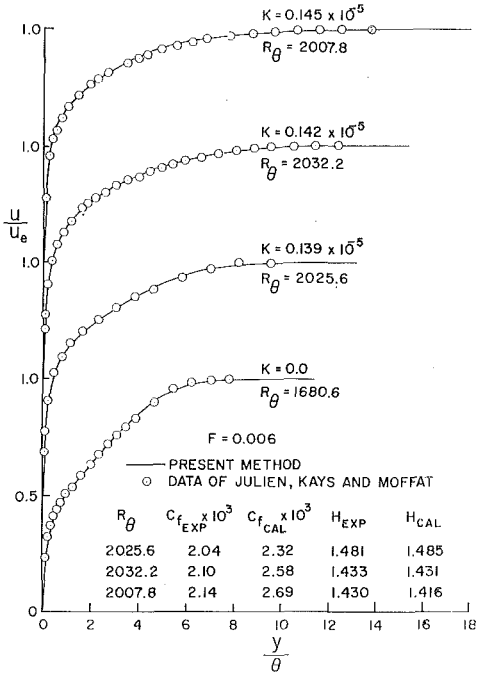

Fig. 19 Comparison of calculated and experimental velocity profiles for the accelerating boundary layer measured by Julien, et al. [15]

tions were started by initially matching the zero-pressure-gradient data for the given blowing rate at $x = 0.958$ ft. Velocity-profile comparisons of Fig. 18 show that agreement with experiment is very good, even at locations far downstream for which the agreement of δ^* and θ with experiment, as shown in Fig. 17, is not as good.

Highly Accelerating Flows With and Without Mass Transfer. In reference [15], Julien et al. have reported a number of velocity-profile data for blown, unblown, and sucked accelerated boundary layers. The pressure gradients investigated are those corresponding to constant values of the acceleration parameter $K = (\nu/u_e^2)(du_e/dx)$. The three values of K considered are 0.57×10^{-6}, 0.77×10^{-6}, and 1.45×10^{-6}. For each acceleration parameter, the surface boundary conditions cover a range of

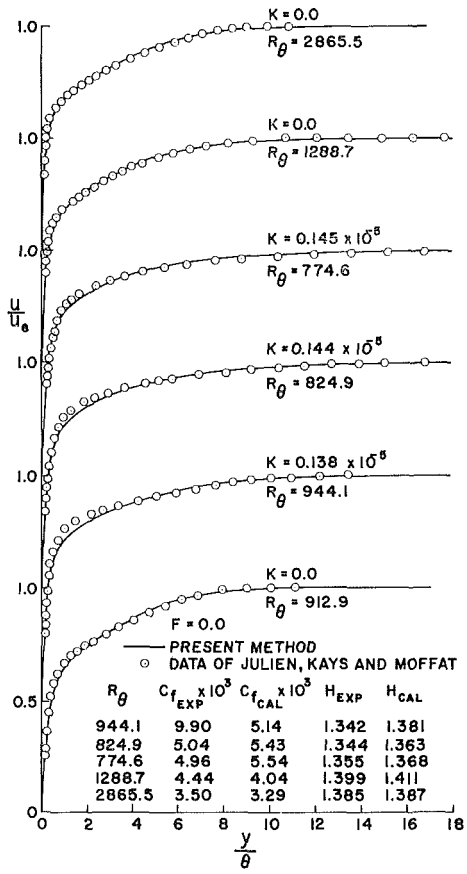

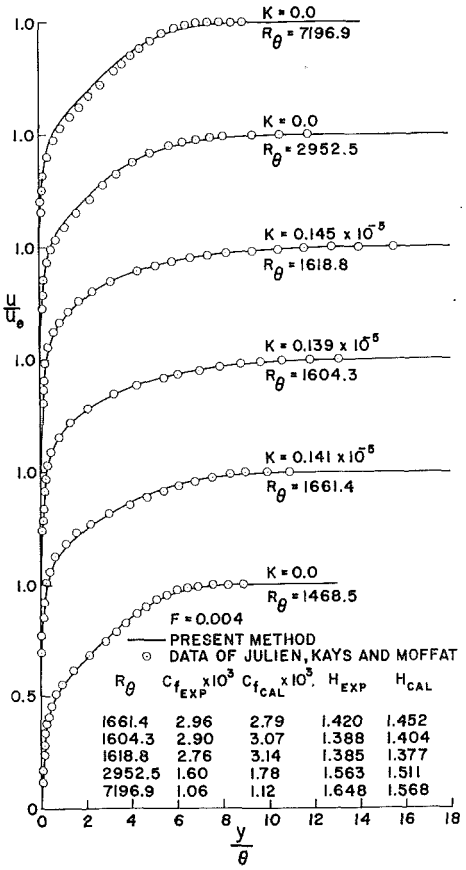

Fig. 20 Comparison of calculated and experimental velocity profiles for the accelerating boundary layer measured by Julien, et al. [15]

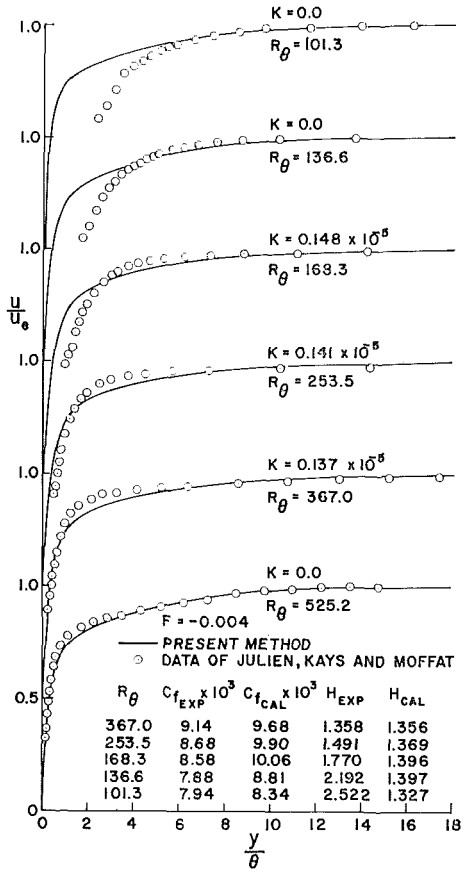

Fig. 21 Comparison of calculated and experimental velocity profiles for the accelerating boundary layer measured by Julien, et al. [15]

constant blowing and sucking fractions from $F = -0.004$ to 0.006.

Calculations made for the experimental data are shown in Figs. 19–21. The comparisons presented in Fig. 19 all start with flat-plate flow and continue with a uniform acceleration parameter. On the other hand, although the comparisons presented in Fig. 20 start and continue in the same way as those in Fig. 19, they end in the presence of zero pressure gradient. The relative importance of these results, compared to those in Fig. 19, is that the calculations account well for the removal of the pressure gradient. In general, the agreement between calculated and experimental results is quite satisfactory. But the results for a boundary layer with suction presented in Fig. 21 do not agree at all with experiment. The experimental velocity profiles clearly show the features of a laminar flow, and the calculated results show the features of a turbulent flow. However, it is to be noted that the Reynolds number for this flow is very low. Obviously, the empirical constants used in the eddy-viscosity formulas are not appropriate for these flows.

In addition to the experimental data of Julien et al., we have also considered two sets of experimental data that included heat transfer. These are the data of Back [17, 18]. Measurements were made for two accelerating flows of varying degrees of acceleration at constant heat flux. A comparison of calculated and experimental velocity profiles together with local skin-friction values and local Stanton numbers, St, defined by

$$\mathrm{St} = \frac{-q_w}{\rho_e u_e (H_e - H_w)} \tag{19}$$

is shown in Figs. 22 and 23. The solution of the energy equation as described in [3] was obtained for a constant turbulent Prandtl number of 0.9. The results show that for $u_e = 110$ fps, which corresponds to a relatively high Reynolds number in comparison

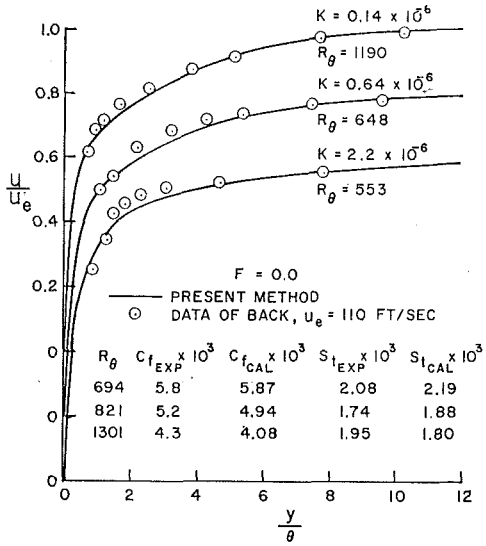

Fig. 22 Comparison of calculated and experimental velocity profiles for the highly accelerating boundary layer measured by Back [17], u_e = 110 fps

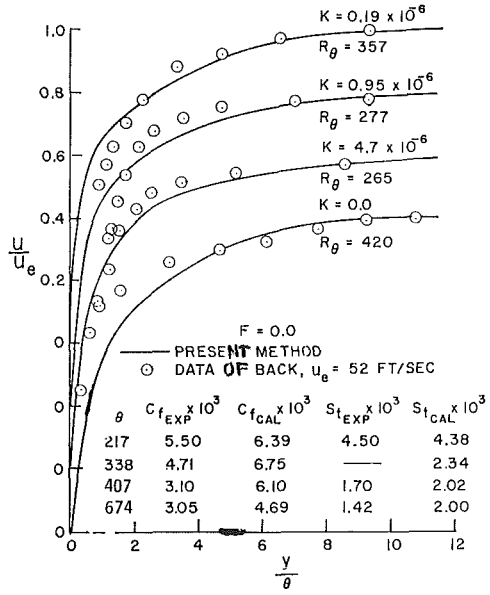

Fig. 23 Comparison of calculated and experimental velocity profiles for the highly accelerating boundary layer measured by Back [17], u_e = 52 fps

to the other one, the agreement is rather good. The agreement in velocity profiles improves with increasing Reynolds number. On the other hand, the agreement for u_e = 52 fps is not good at all. However, the authors believe that the discrepancy between prediction and experiment is not only due to the flow acceleration but also due to the *Reynolds-number effect*. It is also important to note that the agreement in velocity profiles for $K = 0$, $R_\theta = 420$ is bad, but that the agreement for $K = 4.7 \times 10^{-6}$, $R_\theta = 265$ (which corresponds to a very highly accelerating, laminarizing flow) is satisfactory. It is also quite possible that the present eddy-viscosity formulation does not apply at such low Reynolds numbers.

Prediction of Stanton Number for Flat-Plate Flows With Suction and Blowing. The present method, although not described in this paper, also has the capability of predicting heat-transfer rates with mass addition [3]. For this reason, calculations were also made to investigate the accuracy of calculating Stanton numbers for flows with heat and mass transfer. The experimental data of Moffat and Kays [19] were chosen for this purpose, and calculations were made for various flat-plate flows with suction and blowing. Again, the turbulent Prandtl number was assumed to be 0.9. The results as shown in Fig. 24 are in good agreement with experiment.

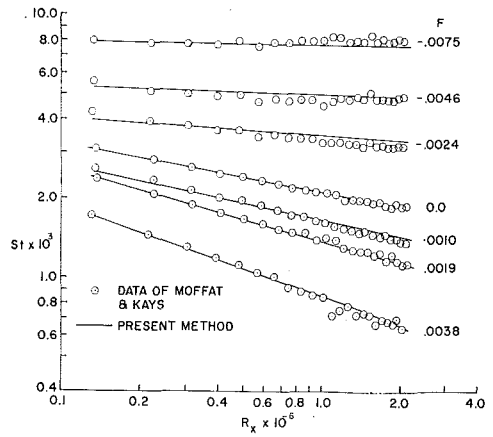

Fig. 24 Comparison of calculated and experimental Stanton numbers for the boundary layer measured by Moffat and Kays [19]

Concluding Remarks

A general method was presented for predicting two-dimensional incompressible turbulent boundary layers with mass addition. Also, several highly accelerating flows with and without mass transfer were considered. The results show that the agreement between calculated and experimental results is quite satisfactory and that the proposed modification of the inner eddy-viscosity formula accounts very well for mass-transfer effects. The results also point out that as the Reynolds number decreases, the agreement between predicted results and experimental results becomes poorer. Although it is difficult to say at what Reynolds number this difference begins to be noticeable, according to the comparisons presented here, it seems to be around $R_\theta = 1000$. However, this is a weak effect until R_θ decreases more and becomes as low as 500. Then the discrepancy increases. But this time the question arises: Are the boundary layers positively turbulent at these Reynolds numbers? According to Preston [20], a necessary but not a sufficient condition for the minimum value of R_θ at which a flow can be turbulent is around 320. More experiments are needed to clarify the situation at such low Reynolds numbers.

The results also indicate the need for some improvement in the present eddy-viscosity formulas to account for low-Reynolds-number flows. This is not surprising, since the empirical constants being used in the eddy-viscosity formulas were obtained from data at high Reynolds number, for $R_\theta > 5000$.

References

1 Cebeci, T., and Smith, A. M. O., "A Finite-Difference Solution of the Incompressible Turbulent Boundary-Layer Equations by an Eddy-Viscosity Concept," *AFOSR-IFP, Stanford Conference on Turbulent Boundary-Layer Predictions*, Vol. 1, 1968.

2 Cebeci, T., Smith, A. M. O., and Mosinskis, G., "Calculation of Compressible Adiabatic Turbulent Boundary Layers," *AIAA Journal*, Vol. 8, No. 11, Nov. 1970, pp. 1973–1982.

3 Cebeci, T., Smith, A. M. O., and Mosinskis, G., "Solution of the Incompressible Turbulent Boundary-Layer Equations With Heat Transfer," JOURNAL OF HEAT TRANSFER, TRANS. ASME, Series C, Vol. 92, No. 1, Feb. 1970, pp. 133–143.

4 Cebeci, T., "Laminar and Turbulent Incompressible Boundary Layers on Slender Bodies of Revolution in Axial Flow," *Journal of Basic Engineering*, TRANS. ASME, Series D, Vol. 92, No. 3, Sept. 1970, pp. 545–554.

5 Cebeci, T., "The Behavior of Turbulent Flow Near a Porous Wall with Pressure Gradient," *AIAA Journal*, Vol. 8, No. 12, Dec. 1970, pp. 2152–2156.

6 Van Driest, E. R., "On Turbulent Flow Near a Wall," *Journal of the Aeronautical Sciences*, Vol. 23, No. 11, Nov. 1956.

7 Klebanoff, P. S., "Characteristics of Turbulence in a Bound-

ary Layer with Zero Pressure Gradient," NACA TN 3178, July 1954.
8 Cebeci, T., and Mosinskis, G. J., "Calculation of Heat and Mass Transfer in Turbulent Flows at Low Mach Numbers," Douglas Aircraft Report No. DAC 70015, Nov. 1969.
9 Cebeci, T., and Smith, A. M. O., "A Finite-Difference Method for Calculating Compressible Laminar and Turbulent Boundary Layers," *Journal of Basic Engineering*, TRANS. ASME, Series D, Vol. 92, No. 3, Sept. 1970, pp. 523–535.
10 Mickley, H. S., and Davis, R. S., "Momentum Transfer for Flow Over a Flat Plate with Blowing," NACA TN 4017, Nov. 1957.
11 Jonsson, V. K., and Scott, C. J., "Uniform Air Injection into a Turbulent Boundary-Layer Flow Over an Axial Circular Cylinder," University of Minnesota Heat Transfer Laboratory, Report No. HTL-TR-63, July 1965.
12 McQuaid, J., "Experiments on Incompressible Turbulent Boundary Layers with Distributed Injection," ARC 28735, 1967.
13 Simpson, R. L., Kays, W. M., and Moffat, R. J., "The Turbulent Boundary Layer on a Porous Plate: An Experimental Study of the Fluid Dynamics with Injection and Suction," Report No. HMT-2, Stanford University, 1967.
14 Tennekes, H., "Similarity Laws for Turbulent Boundary Layers with Suction or Injection," Report VTH-119, Technological University, Delft, the Netherlands, Dec. 1964.
15 Julien, H. L., Kays, W. M., and Moffat, R. J., "The Turbulent Boundary Layer on a Porous Plate: Experimental Study of the Effects of a Favorable Pressure Gradient," Report No. HMT-4, Stanford University, 1969.
16 Stevenson, T. N., "A Law of the Wall for Turbulent Boundary Layers with Suction or Injection," CoA Report Aero No. 166, College of Aeronautics, Cranfield, England, July 1963.
17 Back, L. H., "Heat Transfer to Turbulent Boundary Layers with a Variable Free-Stream Velocity," PhD thesis, University of California, Berkeley, Calif., 1962.
18 Back, L. H., and Seban, R. A., "Flow and Heat Transfer in a Turbulent Boundary Layer with Large Acceleration Parameter," *Proceedings of 1967 Heat Transfer and Fluid Mechanics Institute*, Stanford University, 1967.
19 Moffat, R. J., and Kays, W. M., "The Turbulent Boundary Layer on a Porous Plate: Experimental Heat Transfer with Uniform Blowing and Suction," *International Journal of Heat and Mass Transfer*, Vol. 11, 1968, pp. 1547–1566.
20 Preston, J. H., "The Minimum Reynolds Number for a Turbulent Boundary Layer and the Selection of a Transition Device," *Journal of Fluid Mechanics*, Vol. 3, 1958, p. 373.

A. WORTMAN
Engineering Specialist,
Aerodynamics Research Branch,
Northrop Corp.,
Hawthorne, Calif.

A. F. MILLS
Assistant Professor of
Engineering and Applied Science,
University of California,
Los Angeles, Calif.
Assoc. Mem. ASME

Highly Accelerated Compressible Laminar Boundary Layer Flows With Mass Transfer[1]

Exact numerical solutions have been obtained for highly accelerated self-similar laminar boundary layer flows with and without mass transfer. Values of the acceleration parameter β in the range 0 to 20 were considered. Variable gas properties were realistically modeled by assuming $\rho \propto h^{-1}$, $\mu \propto h^{\omega}$, and Pr = *constant. The results presented show the dependence of wall shear stress, heat transfer rate, and displacement thickness on the problem parameters which include β, Mach number, wall enthalpy ratio, mass transfer rate, ω and* Pr. *The inadequacy of solutions obtained under the simplifying assumptions of* Pr = *1.0 and ω = 1.0 is clearly displayed. The numerical solution procedure employed proved quite adequate for a class of problem which has presented serious difficulties to previous investigators.*

Introduction

Highly accelerated laminar boundary layer flow, in regions of large favorable pressure gradient, are found in a number of engineering situations. Of particular interest is flow in a rocket nozzle throat, and flows over a supersonic compression cone or blunt hypervelocity vehicle. These flows are generally nonsimilar in character and their exact analytical prediction requires the direct solution of the partial differential form of the governing conservation equations. However, a simpler approach, which often yields adequate estimates of the wall shear stress and heat transfer rate, is the method of local similarity, wherein the boundary layer behavior is assumed to be a function of local parameters only. Lees [1][2] proposed the local similarity method for the calculation of heat transfer from accelerated laminar boundary layers over cooled surfaces. Back and Witte [2] showed that the method gave good heat transfer predictions for much larger values of the free-stream acceleration parameter, β, than originally considered by Lees. More recently Marvin and Sinclair [3] investigated flow over the shoulder of a cooled, flat-faced cylinder and showed that the local similarity method gave predictions of shear stress and heat transfer which were in good agreement with the results of exact nonsimilar calculations. Adequate agreement with experimental heat transfer data was also demonstrated. Thus, similarity solutions for highly accelerated flows have practical utility when used in conjunction with the assumption of local similarity. In addition, such solutions conveniently exhibit the effects of various flow parameters such as free-stream acceleration, Mach number, wall enthalpy ratio, real gas property variations, and mass transfer rate.

The engineering problems mentioned above are characterized by all or some of the following features: (*i*) a large temperature difference across the boundary layer, (*ii*) a high free-stream Mach number, (*iii*) surface mass transfer. These features put constraints on the simplifying assumptions which can realistically be used when obtaining solutions to the governing equations. A large temperature difference implies that the often-used convenient simplification of a constant density–viscosity product across the boundary layer is inappropriate and more realistic gas property variations should be considered. If the Mach number is appreciable the assumption of unity Prandtl number is inappropriate since viscous dissipation effects are thereby oversimplified. These two simplifying assumptions have been used by a number of authors, the most recent study being that of Back [4] who considered flows with values of the free-stream acceleration parameter β from 0 to 20. The reader is also referred to [4] for a review of earlier work on accelerated boundary layers. Dewey and Gross [5] employed realistic gas properties ($\rho \propto h^{-1}$, $\mu \propto h^{\omega}$, Pr = constant) and obtained similarity solutions for β up to 5, with the effects of mass addition included. The same authors obtained solutions for the limiting condition of $\beta \rightarrow \infty$

[1] Computer time for the numerical calculations was provided by the Campus Computing Network of the University of California, Los Angeles, Calif.

[2] Numbers in brackets designate References at end of paper.

Contributed by the Heat Transfer Division and presented at the Space Technology and Heat Transfer Conference, Los Angeles, Calif., June 21–24, 1970, of The American Society of Mechanical Engineers. Manuscript received by the Heat Transfer Division March 31, 1970; revised manuscript received October 21, 1970; final revision received March 4, 1971. Paper No. 70-HT/SpT-34.

where a singular perturbation problem obtains in which the velocity boundary layer thickness is of the order $\beta^{-1/2}$ with respect to a total enthalpy layer of order unity. Dewey and Gross note that exact numerical solutions are very difficult to obtain for values of β greater than 2. The nonuniform convergence of $f'(\eta)$ near the wall for $\beta \to \infty$ presents calculational difficulties even for moderate values of β. As a result very few numerical solutions for $\beta > 2$ are in fact presented in reference [5].

The objective of the present study was to obtain, using realistic gas property models, exact numerical boundary layer similarity solutions for a range of β from 0 to 20. These solutions allow the effect of β on such quantities as the wall shear stress, heat transfer rate, and displacement thickness to be clearly exhibited and also can be used for further evaluation of the lower limit of applicability of the asymptotic solutions for $\beta \to \infty$. However, we view the present study as having a deeper significance inasmuch as we have demonstrated that our calculation procedure is quite satisfactory for high β flows. The way is now clear for studies of more complex high β flow problems. After all, real flows with mass transfer invariably involve foreign gases and chemical reactions. Furthermore, even the relatively simple question of the behavior of the recovery factor in high β flows of a perfect gas is yet to be resolved [4, 5].

Analysis

The coordinate system is chosen such that s is measured along, and y perpendicular to, the surface; the corresponding velocity components are u and v, respectively. For steady laminar boundary layer flow the governing equations for a perfect gas are

$$\text{mass:} \qquad \frac{\partial}{\partial s}(\rho u r^{\epsilon}) + \frac{\partial}{\partial y}(\rho v r^{\epsilon}) = 0 \tag{1}$$

$$\text{momentum:} \qquad \rho u \frac{\partial u}{\partial s} + \rho v \frac{\partial u}{\partial y} = -\frac{dp}{ds} + \frac{\partial}{\partial y}\left(\mu \frac{\partial u}{\partial y}\right) \tag{2}$$

$$\text{total enthalpy:} \qquad \rho u \frac{\partial H}{\partial s} + \rho v \frac{\partial H}{\partial y} = \frac{\partial}{\partial y}\left(k \frac{\partial T}{\partial y}\right) + \frac{\partial}{\partial y}\left(\mu u \frac{\partial u}{\partial y}\right) \tag{3}$$

The geometrical index ϵ assumes a value of 1 for axisymmetric flows and 0 for planar ones. Second-order boundary layer effects such as transverse curvature will be neglected. External force fields and radiative energy transport are absent. The boundary conditions imposed on the set of equations are

$$\begin{aligned} y = 0: \quad & u = 0 \\ & \rho v = \dot{m} \\ & H = h_s \end{aligned} \tag{4}$$

$$\begin{aligned} y \to \infty: \quad & u \to u_e \\ & H \to H_e \end{aligned} \tag{5}$$

Following Lees [1] the transformation $x, y \to \xi, \eta$ is made where the Levy and Mangler transformations have been combined in defining

$$\eta = \frac{\rho_e u_e}{(2\xi)^{1/2}} \int_0^y r^{\epsilon} \frac{\rho}{\rho_e} dy \tag{6}$$

$$\xi = \int_0^s \rho_e \mu_e u_e r^{2\epsilon} ds \tag{7}$$

A stream function ψ is introduced such that

$$\rho u r^{\epsilon} = \frac{\partial \psi}{\partial y}; \qquad \rho v r^{\epsilon} = -\frac{\partial \psi}{\partial s} \tag{8}$$

and choosing $\psi(\xi, \eta) = (2\xi)^{1/2} f(\eta)$ leads to $u/u_e = \partial f/\partial \eta \equiv f'$. Under this transformation the conservation equations for self-similar flows become

$$\text{momentum:} \qquad (Cf'')' + ff'' = \beta^0 \left(f'^2 - \frac{\rho_e}{\rho}\right) \tag{9}$$

$$\text{total enthalpy:} \qquad \left(\frac{C}{\mathrm{Pr}} g'\right)' + fg' = E\left[2C\left(\frac{1}{\mathrm{Pr}} - 1\right) f'f''\right]' \tag{10}$$

subject to the boundary conditions

$$\eta = 0: \qquad f' = 0, \quad f = f_s, \quad g = g_s \tag{11}$$

$$\eta \to \infty: \qquad f' \to 1, \quad g \to 1 \tag{12}$$

where

$$C = \frac{\rho\mu}{\rho_e \mu_e}; \quad \beta^0 = 2\frac{d \ln u_e}{d \ln \xi}; \quad g = \frac{H}{H_e}; \quad E = \frac{u_e^2}{2H_e}$$

Following Dewey and Gross [5], a model gas is chosen, with the properties

$$\rho \propto h^{-1}; \quad \mu \propto h^{\omega}; \quad \mathrm{Pr} = \text{constant}$$

thereby eliminating temperature level as a parameter of the problem. For the model gas equation (9) can be recast in the form

$$(Cf'')' + ff'' = \beta(f'^2 - g) \tag{13}$$

where $\beta = \beta^0/(1 - E)$. The parameter β is found to be more appropriate than β^0 for scaling pressure gradient effects in high Mach number flows. The problem parameters are therefore β, E, g_s, f_s, Pr, and ω. A value of the viscosity exponent ω equal to 1.0 yields the familiar constant density–viscosity product simpli-

Nomenclature

$C = \dfrac{\rho\mu}{\rho_e\mu_e}$

$E = \dfrac{u_e^2}{2H_e}$, Mach number or flow speed parameter

f = dimensionless stream function

$g = \dfrac{H}{H_e}$

h = enthalpy

H = total enthalpy

j = mass diffusive flux

k = thermal conductivity

$\dot{m}$ = mass transfer rate

p = pressure

Pr = Prandtl number

q = conductive heat flux

r = radius of an axisymmetric surface; recovery factor

Sc = Schmidt number

s, y = boundary layer coordinates

u, v = velocity components

$\beta^0 = 2\dfrac{d \ln u_e}{d \ln \xi}$

$\beta = \dfrac{\beta^0}{1 - E}$, acceleration parameter

δ_1 = displacement thickness

ϵ = geometrical index

η = transformed coordinate normal to the surface, equation (6)

μ = dynamic viscosity

ρ = density

ξ = transformed coordinate along the surface, equation (7)

τ = shear stress

ψ = stream function

ω = exponent in viscosity–enthalpy relation

Subscripts

e = free stream

s = surface

Superscripts

$'$ = differentiation with respect to η

$*$ = zero mass transfer

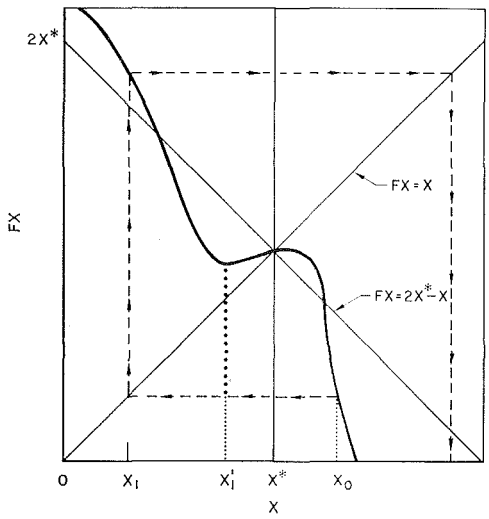

Fig. 1 Behavior of the operator *F*

fication ($C = 1.0$); $\omega = 0.7$ is appropriate for low-temperature flows while $\omega = 0.5$ may be regarded as a limiting value for high-temperature flows. Gross and Dewey [6] have demonstrated that solutions obtained for a power-law viscosity relation can be related to solutions obtained for the Sutherland viscosity law through the Eckert reference enthalpy. Fig. 8 of reference [6] suggests that $\omega = 0.5$ and 0.7 are the most appropriate exponents to use in parametric studies. Most of the present computations were performed for Pr = 0.715, a value appropriate for air and indeed most other gases. Although additional computations were performed with Pr = 0.740 and Pr = 1.0, it was not considered worthwhile to study parametrically the effect of Prandtl number.

In contrast to Back and Witte [2] and Back [4] we are not concerned that most of the solutions obtained do not have corresponding physically real self-similar flows. This viewpoint is in accord with our stated objectives of providing data for use in the local similarity method, and the study of the effects of various problem parameters, in particular β, E, g_s, and f_s.

Solution Procedure

The method of solution employed here was developed and applied to the computation of a wide range of boundary layer flow problems in [7]. Only a brief outline of the method will be given here to indicate the basic approach and its departure from techniques previously employed to solve the boundary layer equations. Reference [7] contains complete derivations, mathematical proofs, and illustrative examples of applications. The main feature of the method is the application of functional analysis to embed specific boundary layer problems in the complete class of self-similar three-dimensional multicomponent boundary layer flows. Thus, the general problem is considered in terms of an operator on the solution vector X whose components are the principal dependent variables of the conservation equations, i.e., $X = (\tau_1, \tau_2, q, j_1, \ldots, j_n)$, where τ_1, τ_2 are the shear stress functions in the principal directions, q is the conduction heat flux function, and j_i are the species diffusion flux functions. Inspection of the equations governing multicomponent three-dimensional boundary layer flows shows that they may be expressed in functional form as

$$\frac{dX}{d\eta} + GX = H$$

Formal integration of these equations, subject to the imposed boundary conditions, yields a relation which in functional form may be written as

$$X = FX$$

Here F is an operator on X, and is itself a function of X since it depends on the basic functions in the conservation equations. By casting the equations into this form, the problem is now viewed in terms of mapping of functions into themselves, and may be investigated using techniques of functional analysis. For constant-property boundary layers, the operator F is a known function whose characteristics are readily investigated by means of standard techniques of functional analysis. In such cases the applicability of simple iterative schemes such as

$$X_i = FX_{i-1}$$

may be ascertained by means of the Banach fixed-point theorem, e.g., Saaty [8], which assures convergence if the norm of the operator F is less than unity. The behavior of the operator on the solution vector is easily studied by means of simple analogues since all the conservation equations of boundary layer flows have the same functional form and, therefore, all the components of the solution vector have similar characteristics. Considerable insight into the solution procedure may be obtained from a study of the graph of norms of FX and X shown in Fig. 1. Since no confusion is likely at this point, the conventional notation for norms will be omitted in the graph and in the following discussion.

The investigation of reference [7] showed that the curve in Fig. 1 is quite representative of a wide class of constant-property boundary layer flow problems. It is readily seen that on the open sets in the two quadrants bounded by the functions $FX = X$ and $FX = 2X^* - X$, any iteration procedure will converge to the solution X^*. In the octants bounded by $FX = 2X^* - X$ and $X = X^*$, the Banach fixed-point theorem does not hold, and an iteration process will diverge. A typical example starting at X_0 is shown in the figure, with the arrows indicating the direction of the procedure. However, if instead of taking the first computed value of $X_1 = FX_0$ as the succeeding approximation, the range of F is restricted and some intermediate value X_1' is taken, then successive solutions are forced into the region where the Banach fixed-point theorem does apply. This behavior is shown by the dotted path in the figure.

The preceding discussion does not apply directly to variable-property flows, particularly when the $(\rho\mu)$ product varies appreciably across the boundary layer. The operator F is now a function of the current approximation to the solution vector; in fact the whole successive approximation procedure is a function of the initial guesses. The procedure now may be expressed in functional form as

$$X_i = F_{i-1}X_{i-1}$$

since only the previously computed values of C, ρ, Pr, and Sc are employed in the evaluation of the operator. In mathematically simple problems this complication presents no difficulties and it was found in reference [7] that, even with complex flow composition, straightforward iterative solutions are readily obtained for stagnation point and low Mach number flat-plate flows. Such problems are mathematically simple because the operator is a contraction mapping everywhere, and thus a convergent solution is obtained from any arbitrary initial value. The scarcity of published data for the mathematically difficult problems such as highly accelerated, variable-property flows, is due primarily to the inability of simple iterative techniques, or the more primitive "shooting" methods, e.g., Back [4], Dewey and Gross [5], to establish convergent sequences.

For variable-property flows no single function of F against X can be derived since the progress of the successive approximations depends on the initial values and also on the details of the calculation procedure. There is no direct correspondence between X and F since in the approximating sequence the value of F is one computing step behind the calculated value of X. In relatively simple problems the norm of the vector X is taken to be proportional to the integrals of the component of the vector. Thus in the simplest examples the restriction of the range of operator reduces to the well-known technique of averaging of successive

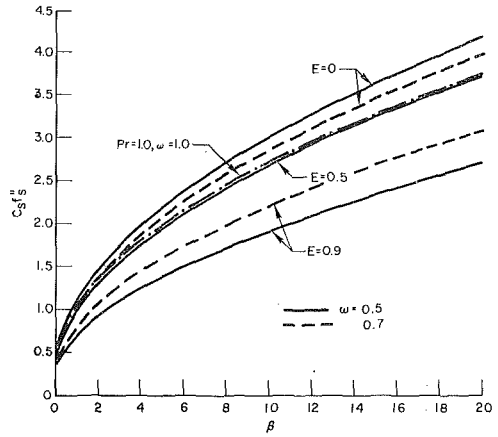

Fig. 2 Nondimensional shear stress $C_s f_s'' = \frac{\tau_s}{\rho_e u_e^2} \frac{(2\xi)^{1/2}}{r^\epsilon \mu_e}$ as a function of β: effect of E for $f_s = 0$. Pr = 0.740, ω = 0.5 unless otherwise specified.

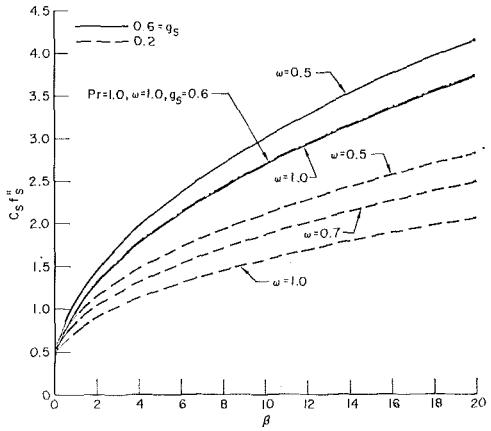

Fig. 3(a) Nondimensional shear stress $C_s f_s'' = \frac{\tau_s}{\rho_e u_e^2} \frac{(2\xi)^{1/2}}{r^\epsilon \mu_e}$ as a function of β: effect of ω for $E = 0$, $f_s = 0$. Pr = 0.715 unless otherwise specified.

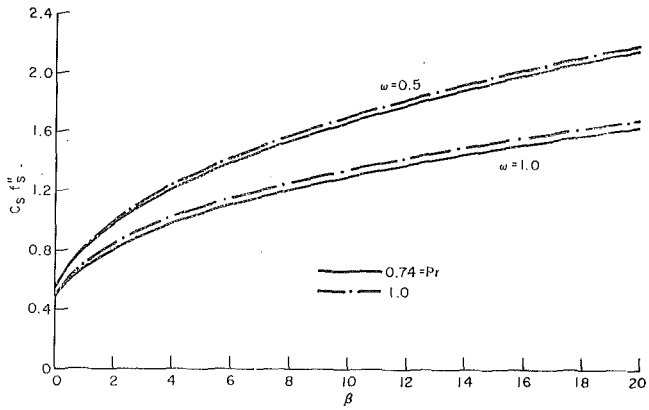

Fig. 3(b) Nondimensional shear stress $C_s f_s'' = \frac{\tau_s}{\rho_e u_e^2} \frac{(2\xi)^{1/2}}{r^\epsilon \mu_e}$ as a function of β: effect of ω and Pr. $E = 0.5$, $g_s = 0.1$, $f_s = 0$.

approximations. In difficult problems a more sophisticated approach is necessary, and not only must the norm of X be more carefully defined, but also the locus of the solution vector X must be selected to minimize the norm of F.

The locus of X toward the solution X^* is controlled by variation of the problem parameters Pr, g_s, ω, β, E, which are selected in such a way that the iteration process remains in the vicinity of the convergent quadrants. Ultimately the desired problem parameters and the imposed boundary conditions must be employed but, for efficient computations, a gradual relaxation of the parameters toward these final values has been found to be rather effective. In practice it was found convenient to restrict the range of the operator for all calculations because it was then possible to perform extensive parametric studies in a single pass through the computer. The resulting small increase in computer time was thought to be worth the convenience.

The highly accelerated flows studied here are particularly difficult to compute because the curve representing the functional relations is very steep (i.e., the norm of the operator is equal to or greater than one). In these cases it is necessary to approach the solution (i.e., the fixed point of the operator) very gradually by placing severe restrictions on the range of the operator. It appears that, as $\beta \to \infty$, the solution tends asymptotically to the line $X = X^*$, and a singular perturbation situation obtains. It is of some interest to note that the solution curves, which fall on the open sets in the octants bounded by $X = X^*$, $FX = X$, cannot be solved by the iterative techniques developed in reference [7] because no stable converging sequence can be established.

The accuracy and reliability of the method were demonstrated in reference [7] for a broad range of problem classes. In addition we present here Tables 1(*a*) and 1(*b*) which show comparisons of our data with those of Dewey and Gross [5] and Back [4], respectively. The good agreement displayed gives confidence in the reliability of our method. We estimate that the data obtained in the present study have at least 3-decimal-place accuracy, and 4-decimal-place accuracy for all cases where $\beta \leq 10$. The data were obtained in a series of parametric runs of about 60 cases each. The computation time on the IBM 360/91 computer was about 3 sec per case. No attempt was made to optimize the speed of the computations which consisted of elementary quadratures and property calculations.

Results and Discussion

Of primary engineering importance are the wall shear stress, the heat transfer rate, and the boundary layer dispacement thickness. Our objective is to demonstrate the manner in which these quantities depend on the problem parameters β, E, g_s, f_s, and ω. As mentioned in the Introduction, Back [4] has studied the problem in detail for an impermeable wall ($f_s = 0$) with the simplifying assumptions of Pr = 1 and $\omega = 1$. The reader is referred to [4] for a rather comprehensive discussion of the general features of high β flows. We shall focus here on the effects of ω, E for Pr $\neq$ 1, and mass transfer ($f_s \neq 0$). In this regard, the manner in which Back handled the Mach number parameter (here $u_e^2/2H_e$, referred to by Back as the flow speed parameter) requires some elaboration. Under the assumption of Pr = 1, and regarding β rather than β^0 as the acceleration parameter, E does not appear in the governing conservation equations. Thus, for example, Back's solution for the nondimensional wall shear stress, $C_s f_s''$, is a function of β and g_s only, and E affects the wall shear only through the scaling of β^0 in the relation $\beta = \beta^0/(1 - E)$. In contrast, we have taken Pr $\neq$ 1 and thus our solutions for $C_s f_s''$ (see, for example, Fig. 2) exhibit a marked dependence on E independent of that which is contained in β. Back does present boundary layer profiles and thicknesses which have both β and E as parameters; in transforming from the η plane to the physical plane Back reintroduces E as a parameter by arbitrarily assigning a value to E in the relation $h_e = (1 - E)H_e$. But, as can be seen from equation (10), Back's assumption of Pr = 1 conveniently eliminates the computationally awkward viscous dissipation term which is scaled by E. Also, his further assumption of $C = 1$ completely removes the E-dependence from the governing differential equations, equations (10) and (13), thereby greatly reducing the computational task. Since the main issue is the realistic representation of engineering problems, we do not believe that the

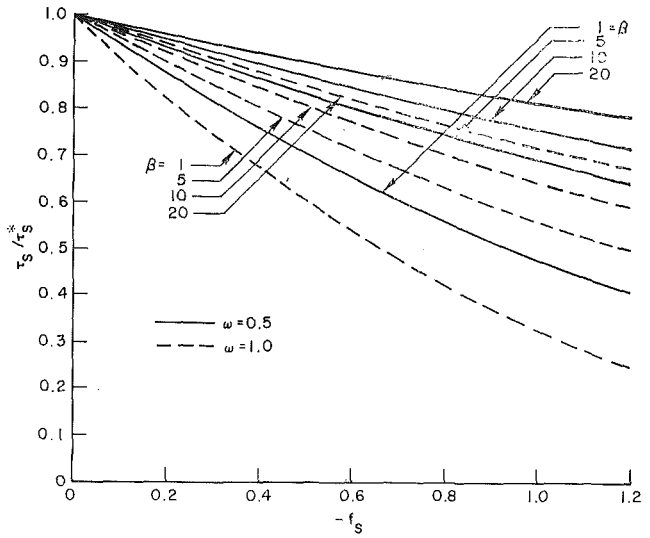

Fig. 4 Normalized shear stress as a function of mass injection rate: effect of ω. $E = 0$, Pr = 0.715, $g_e = 0.2$.

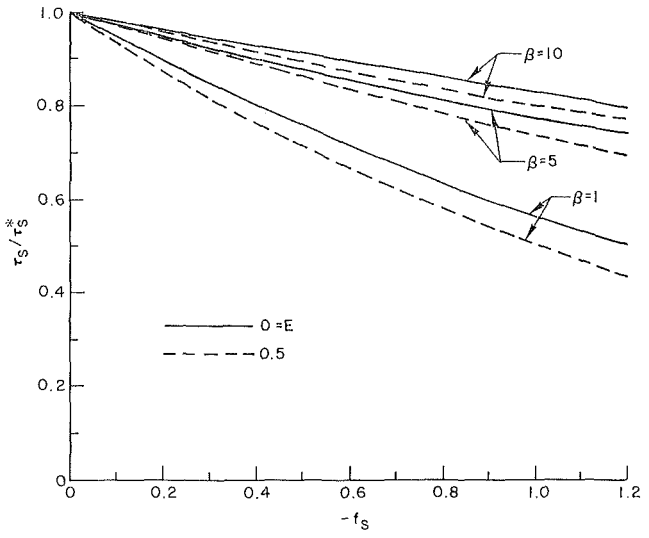

Fig. 5 Normalized shear stress as a function of mass injection rate: effect of E. Pr = 0.715, $g_e = 0.6$, $\omega = 0.5$.

effects of E displayed in reference [4] have engineering utility. Real gases have Pr $\neq$ 1 and $C \neq 1$; we do not see how Pr $\neq$ 1 effects, as a function of flow speed, can be ascertained from solutions of an energy equation which omits the viscous dissipation term. For example, Fig. 12(b) shows that there is little resemblance between profiles calculated following Back's approach, and our results for realistic gas properties. With the role to be played by E in the present study thus established, we now proceed to a detailed discussion of the results.

Wall Shear Stress. Fig. 2 shows the effect of the Mach number parameter E on the nondimensional wall shear stress $C_s f_s'' = [\tau_s/\rho_e u_e^2][(2\xi)^{1/2}/r^e \mu_e]$ for flow over an impermeable wall. The shear stress decreases quite markedly with increasing E, the ratio $\tau/\tau_{E=0}$ being comparatively insensitive to β. The $E = 0.5$, $g_s = 0.6$ curve nearly coincides with the Pr = 1.0, $\omega = 1.0$ curve; by chance these particular values of E and g_s give $C_s = 0.913$, which is close to unity. Figs. 3(a) and 3(b) show the results of considering a realistic viscosity–temperature relation. As expected, the effect of $\omega(\mu \propto h^\omega)$ is more marked for large enthalpy ratios across the boundary layer. The effect of wall cooling in reducing the effect of β on wall shear is clearly displayed in Fig. 3(a). This is, of course, the "heavy surface layer" concept first discussed by Lees [1]. The reference curves for Pr = 1 on Figs. 3(a) and 3(b) demonstrate the expected small effect of Pr on the shear stress, though the effect clearly increases with wall cooling.

Figs. 4 and 5 show the effect of mass injection on the wall shear stress. The results are presented in the conventional normalized form τ_s/τ_s^*, where τ_s^* is the corresponding value of the shear stress for zero mass transfer. Such normalization removes the major dependence on property variations, but as Fig. 4 in particular demonstrates, a residual dependence does remain. It can be seen that the effectiveness of injection in reducing the shear stress decreases markedly with increasing β. That this is to be expected may be deduced from the integral momentum balance of the boundary layer in the following manner. Comparison of, say, Figs. 2 and 5 shows that the absolute decrease in wall shear stress becomes substantially greater at high values of β. The inner layer, where the velocity adjusts to its free-stream value, becomes relatively thinner with increasing β, and hence the effect of injection on the wall velocity gradient becomes more marked. However, the integral momentum conservation equation indicates that, at high β, the momentum balance is essen-

Table 1(a) Comparison of numerical data with results obtained by Dewey and Gross [5]. Pr = 0.7, $\omega = 0.5$, $g_e = 0.15$.

β	E	Dewey & Gross [5]		Present Study	
		f_s''	g_s'	f_s''	g_s'
0.0	0.0	.2172	.1605	.2172	.1606
0.0	0.5	.2764	.1864	.2764	.1864
0.5	0.0	.2954	.1702	.2954	.1703
	0.5	.3785	.1995	.3785	.2000
	0.8	.5095	.2534	.5095	.2534
1.0	0.0	.3493	.1755	.3493	.1755
	0.5	.4483	.2067	.4483	.2066
	0.8	.6050	.2645	.6050	.2646
1.5	0.0	.3923	.1790	.3923	.1790
	0.5	.5040	.2115	.5040	.2115
2.0	0.0	.4290	.1816	.4290	.1816
	0.25	.4773	.1941	.4773	.1941
3.0	0.0	.4906	.1853	.4906	.1853

Table 1(b) Comparison of numerical data with results obtained by Back [4]. Pr = 1.0, $\omega = 1.0$, $E = 0$.

β	Back [4]		Present Study	
	f_s''	g_s'	f_s''	g_s'
0	.46960	.18784	.4696	.1879
0.5	.79520	.20914	.7952	.2092
2	1.3334	.23063	1.333	.2307
5	1.9824	.24575	1.982	.2458
10	2.7162	.25623	2.715	.2564
15	3.2789	.26173	3.276	.2619
20	3.7528	.26531	3.747	.2655

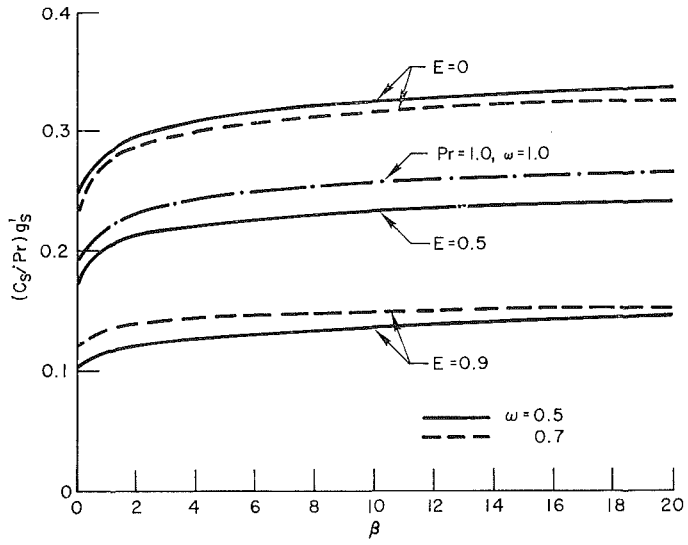

Fig. 6 Nondimensional heat transfer rate $\frac{C_s}{\mathrm{Pr}} g_s' = \frac{q_s}{\rho_e u_e H_e} \frac{(2\xi)^{1/2}}{r^\epsilon \mu_e}$ as a function of β: effect of E for $f_s = 0$. Pr = 0.740, $\omega = 0.5$ unless otherwise specified.

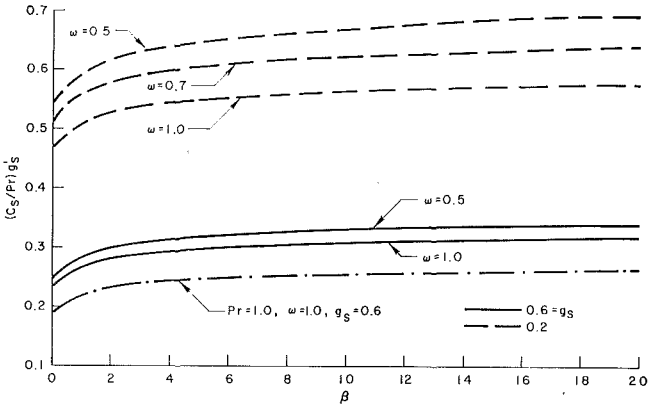

Fig. 7(a) Nondimensional heat transfer rate $\frac{C_s}{\mathrm{Pr}} g_s' = \frac{q_s}{\rho_e u_e H_e} \frac{(2\xi)^{1/2}}{r^\epsilon \mu_e}$ as a function of β: effect of ω and Pr. $E = 0.5$, $g_s = 0.1$, $f_s = 0$.

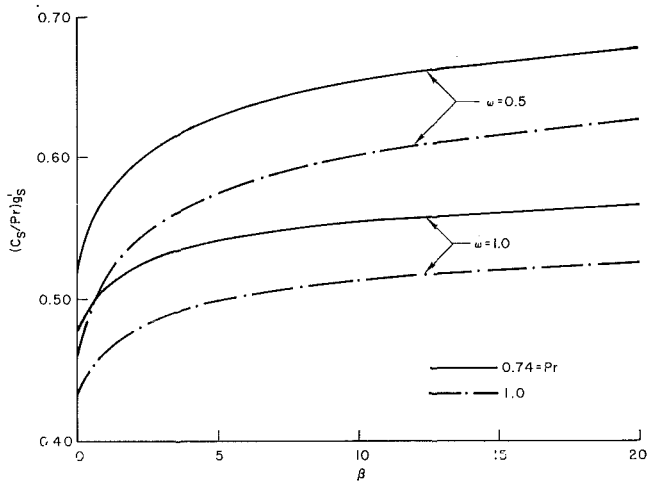

Fig. 7(b) Nondimensional heat transfer rate $\frac{C_s}{\mathrm{Pr}} g_s' = \frac{q_s}{\rho_e u_e H_e} \frac{(2\xi)^{1/2}}{r^\epsilon \mu_e}$ as a function of β: effect of ω for $E = 0$, $f_s = 0$. Pr = 0.715 unless otherwise specified.

tially between τ_s and the pressure gradient terms. A large value of τ_s obtains and consequently, on a percentage basis, there results the observed reduced effect of mass injection.

Heat Transfer Rate. Figs. 6, 7(a), and 7(b) show the nondimensional heat transfer rate $(C_s/\mathrm{Pr})g_s' = [q_s/\rho_e u_e H_e][(2\xi)^{1/2}/r^\epsilon \mu_e]$ as a function of β for flow along an impermeable wall. The relative insensitivity of heat transfer to β is due to the inner layer, where the velocity adjusts to its free-stream value, being of thickness order $\beta^{-1/2}$ with respect to a total enthalpy layer of order unity. Thus, in the limit $\beta \to \infty$ the heat transfer is independent of β and is given by the solution of the outer-layer equations. As $\beta \to \infty$ the thermal resistance becomes wholly contained in the outer layer where the velocity is independent of β. Fig. 7(b) shows that wall cooling has a rather insignificant effect on this insensitivity of heat transfer to β. Thus, a highly cooled wall is not required in order to exploit the local similarity approach in calculations of heat transfer at high β. The marked effect of the Mach number parameter E displayed in Fig. 6 is, of course, primarily due to viscous dissipation. A more appropriate ordinate would be a Stanton number based on the difference between the adiabatic wall and the wall enthalpies. However, in order to prepare such a graph, the dependence of the recovery factor r on β for variable-property flows is required. Back [4] states that Kemp, Rose, and Detra [9] found r to be independent of β for β up to 2 and E up to 0.75. But in reference [9], calculations of r were made only for $\beta^0 = 0$ and $^1/_2$, so that an independence was not firmly established. In contrast, Dewey and Gross [5] state that, although they have not been able to prove it analytically, it appears that $r = 1.0$ for all values of Pr, ω, and E in the limit $\beta \to \infty$. Finally, in [10] are presented extensive calculations of r for values of β up to 2 where it is demonstrated that r decreases with increasing β. A decrease of about 4 percent in the range $0 < \beta < 2$ is typical. For Pr = 0.71 values of r of about 0.80 at $\beta = 2$ are indicated; thus one must conclude that the uncertainty of r in the range $2 < \beta < 20$ might be even greater than 20 percent. Clearly further calculations of r for this range of β are necessary before meaningful Stanton numbers can be constructed for the presentation of heat transfer data.[3] Finally, as was the case for wall shear, the effect of ω on heat transfer, as displayed in Figs. 7(a) and 7(b), becomes more pronounced with increased wall cooling.

Figs. 8 and 9 show the effect of mass injection on the normalized heat transfer. In contrast to the normalized wall shear stress, q_s/q_s^* is relatively insensitive to β. The reason for this behavior is to be found in the argument given above which explained the insensitivity of heat transfer to β. The effect of injection on heat transfer must become independent of β as $\beta \to \infty$ as the equations governing the outer layer are independent of β in that limit.

Displacement Thickness. Fig. 10 shows the effect of β on the nondimensional displacement thickness

$$\int_0^\infty \left(\frac{\rho_e}{\rho} - f'\right) d\eta = \delta_1 \frac{\rho_e u_e r^\epsilon}{(2\xi)^{1/2}}$$

Clearly displayed is the well-known characteristic of δ_1, that of a decrease with wall cooling and even negative values when the mass velocity in the boundary layer becomes sufficiently high. The effect of viscous dissipation ($E = 0$) in increasing δ_1 is quite evident, as is the effect of β in reducing δ_1. The effect of β is again due to the inner layer thickness being of order $\beta^{-1/2}$ with respect to an energy layer of order unity, as illustrated by the velocity and enthalpy profiles in Fig. 12. Since $\rho_e/\rho = h/h_e$ for a perfect gas, it follows that

$$\int_0^\infty \left(\frac{\rho_e}{\rho} - \frac{u}{u_e}\right) d\eta$$

[3] Subsequent to the original presentation of this paper a computer program was developed for the calculation of high β recovery factors. For Pr = 0.715, $\omega = 0.5$, and $E = 0.7$, r was found to be as low as 0.7415 at $\beta = 20$. Detailed results are presented in reference [11].

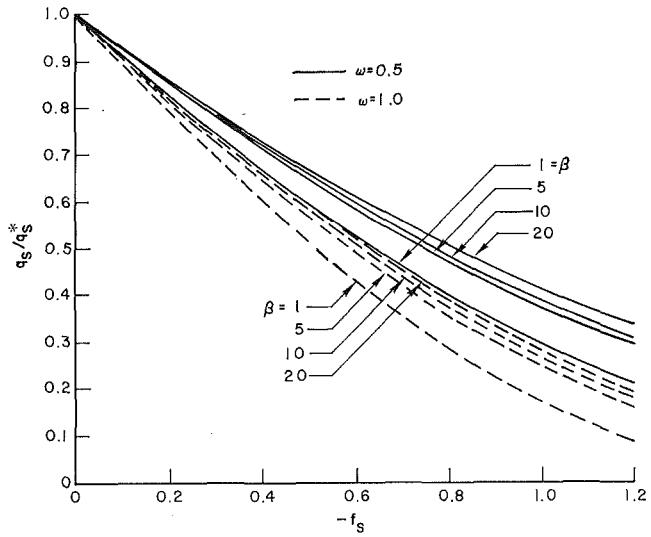

Fig. 8 Normalized heat transfer rate as a function of mass injection rate: effect of ω. $E = 0$, Pr = 0.715, $g_s = 0.2$.

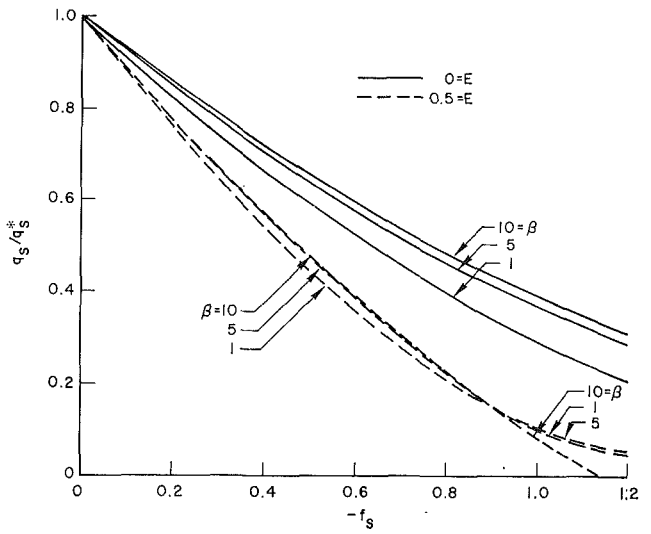

Fig. 9 Normalized heat transfer rate as a function of mass injection rate: effect of E. Pr = 0.715, $g_s = 0.6$, $\omega = 0.5$.

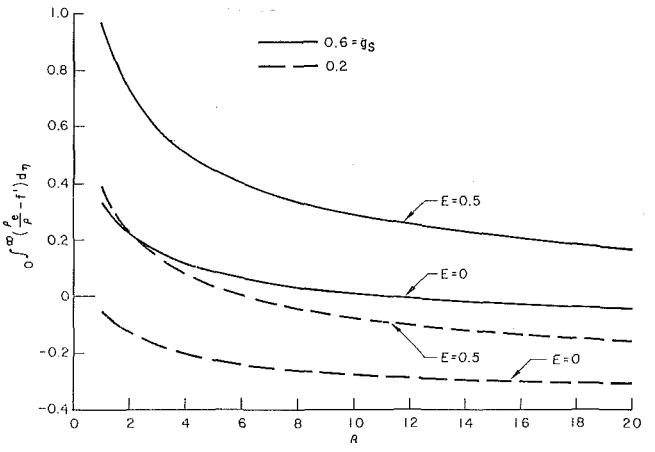

Fig. 10 Nondimensional displacement thickness $\int_0^\infty \left(\frac{\rho_e}{\rho} - f'\right) d\eta = \delta_1 \frac{\rho_e u_e r^\epsilon}{(2\xi)^{1/2}}$ as a function of β: effect of E. Pr = 0.715, $\omega = 0.5$, $f_s = 0$.

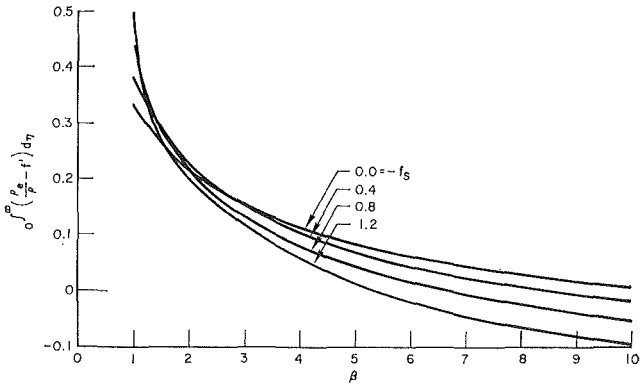

Fig. 11 Nondimensional displacement thickness $\int_0^\infty \left(\frac{\rho_e}{\rho} - f'\right) d\eta = \delta_1 \frac{\rho_e u_e r^\epsilon}{(2\xi)^{1/2}}$ as a function of β: effect of mass injection. $E = 0$, Pr = 0.715, $\omega = 0.5$, $g_s = 0.6$.

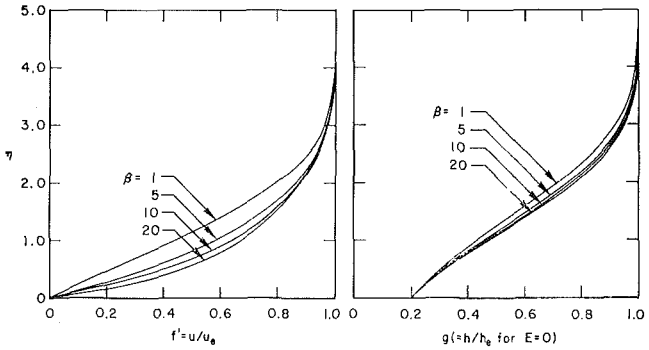

Fig. 12(a) Effect of β on velocity and enthalpy profiles. $E = 0$, Pr = 0.715, $\omega = 0.5$, $g_s = 0.2$, $f_s = 0$.

must decrease with increasing β.

Fig. 11 shows the effect of mass injection on δ_1; the range of β on this graph has been restricted since no additional features were apparent for $\beta > 10$. Of interest is the fact that, whereas at low values of β, mass transfer increases δ_1, at higher values of β the effect is reversed. This anomaly is explained in terms of the effect of injection on the velocity and enthalpy profiles. At low values of β, injection affects the displacement thickness primarily through the velocity profile and the behavior is as for incompressible flow. At high values of β, injection affects δ_1 primarily through the density profile as the velocity change is confined to the thin inner layer. Since $\rho_e/\rho = h/h_e$ the effect of injection on the density profile is in an opposite sense to the effect on the velocity profile. As can be seen from Fig. 11, these effects cancel in the range $1 < \beta < 3$ where δ_1 is relatively unaffected by injection. That the interesting behavior of δ_1 is encountered in the range $1 < \beta < 5$ is of some consequence in evaluating the importance of being able to obtain self-similar solutions for these values of β. The β values are too low for the $\beta \to \infty$ asymptotic solutions of Dewey and Gross [5] to be reliable, but nevertheless were large enough to present serious numerical difficulties for previous calculation procedures, and a resulting paucity of data.

Suction. Figs. 13 and 14 show the effect of suction on the wall shear stress and heat transfer for $E = 0$ and $E = 0.5$. In addition to its engineering significance, such data is useful for substantiating arguments about the physical nature of boundary layer flows. The marked increase in shear and heat transfer with suction is quite apparent; the basically linear behavior at high rates of suction indicates an approach to the asymptotic limit for strong suction investigated by Watson [12], Acrivos [13], and others.

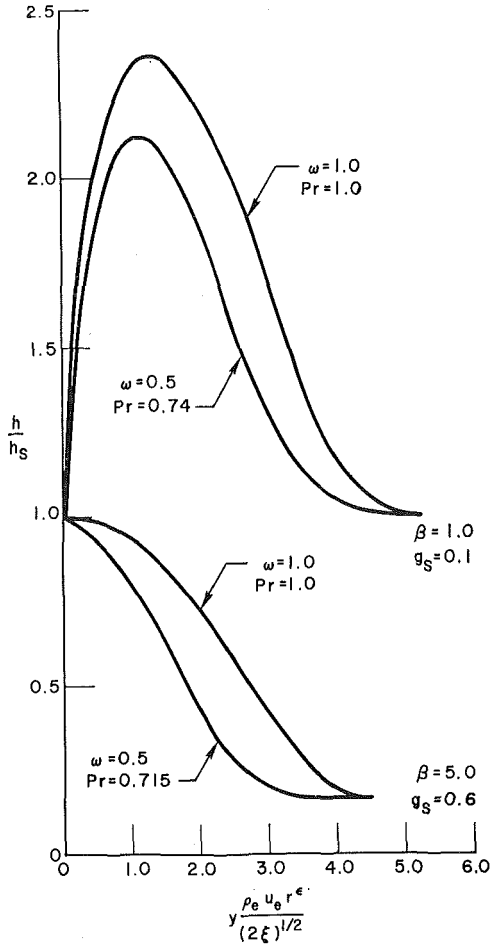

Fig. 12(b) Comparison of enthalpy profiles calculated according to Back's suggestion [4] and our exact results. $E = 0.9$, $f_s = 0$.

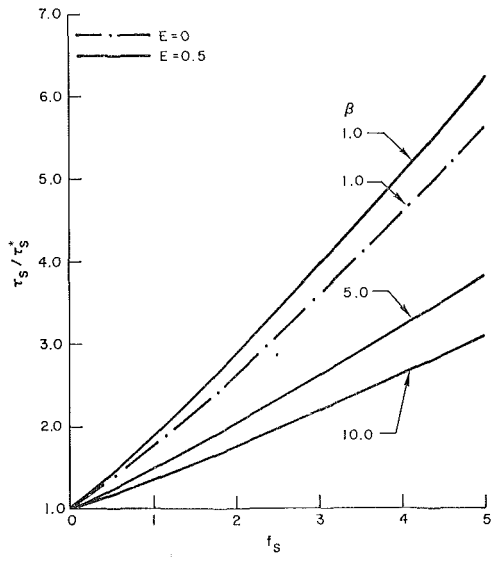

Fig. 13 Normalized shear stress as a function of mass suction rate: effect of β. Pr = 0.715, $\omega = 0.5$, $g_s = 0.2$.

Correlation of Property Variation Effects. Back and Witte [2] have proposed that data obtained for shear stress and heat transfer, under the assumption of $C = 1$, can be corrected for the effects of a more realistic viscosity law by introducing a factor C_s^n, independent of β and E. A value of n equal to 0.12 was suggested for shear stress and 0.10 for heat transfer. Since the correction is usually modest, the proposal has merit for engineering purposes. With values of $E = 0$ particularly in mind, Back [4] reevaluated this proposal and was uncertain as to the kind of correction, if any, that should be made, and indeed gives no recommendation. In order to examine the merits of the correction proposed by Back and Witte [2], we present in Table 2 values of τ' defined by the equation

$$\tau' = \frac{C_s^{0.12}\tau_s \quad (\mathrm{Pr} = 1.0, \omega = 1.0)}{\tau_s \quad (\mathrm{Pr} = 0.740, \omega = 0.5)} \tag{14}$$

Table 2 shows that the correction is quite useful at low values of E, but fails to handle the data for $E = 0.9$. The correction $C_s^{0.12}$ was essentially based on variations of C_s due to wall cooling; it is clear that variations of C_s due to Mach number are not related to shear stress in the same manner. In addition we note

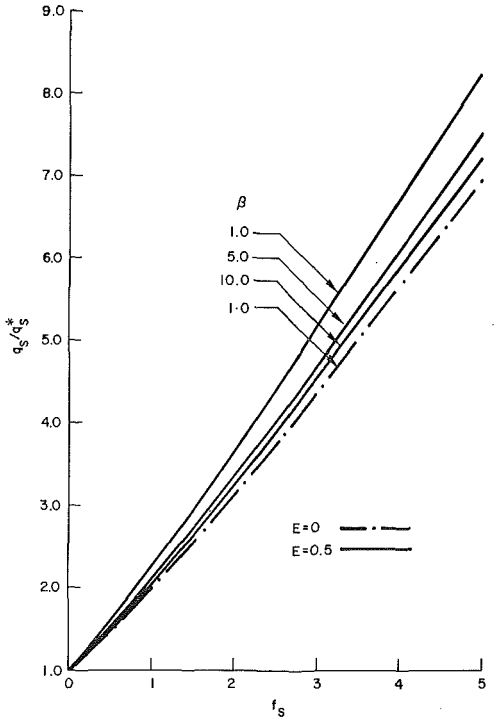

Fig. 14 Normalized heat transfer rate as a function of mass suction rate: effect of β. Pr = 0.715, $\omega = 0.5$, $g_s = 0.2$.

Table 2 Ratio of wall shear calculated according to the suggestion of Back and Witte [2] to the corresponding exact value; τ' is defined by equation (14). Pr = 0.740, $\omega = 0.5$, $g_s = 0.6$, $f_s = 0$.

β	τ'		
	E = 0 C_s = 1.291	E = 0.5 C_s = 0.913	E = 0.9 C_s = 0.408
0.0	.970	1.047	1.322
0.5	.960	1.040	1.325
1.0	.954	1.030	1.319
2.0	.946	1.025	1.306
5.0	.937	1.015	1.292
10.0	.931	1.006	1.280
15.0	.927	1.002	1.276
20.0	.925	.999	1.266

that errors would be incurred by assuming the correction to be independent of mass transfer. For example, in Figs. 4 and 5, the effects of β, ω, and E displayed would require a correction over and above a zero mass transfer correction contained in τ_s^*. For $E \neq 0$ it would be of interest to explore the possibility of obtaining a correlation based on C evaluated at the Eckert reference enthalpy, rather than on C_s. However, as was the case in correlating heat transfer, the uncertainty with respect to the recovery factor at high β precludes such an evaluation at the present time.

Conclusions

Satisfactory solutions of compressible laminar boundary layer flow with mass transfer can be obtained only by considering realistic property variations. The often-used simplifying assumptions of $\mu \propto h$ and $\Pr$ = unity leads to significant errors in the wall shear and heat transfer rate. The numerical solution procedure employed proved adequate for this class of problem; its use is indicated for the study of more complex high-β laminar boundary layer flows.

References

1 Lees, L., "Laminar Heat Transfer Over Blunt-Nosed Bodies at Hypersonic Flight Speeds," *Jet Propulsion*, Vol. 26, 1956, pp. 259–269.

2 Back, L. H., and Witte, A. B., "Prediction of Heat Transfer From Laminar Boundary Layers, With Emphasis on Large Free-Stream Velocity Gradients and Highly Cooled Walls," JOURNAL OF HEAT TRANSFER, TRANS. ASME, Series C, Vol. 88, No. 3, Aug. 1966, pp. 249–256.

3 Marvin, J. G., and Sinclair, A. R., "Convective Heating in Regions of Large Favorable Pressure Gradient," *AIAA Journal*, Vol. 5, 1967, pp. 1940–1948.

4 Back, L. H., "Acceleration and Cooling Effects in Laminar Boundary Layers—Subsonic, Transonic and Supersonic Speeds," *AIAA Journal*, Vol. 8, 1970, pp. 794–802.

5 Dewey, C. F., and Gross, J. F., "Exact Similar Solutions of the Laminar Boundary Layer Equations," *Advances in Heat Transfer*, edited by J. P. Hartnett and T. F. Irvine, Jr., Academic Press, New York, 1967, Vol. 4, pp. 317–446.

6 Gross, J. F., and Dewey, C. F., Jr., "Similar Solutions of the Laminar Boundary-Layer Equations with Variable Fluid Properties," *Archiwum Mechaniki Stosowanej*, Vol. 3, 1964, pp. 761–780.

7 Wortman, A., "Mass Transfer in Self-Similar Laminar Boundary-Layer Flows," PhD dissertation, School of Engineering and Applied Science, University of California, Los Angeles, Calif., 1969.

8 Saaty, T. L., *Modern Nonlinear Equations*, McGraw-Hill, New York, 1967.

9 Kemp, N. H., Rose, P. H., and Detra, R. W., "Laminar Heat Transfer Around Blunt Bodies in Dissociated Air," *Journal of the Aerospace Sciences*, Vol. 26, 1959, pp. 421–430.

10 Wortman, A., Mills, A. F., and Soo-Hoo, G., "The Effect of Mass Transfer on Recovery Factors in Laminar Boundary Layer Flows," to appear in *International Journal of Heat and Mass Transfer*.

11 Wortman, A., and Mills, A. F., "The Recovery Factor for Highly Accelerated Boundary Layers," to appear in *AIAA Journal*.

12 Watson, E. J., "The Asymptotic Theory of Boundary Layer Flow with Suction," *NACA Reports and Memoranda*, No. 2619, 1947.

13 Acrivos, A., "Mass Transfer in Laminar Boundary Layers with Finite Interfacial Velocities," *AIChE Journal*, Vol. 6, 1960, pp. 410–414.

J. R. GREEN
Graduate Student.

E. G. HAUPTMANN
Associate Professor.
Assoc. Mem. ASME

Department of Mechanical Engineering,
The University of British Columbia,
Vancouver B. C., Canada

Forced Convection Heat Transfer From a Cylinder in Carbon Dioxide Near the Thermodynamic Critical Point

*In an attempt to determine the heat transfer rates in forced flow normal to a heated cylinder and to provide some insight into the mechanisms in heat transfer in the critical region, heat transfer rates have been measured for both free and forced flow of supercritical carbon dioxide normal to a horizontal heated cylinder. The 0.006-*in-dia *cylinder was held at various constant temperatures by a feedback circuit. The effects of bulk fluid temperature, bulk fluid pressure, and surface temperature were studied for a range of bulk fluid temperatures and pressures from 0.8 to 1.4 times the critical temperature and pressure, and free-stream velocities from 0 to 3* fps. *The temperature difference between the heated cylinder and the bulk fluid was varied from 1 to 300* deg F. *Several photographs of the flow field are presented. In a supercritical fluid the heat transfer* rate *increases smoothly and monotonically with increasing temperature difference, increasing velocity, and increasing pressure. In fluid with the bulk temperature below the pseudo-critical temperature the heat transfer* coefficient *shows large peaks when the cylinder temperature is near the pseudo-critical temperature. The heat transfer* coefficient *decreases with increasing temperature difference when the bulk fluid temperature is above the pseudo-critical temperature. Supercritical forced convection does not exhibit the characteristic maximum in heat transfer* rate *shown in forced-flow nucleate boiling. Heat transfer* rates *at larger temperature differences are very similar in forced-flow film boiling and supercritical forced-flow heat transfer. With this horizontal constant-temperature cylinder, no "bubble-like" or "boiling-like" mechanisms of heat transfer were observed in supercritical free or forced convection.*

Introduction

Heat transfer in fluids in the critical region has become of great importance in the last 15 years due to the very high heat transfer rates possible in this region. Current applications include supercritical water in water steam once-through boilers in power stations, and supercritical hydrogen as the coolant and fuel in large-thrust regeneratively cooled rocket engines. Proposed applications are supercritical methane as a coolant and fuel for the supersonic transport, and supercritical carbon dioxide as the working fluid in an entirely supercritical turbine power cycle.

Of more fundamental interest, heat transfer to a fluid near the critical state is an extreme example of variable-property heat transfer. There is some dispute as to whether the heat transfer rates in a near-critical fluid can be explained by the intense fluid property variations alone. Unusual mechanisms of heat transfer, such as pseudo-boiling [1][1] and a penetration model [2], have been proposed. To date the fundamental mechanisms of critical region heat transfer are not completely understood.

The terminology commonly used in describing near-critical fluids is summarized in Fig. 1. Typical property variations in supercritical CO_2 are shown in Fig. 2.

Most work in supercritical fluids has been concerned with flow inside heated tubes. This geometry is of immediate engineering interest and while some design correlations have been obtained only limited theoretical work has been done. Reference [3] is a survey of heat transfer to supercritical fluids in internal flows. Reference [4] is a more complete survey of heat transfer to supercritical fluids in both internal and external flows. These surveys show that workers have been able to predict heat transfer rates and correlate experimental data only in parts of the critical region.

This study was primarily concerned with forced-convection

Contributed by the Heat Transfer Division and presented at the Space Technology and Heat Transfer Conference, Los Angeles, Calif., June 21–24, 1970, of The American Society of Mechanical Engineers. Manuscript received by the Heat Transfer Division March 30, 1970; revised manuscript received October 22, 1970. Paper No. 70-HT/SpT-36.

[1] Numbers in brackets designate References at end of paper.

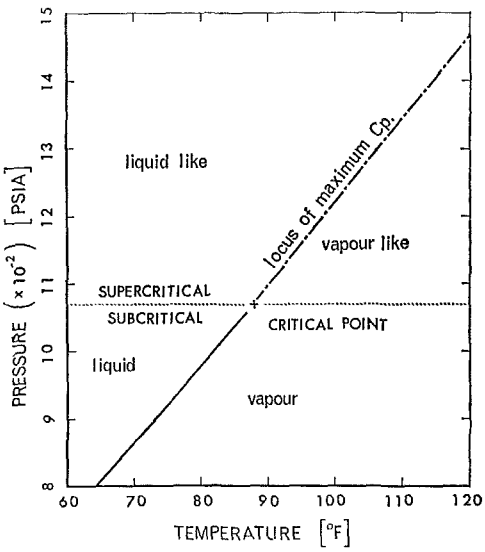

Fig. 1 Summary of near-critical region terminology

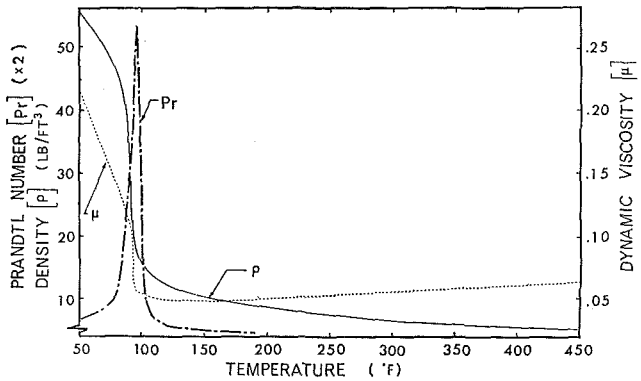

Fig. 2 Typical property variations in near-critical carbon dioxide

heat transfer normal to a heated cylinder in a supercritical fluid. Carbon dioxide with critical pressure of 1071 psia and critical temperature of 87.8 deg F was used as the working fluid. Various investigators have studied the problem of *free* convection from cylinders in supercritical fluids, with varied results. References [5–10] have worked with cylinders in carbon dioxide, [11] has worked in freon. The most complete studies are those of Goldstein [5] and Knapp [6] who reported heat flux differences of more than 100 percent for the same operating conditions. Both used a constant-flux cylinder, allowing the cylinder temperature to vary. Very limited work has been done in external flow with forced convection. Kato et al. [9] presented results for one pressure, one free-stream velocity, and five bulk temperatures for temperature differences less than 25 deg F for a cylinder in cross-flow. By using integrated mean bulk fluid properties Kato correlated his data to ±25 percent but was unable to comment on the mechanism of heat transfer.

Sabersky and Hauptmann [12] studied forced convection in external flow past a flat plate also in near-critical CO_2. Results showing the effect of bulk temperature, pressure, and free-stream velocity for flow over a heated flat plate were presented. Visual studies of the mechanism of heat transfer were included and observed peaks in the heat transfer coefficient were concluded to be primarily due to the large property variations in a fluid near the critical point.

The present study is an attempt to determine heat transfer rates in forced flow normal to a heated cylinder held at constant temperatures and to provide some insight into the mechanisms and important variables influencing heat transfer in the critical region.

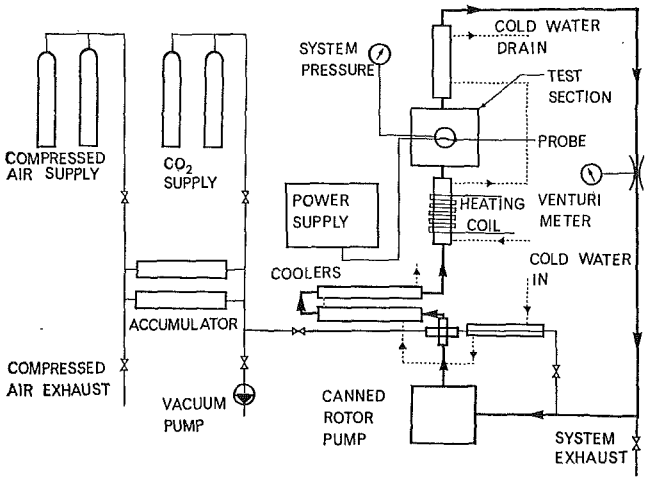

Fig. 3 Schematic of near-critical carbon dioxide forced-flow loop

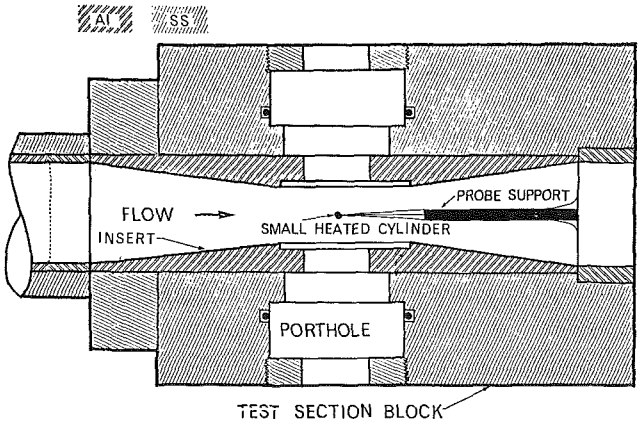

Fig. 4 Section of test section block

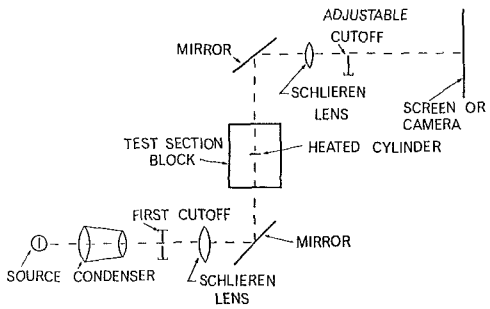

Fig. 5 Arrangement of Schlieren system

Experimental Equipment and Procedure

A closed-circuit test loop was used in this study. The test fluid was circulated through the test section at various velocities by a canned-rotor pump. The main test section was a vertical stainless steel tube 2 in. in diameter and 3 ft long with a removable test section block at mid-height. The test loop was arranged as shown in the schematic of Fig. 3. The test section block has been fitted with tempered Pyrex viewing ports as shown fn Fig. 4. The main flow was upward past the horizontal heated cylinder which was mounted in the optical path of the lens-type Schlieren system shown in Fig. 5. A flow conditioning section consisting of a packed Teflon wool matrix, a honeycomb section, and a series of very fine screens was located in the main test section upstream of the heated cylinder. Cold-water heat exchangers were used to control the bulk fluid temperature and free-piston accumulators were used to maintain bulk fluid pressure. Power

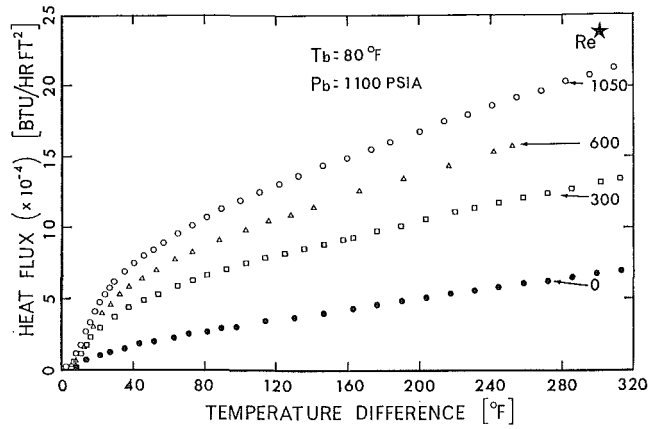

Fig. 6 Effect of velocity on heat transfer rate in CO_2 at 80 deg F and 1100 psia

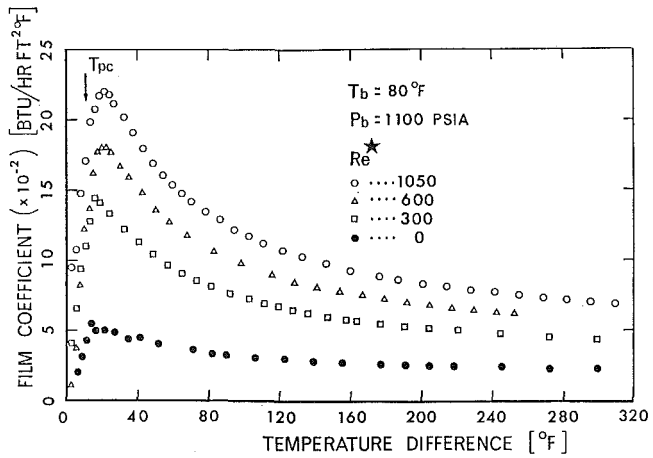

Fig. 7 Effect of velocity on heat transfer coefficient in CO_2 at 80 deg F and 1100 psia

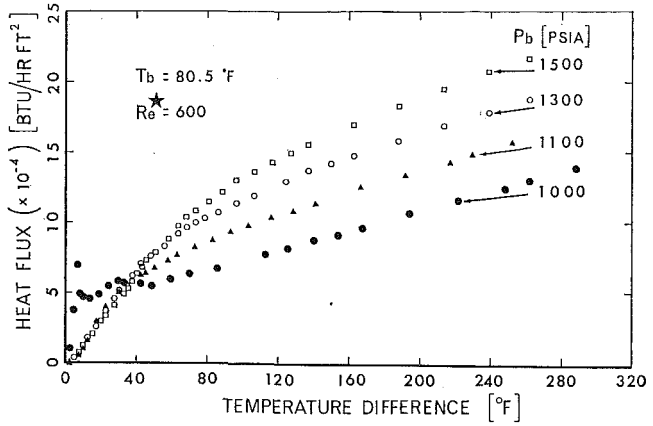

Fig. 8 Effect of bulk pressure on heat transfer rate at 80 deg F ($Re^* = 600$)

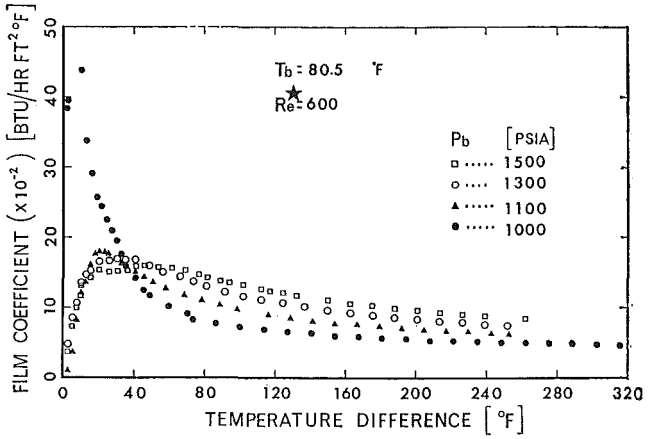

Fig. 9 Effect of bulk pressure on heat transfer coefficient at 80 deg F ($Re^* = 600$)

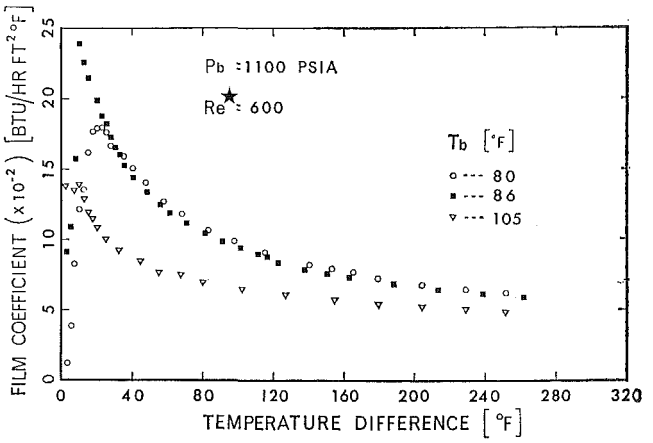

Fig. 10 Effect of bulk temperature on heat transfer coefficient at 1100 psia ($Re^* = 600$)

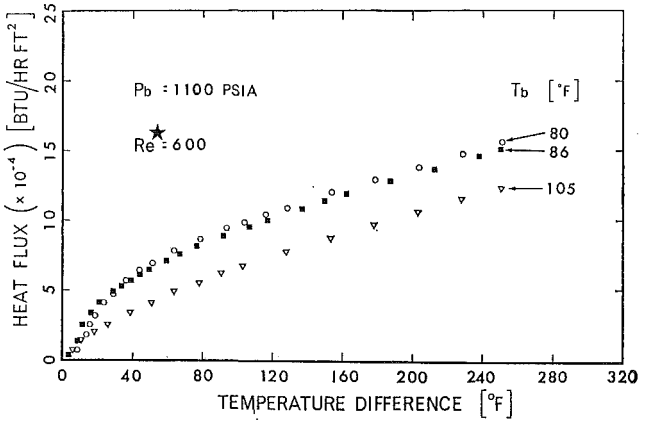

Fig. 11 Effect of bulk temperature on heat transfer rate at 1100 psia ($Re^* = 600$)

was supplied to the heated cylinder by a feedback bridge. The bridge is a hot-wire anemometer power supply, factory-modified to provide power levels of more than 2×10^6 Btu/ft²-hr.

The heated cylinders used in this study were either nichrome probes (0.003-in-dia) manufactured by the authors, or a gold-coated platinum-film quartz cylinder (0.006-in-dia) manufactured by Thermo-Systems Inc. The platinum-film probes were used for the bulk of the experimental work. They gave reproducible data and have a high temperature coefficient of resistivity which enables surface temperature to be accurately determined. Power dissipated by the heated cylinder was determined from the current flowing to the heated cylinder and the cylinder operating resistance.

The Schlieren image of the heated flow field was projected on a screen or directly on the film plane of either a Pentax 35-mm still camera, or a 16-mm high-speed Hycam movie camera. Still photos were taken at 1/1000-sec exposure and high-speed movies at 5000 frames per sec.

In order to obtain consistent results in free convection it was necessary to have the entire flow loop and the laboratory at the required bulk fluid temperature, and to begin the data runs with still fluid which had not been disturbed for at least 1 hr.

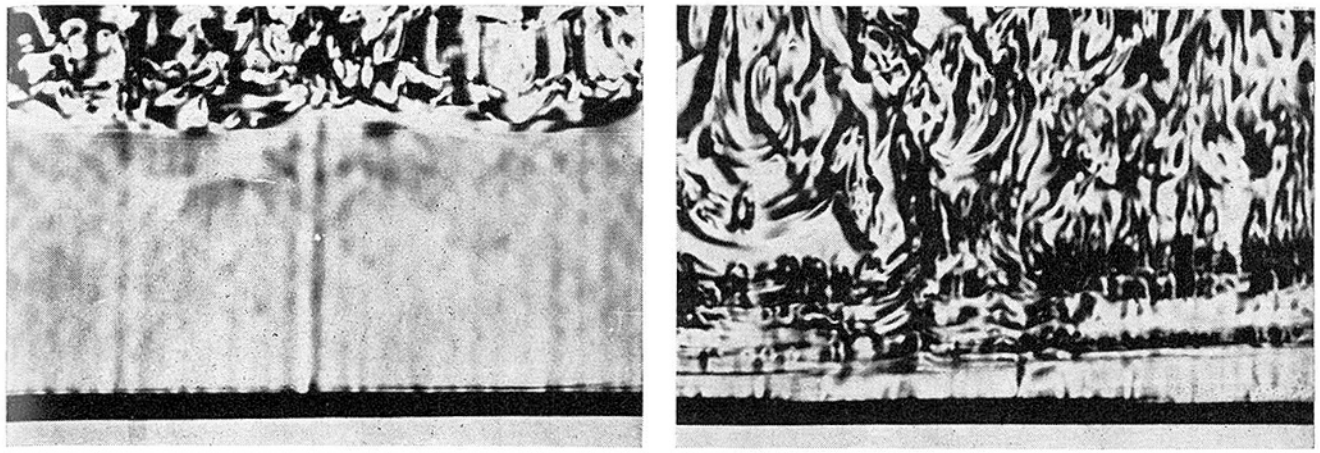

(a) Free convection

(b) $Re^* = 50$

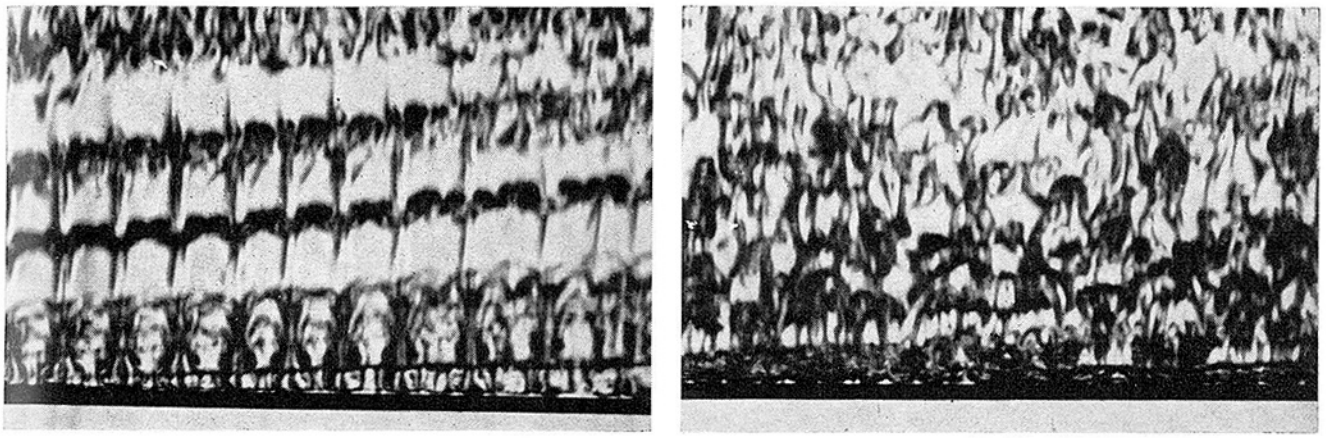

(c) $Re^* = 125$

(d) $Re^* = 375$

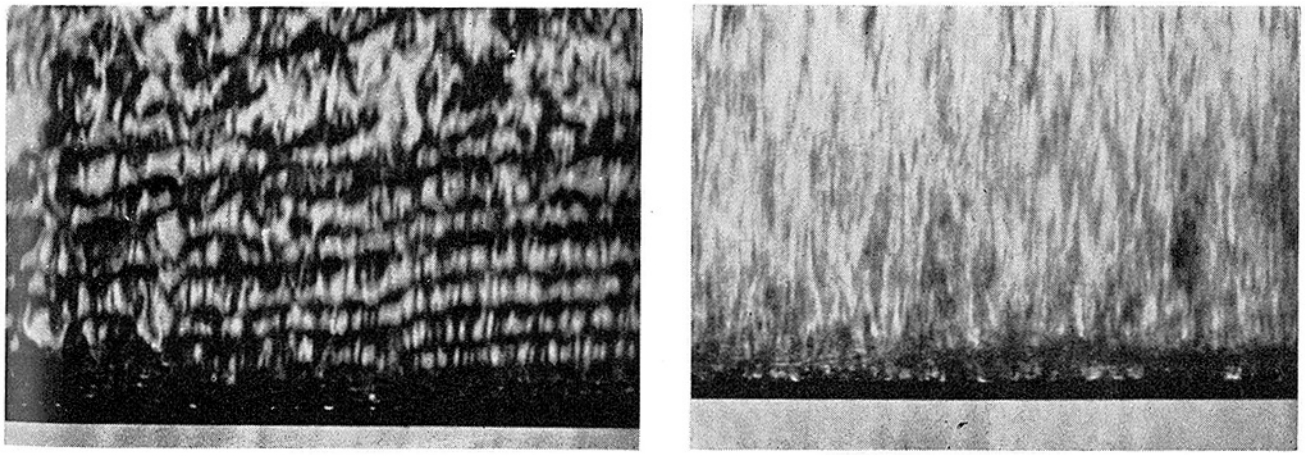

(e) $Re^* = 500$

(f) $Re^* = 1000$

Fig. 12 Effect of velocity on flow fields in forced convection normal to a heated cylinder in supercritical CO_2 (cylinder temperature = 380 deg F, fluid bulk temperature = 80 deg F, fluid bulk pressure = 1100 psia)

Forced-convection data runs were taken by setting the bulk pressure at the required pressure, setting the bulk temperature to the lower acceptable limit and running the apparatus until the bulk conditions stabilized and no change in pressure had been observed for approximately 15 min. Data points were taken in order of increasing temperature difference until the maximum temperature difference was reached, and then in order of decreasing temperature difference. Additional points were taken if the loop had to be stopped or the cooling rate changed at any point in the run. Photographs were taken either during the data run or in a separate test, and the operating points included as data points. Maximum bulk temperature difference from the desired test condition was ± 0.5 deg F. Maximum bulk system pressure difference was limited to ± 2.0 psia. The pressure was corrected by adding or releasing compressed air in the accumulator.

Experimental Results

Typical experimental results are presented in Figs. 6–11. Figs. 6 and 7 cover carbon dioxide at a bulk pressure of 1100 psia and a bulk temperature of 80 deg F (supercritical, liquid-like region). Results presented are for free convection as well as a range of free-stream velocities. For convenience, free-stream

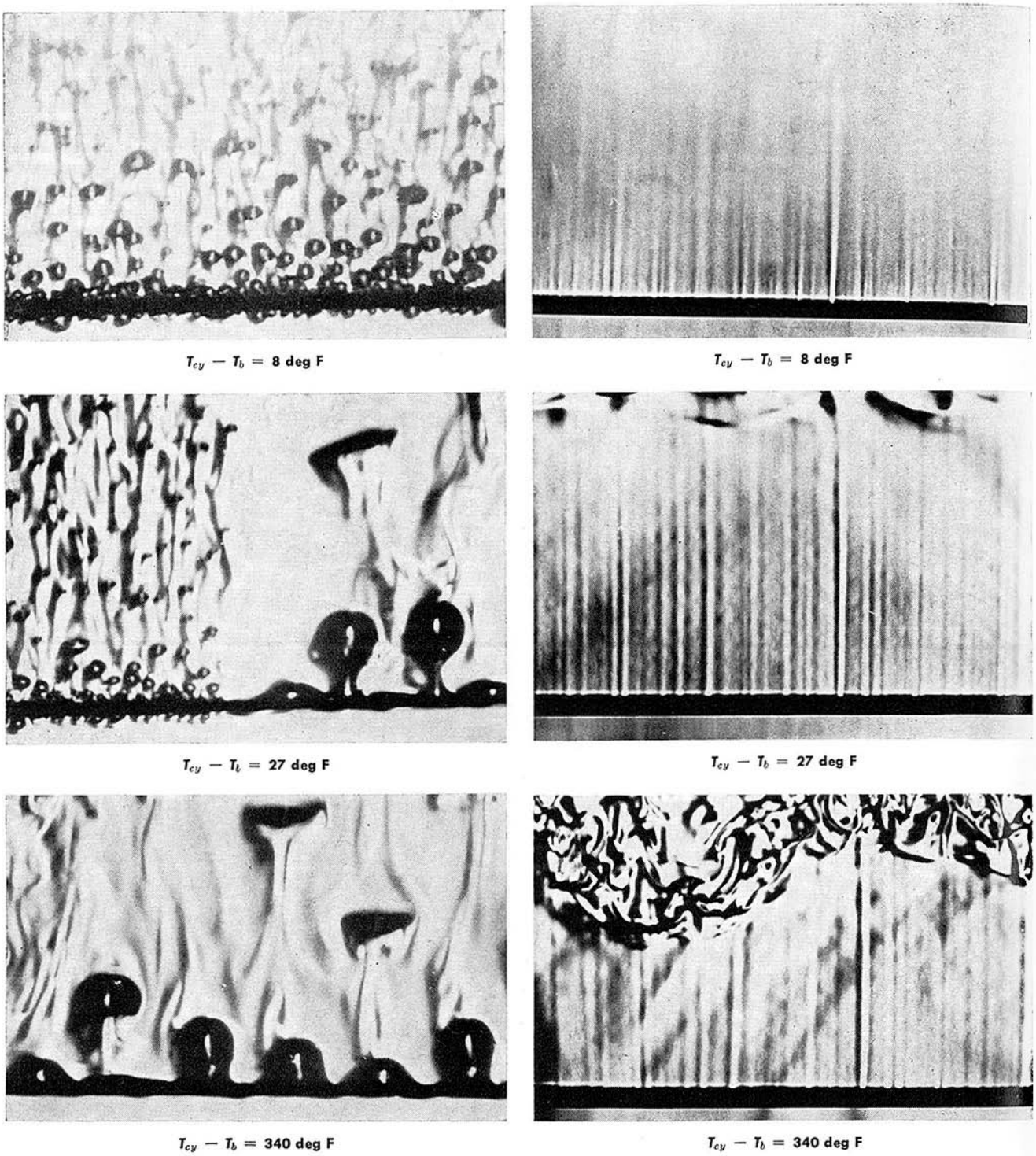

Fig. 13 Free-convection flow field variation with cylinder temperature; left column, subcritical, P_b = 1000 psia; right column, supercritical, P_b = 1100 psia

velocity is expressed in terms of an equivalent, constant-property Reynolds number (Re*) based on constant free-stream properties and cylinder diameter. Note that whenever the temperature difference is above 10 deg F the fluid very near the heated cylinder is above the pseudo-critical temperature and has vapor-like properties. Heat transfer rate increased with increasing temperature differences and increasing velocity. Even though the heat transfer *coefficient* displays large peaks when the cylinder temperature is slightly above the pseudo-critical temperature, the heat transfer *rate* is a smooth function of temperature difference for all velocities shown. The results presented are typical of data obtained at other operating conditions (80 to 105 deg F, 1300 and 1500 psia).

The effects of bulk pressure variation for a particular velocity are shown in Figs. 8 and 9. At subcritical pressures (1000 psia) the characteristic departure from nucleate boiling (DNB) maximum heat flux was observed. As the pressure was increased above the critical pressure the DNB peak disappeared. Heat transfer rates in supercritical CO_2 increased with increasing pressure for any given velocity and temperature difference. The heat transfer coefficients are nearly constant for both subcritical and supercritical cases for sufficiently high temperature difference (100 to 300 deg F).

The effects of bulk temperature variations for one velocity are shown in Figs. 10 and 11. Note that increasing bulk temperature results in a small increase in heat transfer coefficient when both

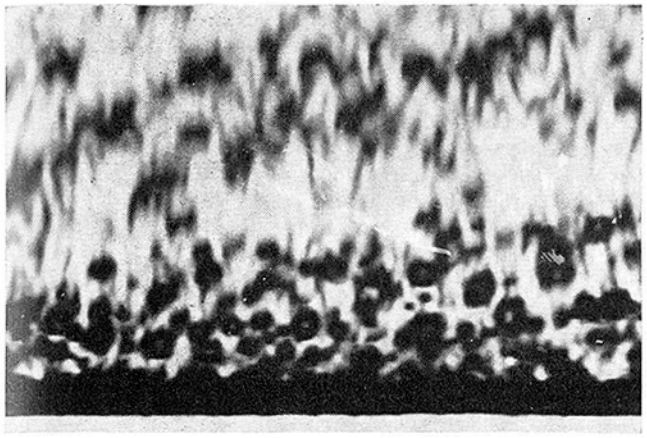

$T_{cy} - T_b = 8$ deg F

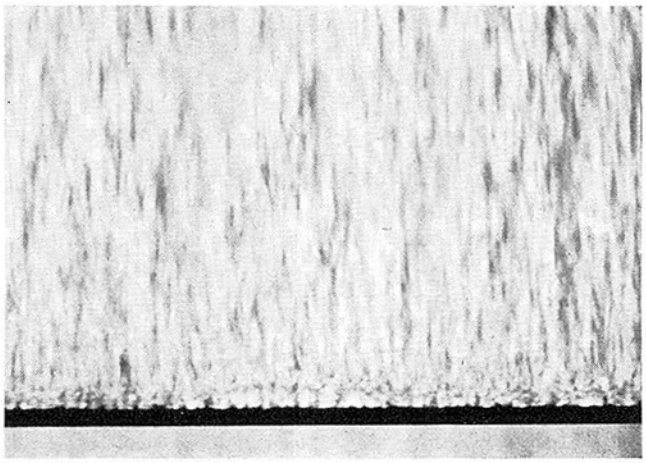

$T_{cy} - T_b = 8$ deg F

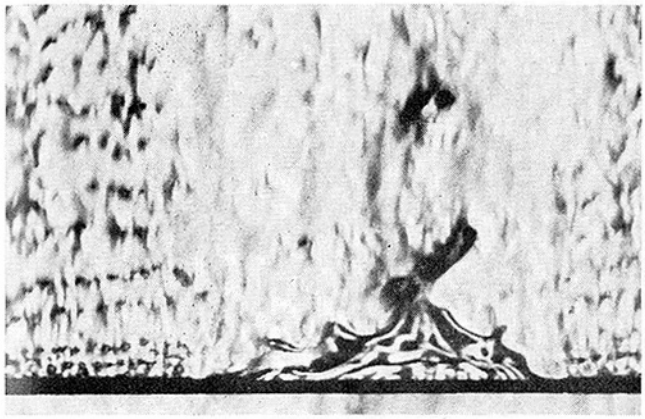

$T_{cy} - T_b = 27$ deg F

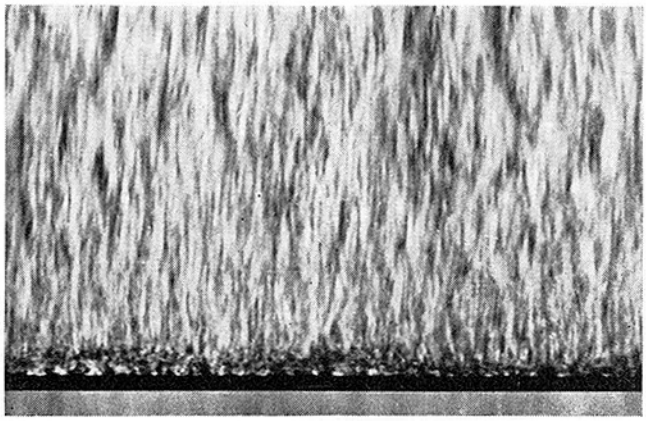

$T_{cy} - T_b = 27$ deg F

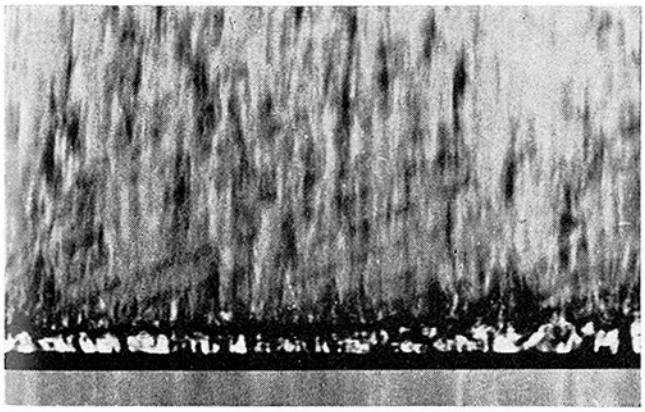

$T_{cy} - T_b = 340$ deg F

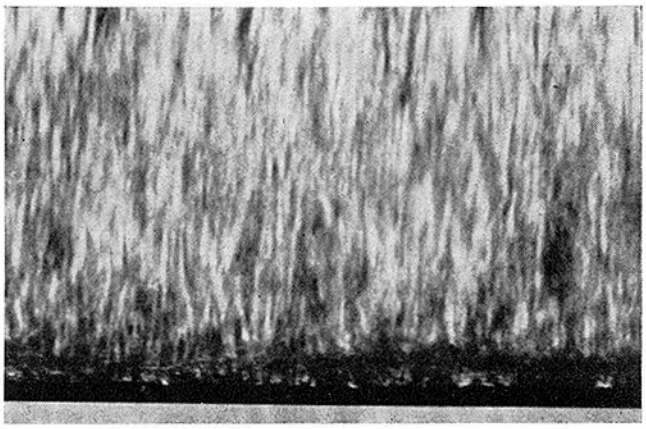

$T_{cy} - T_b = 340$ deg F

Fig. 14 Forced-convection flow field variation with cylinder temperature, Re* = 650; left column, subcritical, $P_b = 1000$ psia; right column, supercritical, $P_b = 1100$ psia

the cylinder and bulk fluid temperature are below the pseudo-critical but that a decrease in heat transfer coefficient occurs when the cylinder is in contact with vapor-like fluid. The amount of decrease in heat transfer coefficient becomes larger as the bulk temperature rises further above the pseudo-critical temperature. Again the results presented are typical of other free-stream velocities and pressures tested.

A large number of still photographs and high-speed movies were studied in an attempt to determine the mechanism of heat transfer. Photos at subcritical pressures show the various expected nucleate, unstable-film, and stable-film boiling regimes. Photos at supercritical pressures show that no secondary or unusual mechanisms of heat transfer are present.

Fig. 12 shows the effect of velocity variation on the flow fields at 1100 psia, 80 deg F, and a cylinder surface temperature of 380 deg F. In free convection the flow field appears as a well-ordered sheet of hot fluid having vertical "columns" of even hotter fluid rising to a turbulent plume. In particular, no unusual bubble-like flow was observed in the immediate vicinity of the cylinder.

With very low free-stream velocities (Re* ~50) the well-ordered free-convection flow breaks up into another regular pattern of horizontal layers of heated fluid. The spacing and structure of these layers resemble a Karman vortex street. Increasing the velocity further breaks up any regular patterns. At the highest velocity in the present tests the flow appeared similar to subcritical film boiling, with a highly disorganized wake

separated from the cylinder by a narrow region of rapidly oscillating fluid.

For purposes of comparison Fig. 13 shows the differences between the free-convection flow field for film and nucleate boiling, and the free-convection flow field at supercritical pressure.

Fig. 14 shows the differences in forced-convection flows at subcritical and supercritical pressures. The subcritical case shows the familiar DNB situation ($T'_{cy} - T'_b = 8$ deg F), and the onset of stable film boiling ($T'_{cy} - T'_b = 27$ deg F), in contrast to the reasonably well-ordered supercritical flow field.

Discussion of Results

Results indicate that, for forced convection from a cylinder in a supercritical fluid, the film coefficient is a strong function of velocity, cylinder, and bulk fluid temperature, and to a lesser extent bulk fluid pressure. Even though sharp peaks in film coefficient have been observed, the heat transfer rate increases smoothly with increasing velocity and temperature difference, not discontinuously as might be expected from some previous free-convection studies, such as Knapp [6] and Nishikawa [8]. It should be emphasized that these results were obtained by a heated cylinder whose temperature was fixed, allowing the heat flux to vary.

In particular, even a slight velocity alters the free-convection flow fields significantly, but the resulting forced-convection flow fields, at all velocities tested, were then similar. These flow fields, or even the free-convection flow fields, did not show the bubble-like flows previously observed [6]. The supercritical forced-convection flow fields consisted of a heated wake separated from the cylinder by a region of rapidly oscillating fluid. Increasing velocity increased the frequency of oscillation and increasing temperature increased the density variations through the wake. No distinct fluid bubbles were observed but the flow did resemble forced-flow subcritical film boiling.

The peaks in heat transfer coefficient correspond to a surface temperature slightly above the pseudo-critical temperature and can be due to the very large values of transport properties occurring in the region next to the heated cylinder. The forced-convection heat transfer process was aided by the oscillating clumps of fluid immediately behind the cylinder. When the bulk fluid is above the pseudo-critical temperature for the test pressure the heat transfer coefficient shows only deterioration with increasing cylinder temperature.

No dimensionless correlations of the data have been presented since, strictly speaking, a correlation which did not include the rates of change with temperature and pressure of all fluid properties, would be valid only for CO_2 and not of general use.

The prime purpose of this work was to investigate the effects of velocity, temperature difference, and bulk temperature and pressure on the mechanisms of heat transfer in near-critical CO_2.

Conclusions

No unusual heat transfer mechanism has been observed for either free or forced convection in the present work. The heat transfer process is aided by vapor-like clumps of fluid which diffuse into the main flow but this is considered only a strong example of variable-property fluid heat transfer. Except for the region of nucleate boiling, heat transfer at supercritical pressures is more effective than heat transfer at subcritical pressures for the same bulk temperature and flow velocity.

Acknowledgments

Financial support of this research by the National Research Council of Canada under Grant A-3330 is gratefully acknowledged.

References

1 Goldman, K., "Special Heat Transfer Phenomena for Supercritical Fluids," NDA 2–31, 1956.

2 Graham, R. W., "Penetration Model Explanation for Turbulent Forced-Convection Heat Transfer Observed in Near-Critical Fluids," NASA TN D-5522, 1969.

3 Petukov, B. S., "Heat Transfer in a Single Phase Medium Under Supercritical Conditions," *Teplofizika Vysokikh Temperatur*, Vol. 6, No. 4, July-Aug. 1968, pp. 732–745.

4 Hendricks, R. C., Simoneau, R. J., Smith, R. V., "Survey of Heat Transfer to Near Critical Fluids," NASA TM X-52612, 1969.

5 Goldstein, R. J., and Aung, W., "Heat Transfer by Free Convection From a Horizontal Wire to Carbon Dioxide in the Critical Region," JOURNAL OF HEAT TRANSFER, TRANS. ASME, Series C, Vol. 90, No. 1, Feb. 1968, pp. 51–55.

6 Knapp, K. K., and Sabersky, R. H., "Free Convection Heat Transfer to Carbon Dioxide Near the Critical Point," *International Journal of Heat and Mass Transfer*, Vol. 9, No. 1, 1966, pp. 41–51.

7 Daniels, T. C., and Bramall, J. W., "An Experimental Investigation of the Heating Mechanism of Carbon Dioxide above the Critical Point," *Proc. Institution of Mechanical Engineers*, Vol. 80, Part 3C, 1965–66.

8 Nishikawa, Kaneyawa, and Miyabe, K., "On the Boiling-Like Phenomena at Supercritical Pressures," *Memoirs of the Faculty of Engineering at Kyusa University*, Vol. 25, No. 1, Dec. 1965, pp. 1–25.

9 Kato, Nishiwaki, and Masaru, H., "Studies on the Heat Transfer of Fluids at a Supercritical Pressure," *Bulletin of JSME*, Vol. 11, No. 46, 1968, pp. 654–663.

10 Skripov, V. P., and Dubrovina, E. N., "Convective Heat Transfer in the Supercritical Region of Carbon Dioxide," *Proceedings of Second All-Soviet Union Conference on Heat and Mass Transfer*, Vol. 1, C. Gazley, Jr., J. P. Hartnett, and E. R. G. Eckert, eds., California University Press, 1966, pp. 36–45.

11 Doughty, D. L., and Drake, R. M., Jr., "Free-Convection Heat Transfer From a Horizontal Right Circular Cylinder to Freon 12 Near the Critical State," TRANS. ASME, Vol. 78, 1956, pp. 1843–1850.

12 Hauptmann, E. G., and Sabersky, R. H., "An Experimental Investigation of Forced Convective Heat Transfer to a Fluid in the Region of its Critical Point," *International Journal of Heat and Mass Transfer*, Vol. 10, 1967, pp. 1499–1508.

V. E. DENNY
Assistant Professor.

A. F. MILLS
Assistant Professor.
Assoc. Mem. ASME

V. J. JUSIONIS
Research Assistant.

University of California,
Los Angeles, Calif.

Laminar Film Condensation From a Steam-Air Mixture Undergoing Forced Flow Down a Vertical Surface

An analytical study of the effects of noncondensable gas on laminar film condensation of vapor undergoing forced flow along a vertical surface is presented. Due to the markedly nonsimilar character of the coupled two-phase-flow problem, the set of parabolic equations governing conservation of momentum, species, and energy in the vapor phase was solved by means of finite-difference methods using a forward marching technique. Interfacial boundary conditions for the numerical solution were extracted from a locally valid Nusselt-type analysis of the liquid-film behavior. Locally variable properties in the liquid were treated by means of the reference-temperature concept, while those in the vapor were treated exactly. Closure of the numerical solution at each step was effected by satisfying overall mass and energy balances on the liquid film. A general computer program for solving the problem has been developed and is applied here to condensation from water-vapor–air mixtures. Heat-transfer results, in the form q/q_{Nu} versus x, are reported for vapor velocities in the range 0.1 to 10.0 fps *with the mass fraction of air ranging from 0.001 to 0.1. The temperature in the free stream is in the range 100–212 deg F, with overall temperature differences ranging from 5 to 40 deg F. The influence of noncondensable gas is most marked for low vapor velocities and large gas concentrations. The nonsimilar character of the problem is especially evident near $x = 0$, where the convective behavior of the vapor boundary layer is highly position-dependent.*

Introduction

THE PRESENCE of a small concentration of noncondensable gas in a vapor leads to significant reductions in condensation heat-transfer rates. Previous analytical attention has been directed to the specific problem of gravity-flow laminar-film condensation on a vertical surface, where the only motion in the vapor is caused by the condensation process itself. A vapor boundary-layer flow arises from natural convection induced by the species concentration and temperature-dependent density variation adjacent to the film, and from vapor drag by the liquid surface. The gravity-flow problem admits a similarity solution to the coupled set of boundary-layer conservation equations governing the two-phase flow. By integrating the resulting ordinary differential equations numerically, Sparrow and Lin [1][1] analyzed the constant-property (Boussinesq approximation) problem while Minkowycz and Sparrow [2, 3] extended the study to include variable properties for the water-vapor–air system. In addition, Rose [4] has employed an integral method to obtain an approximate solution to the constant-property problem. Several experiments have been performed to determine the effect of noncondensable gas on condensation rates. The water-vapor–air system has received most attention owing to its importance in relation to steam power plant condenser performance and distillation-type saline-water conversion processes. In most of these experiments, e.g., Hampson [5] and Meisenburg et al. [6], significant forced convection was present in the vapor. Indeed, in order to insure minimal forced-flow effects, Minkowycz and Sparrow had to resort to a comparison with experimental data for condensation on a horizontal tube obtained by Othmer [7]. More recently Slegers [8] has performed an experimental investigation specifically intended to evaluate the results of the Minkowycz analysis. The measured condensation rates were, on an average, 20 percent above the analytical predictions. Even though care was taken to minimize spurious convective motions, Slegers attributes this discrepancy to a failure to completely eliminate forced convection. The available experimental evidence thus appears to indicate that reductions in condensation rates due to noncondensable gas are sensitive to the presence of forced flow in the vapor phase. As most industrial situations are

[1] Numbers in brackets designate References at end of paper.

Contributed by the Heat Transfer Division for publication (without presentation) in the JOURNAL OF HEAT TRANSFER. Manuscript received by the Heat Transfer Division August 20, 1970. Paper No. 71-HT-E.

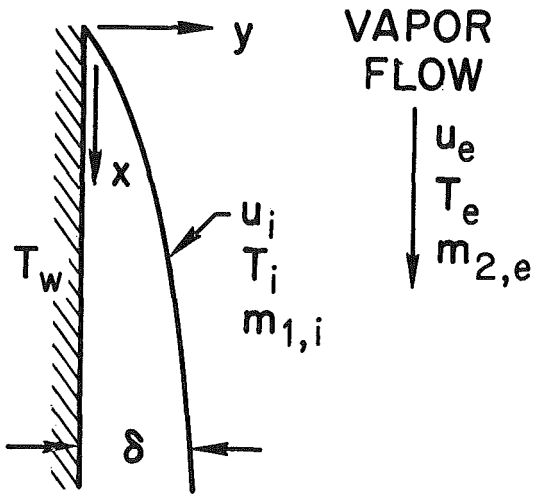

Fig. 1 Coordinate system and related physical quantities

characterized by forced-convection vapor flows, an analysis of the forced-vapor-flow situation is warranted.

The problem of laminar film condensation on a vertical surface, with forced vapor flow parallel to the surface, is nonsimilar in character. An exact analytical result requires solution of a coupled set of boundary-layer conservation equations which cannot be reduced to a set of ordinary differential equations. A previous result of the present authors [9] does enable one significant simplification of the solution procedure. They have shown that the behavior of the liquid film may be satisfactorily analyzed using the Nusselt assumptions, whereby liquid acceleration and energy convection are neglected, provided locally variable properties are evaluated at an appropriate reference temperature. For example, a reference temperature $T_r = T_w + 0.33(T_i + T_w)$ has been established for water which is independent of temperature level, wall-temperature variation, and vapor drag due to forced flow. Thus, the set of parabolic partial differential equations governing conservation of momentum, species, and energy in the vapor phase can be solved by finite-difference methods using a forward marching technique, extracting the necessary boundary conditions at the interface from a locally applied Nusselt-type analysis.

Analysis and Numerical Procedure

Physical Model and Coordinates. A schematic representation of the physical model and coordinate system is shown in Fig. 1. The coordinates along and normal to the surface are x and y respectively, and the corresponding velocity components are u and v. At some distance from the surface the vapor has velocity u_e, temperature T_e, and noncondensable-gas concentration $m_{2,e}$. The system pressure, P_e, is determined from T_e and $m_{2,e}$, the free-stream vapor being saturated. The condenser wall is at a uniform temperature T_w. The condensate film has thickness δ, which is a function of x. At the liquid–vapor interface the temperature T_i, and consequently the vapor concentration $m_{1,i}$ are unknown and are determined in the course of analysis.

Conservation Equations and Boundary Conditions. For the vapor phase the equations governing conservation of mass, momentum, species, and energy are, respectively:

$$\frac{\partial}{\partial x}(\rho_v u) + \frac{\partial}{\partial y}(\rho_v v) = 0 \tag{1}$$

$$\rho_v u \frac{\partial u}{\partial x} + \rho_v v \frac{\partial u}{\partial y} = \frac{\partial}{\partial y}\left(\mu_v \frac{\partial u}{\partial y}\right) + g(\rho_v - \rho_{v,e}) \tag{2}$$

$$\rho_v u \frac{\partial m_1}{\partial x} + \rho_v v \frac{\partial m_1}{\partial y} = \frac{\partial}{\partial y}\left(\rho_v \mathfrak{D}_{12} \frac{\partial m_1}{\partial y}\right) \tag{3}$$

$$\rho_v u \frac{\partial T}{\partial x} + \rho_v v \frac{\partial T}{\partial y} = \frac{\partial}{\partial y}\left(\frac{k_v}{C_{pv}} \frac{\partial T}{\partial y}\right) + \frac{k_v}{C_{pv}} \frac{\partial T}{\partial y} \frac{\partial \ln C_{pv}}{\partial y} + \frac{\rho_v \mathfrak{D}_{12}}{C_{pv}} (C_{p1} - C_{p2}) \frac{\partial m_1}{\partial y} \frac{\partial T}{\partial y} \tag{4}$$

Viscous dissipation and compressibility effects are omitted from the energy equation since low-velocity flow is under consideration. In addition, thermal diffusion and diffusional conduction (Dufour effect) are ignored in view of the results obtained by Minkowycz [2]. For the liquid phase, constant properties are assumed and the Nusselt assumptions invoked to yield equations governing conservation of momentum and energy respectively as

$$0 = \mu_l \frac{d^2 u}{dy^2} + g(\rho_l - \rho_{v,e}) \tag{5}$$

$$0 = \frac{d^2 T}{dy^2} \tag{6}$$

Equations (1)–(6) are subject to the boundary conditions:
Vapor at infinity: $y \to \infty$;

$$u \to u_e, \quad m_1 \to m_{1,e}, \quad T \to T_e \tag{7}$$

Liquid at the wall: $y = 0$;

$$u = 0, \quad T = T_w \tag{8}$$

Nomenclature

$\mathfrak{G}$ = mass-transfer driving force
C_p = heat capacity (Btu/lb deg R)
$\mathfrak{D}_{12}$ = binary diffusion coefficient (ft²/sec)
g = normal gravity (ft/sec²), also conductance (lb/ft² sec)
k = thermal conductivity (Btu/ft sec deg R)
m = mass fraction
$\dot{m}$ = condensation rate (lb/ft² sec)
n = mass flux (lb/ft² sec)
Nu_m = Nusselt number for mass transfer, $gx/\rho\mathfrak{D}_{12}$
P = pressure (atm)
q = wall heat flux (Btu/ft² sec)
q_{Nu} = Nusselt heat flux (Btu/ft² sec)
R = specific gas constant (atm ft³/lb deg R)
Re = Reynolds number, $u_e\rho_e x/\mu_e$
Sc = Schmidt number, $\mu_e/\rho_e\mathfrak{D}_{12}$
T = absolute temperature (deg R)
u, v = velocity components (fps)
x, y = boundary-layer coordinates (ft)
δ = condensate film thickness (ft)
δ_v = vapor boundary-layer thickness (ft)
λ = latent heat of vaporization (Btu/lb)
μ = absolute viscosity (lb/ft sec)
ν = kinematic viscosity (ft²/sec)
ρ = density (lb/ft³)
τ = shear stress (lb/ft sec²)
ψ = stream function (lb/ft sec)
$\omega = (\psi - \psi_i)/(\psi_e - \psi_i)$
$\nabla_j = \omega_j - \omega_{j-1}$

Subscripts

e = at the vapor boundary-layer edge
i = at the interface
j = jth node point
l = in the liquid phase
r = at the reference state
v = in the vapor phase
w = at the wall
1 = of water vapor
2 = of air

Superscripts

* = at the previous step

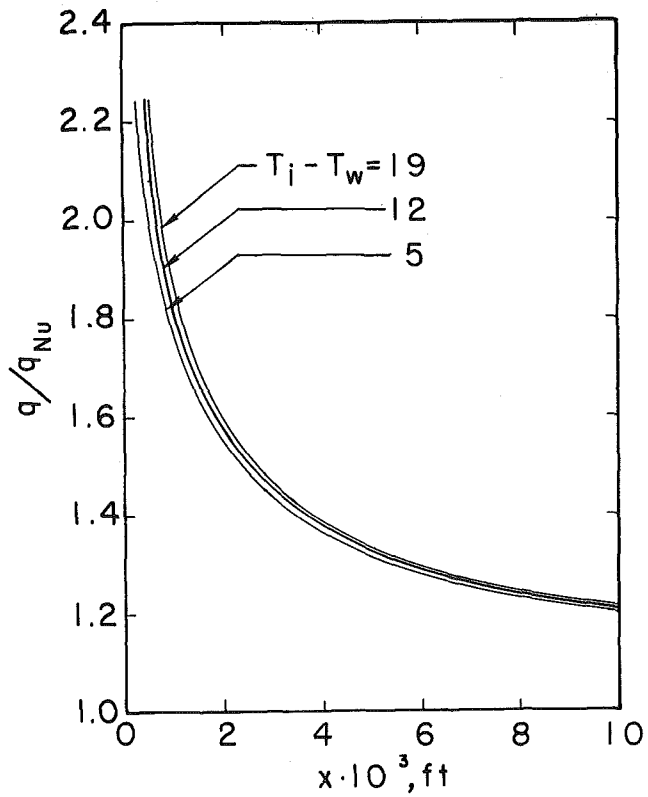

Fig. 2 Effect of initial conditions on the starting problem: u_e = 10 fps, $m_{2,e}$ = 0.01, T_e = 212 deg F, $T_e - T_w$ = 20 deg F

Interface continuity: $y = \delta$;

$$u|_{l,i} = u|_{v,i} = u_i \tag{9}$$

$$T|_{l,i} = T|_{v,i} = T_i \tag{10}$$

$$\mu_l \left.\frac{\partial u}{\partial y}\right|_i = \mu_v \left.\frac{\partial u}{\partial y}\right|_i = \tau_i \tag{11}$$

$$\frac{d}{dx}\int_0^\delta \rho_l u dy = -\dot{m} = \frac{\rho_v \mathfrak{D}_{12}}{1 - m_1} \left.\frac{\partial m_1}{\partial y}\right|_i \tag{12}$$

$$k_l \left.\frac{\partial T}{\partial y}\right|_i = -\dot{m}\lambda + k_v \left.\frac{\partial T}{\partial y}\right|_i \tag{13}$$

In addition, there is the equation of state of an ideal gas mixture, $P = \rho_v RT$, and the thermodynamic constraint that the interface condition is a saturation state for the condensing vapor. From thermodynamic tables,

$$T_i = T_i(m_{1,i}, P) \tag{14}$$

where it is assumed that the interface exhibits negligible departure from thermodynamic equilibrium, in accordance with results presented in references [2, 10].

Closure of the problem is attained through a heat balance on the liquid film which determines its thickness δ, namely,

$$\int_0^x k_l \left.\frac{\partial T}{\partial y}\right|_{y=0} dx = \int_0^\delta \rho_l u[\lambda + C_{pl}(T_i - T)]dy|_x + \int_0^x k_v \left.\frac{\partial T}{\partial y}\right|_i dx \tag{15}$$

With the problem stated in the above form, the analytical task may be viewed as one of solving the partial differential equations (1)–(4) governing conservation in the vapor phase, subject to a complex set of boundary conditions. These conditions include a subsidiary solution of the ordinary differential equations governing conservation in the liquid phase. A finite-difference analog to the partial differential equations was developed following the procedure recommended by Patankar and Spalding [11]. For this purpose it was required to effect a transformation of independent variables x, y to x, ω where ω is a nondimensional stream function defined by $\omega \equiv (\psi - \psi_i)/(\psi_e - \psi_i)$. Space limitations preclude a complete reformulation of the problem in terms of the new variables. It suffices to note that equations (2)–(4) transform into the general form

$$\frac{\partial f_n}{\partial x} - F(\psi)\frac{\partial f_n}{\partial \omega} = \frac{\partial}{\partial \omega}\left(\phi_n \frac{\partial f_n}{\partial \omega}\right) + \Phi_n \tag{16}$$

where $F(\psi) = (d\psi_i/dx + \omega d(\psi_e - \psi_i)/dx)/\Delta\psi = (-\dot{m} + \omega d\Delta\psi/dx)/\Delta\psi$, and for n = 1, 2, and 3 the quantities f_n, ϕ_n, and Φ_n are defined as follows:

n	f_n	$(\Delta\psi)^2\phi_n/\rho_v\mu_v u$	$\rho_v u\Phi_n$
1	u	1	$g(\rho_v - \rho_{v,e})$
2	m_1	$\rho_v\mathfrak{D}_{12}/\mu_v$	0
3	T	$k_v/C_{pv}\mu_v$	$\left(k_v \frac{\partial T}{\partial y}\frac{\partial \ln C_{pv}}{\partial y} + \rho_v\mathfrak{D}_{12}(C_{p1} - C_{p2})\frac{\partial m_1}{\partial y}\frac{\partial T}{\partial y}\right)\Big/ C_{pv}$

Difference Equations. For the vapor-side problem, equations (16) were approximated by fully implicit finite-difference equations of the form

$$\frac{f_{n,j} - f^*_{n,j}}{\Delta x} - \frac{F_j}{\nabla_j + \nabla_{j+1}}\left(\frac{\nabla_j}{\nabla_{j+1}}(f_{n,j+1} - f_{n,j}) + \frac{\nabla_{j+1}}{\nabla_j}(f_{n,j} - f_{n,j-1})\right) \simeq \frac{2}{\nabla_j + \nabla_{j+1}}\left(\phi_{n,j+\frac{1}{2}}\frac{f_{n,j+1} - f_{n,j}}{\nabla_{j+1}} - \phi_{n,j-\frac{1}{2}}\frac{f_{n,j} - f_{n,j-1}}{\nabla_j}\right) + \Phi_{n,j} \tag{17}$$

where $f_{n,j} = f_n(x, \omega_j)$, $f^*_{n,j} = f_n(x - \Delta x, \omega_j)$, and $\nabla_j = \omega_j - \omega_{j-1}$. The mesh points ω_j were spaced such that forward difference approximations for extracting velocity, temperature, and mass species gradients at the interface

$$\left.\frac{\partial f_n}{\partial y}\right|_{\omega=0} = \left.\frac{\partial f_n}{\partial y}\right|_i \simeq \frac{f_{n,2} - f_{n,1}}{y_2} - \frac{y_2}{y_3}\left(\frac{f_{n,3} - f_{n,2}}{y_3 - y_2} - \frac{f_{n,2} - f_{n,1}}{y_2}\right) \tag{18}$$

where

$$y_j = y_{j-1} + 2\nabla_j\Delta\psi/(\rho_{v,j}u_j + \rho_{v,j-1}u_{j-1}) \tag{19}$$

$$d\psi_e/dx = \mu_{v,e}/(y_{je} - y_{je-1}) \tag{20}$$

$$\Delta\psi = \Delta\psi^* + (\Delta x/2)(d\psi_e/dx + (d\psi_e/dx)^* + \dot{m} + \dot{m}^*) \tag{21}$$

are as accurate as the difference equations (17). Thus, equations (17) assume the general algebraic form

$$f_{n,j} = A_{n,j}f_{n,j+1} + B_{n,j}f_{n,j-1} + C_{n,j} \tag{22}$$

where n = 1, 2, 3 and j = 2, 3, . . . , $je - 1$, with Dirichlet boundary conditions at $\omega = 1$

$$f_{n,je} = f_{n,e} \tag{23}$$

and mixed boundary conditions at $\omega = 0$

$$f_{n,1} = f_n|_i \qquad (n = 1, 3) \tag{24}$$

$$\partial m_1/\partial y|_i = -\dot{m}(1 - m_1)/\rho_v\mathfrak{D}_{12}|_i \qquad (n = 2) \tag{25}$$

On introducing equation (18) for n = 2, the interfacial species boundary condition assumes the form

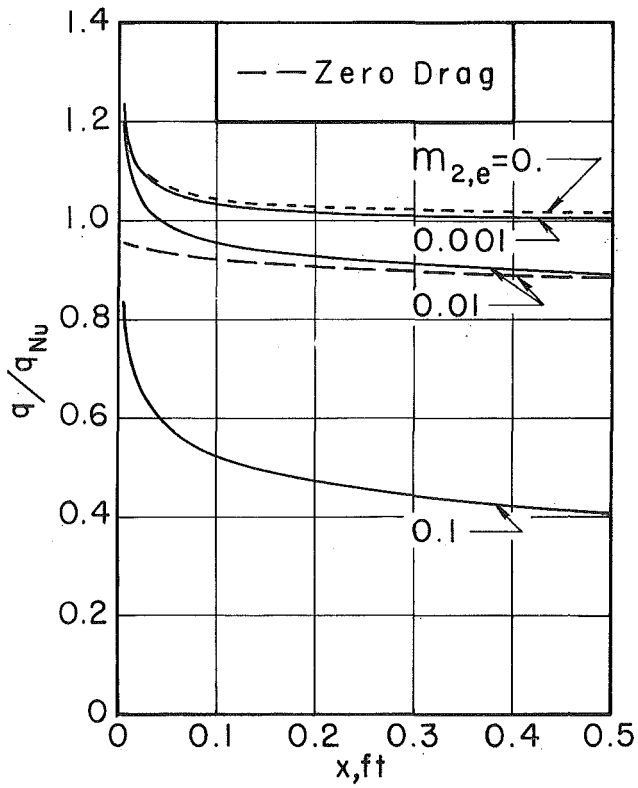

Fig. 3 Condensation heat transfer: u_e = 10 fps, T_e = 212 deg F, $T_e - T_w$ = 5 deg F

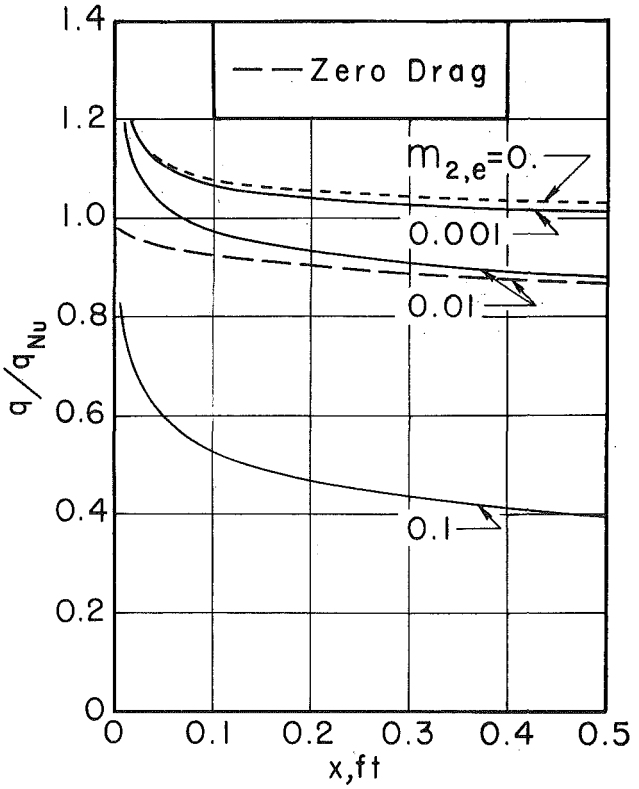

Fig. 4 Condensation heat transfer: u_e = 10 fps, T_e = 212 deg F, $T_e - T_w$ = 20 deg F

$$m_{1,1} = \alpha m_{1,2} + \beta m_{1,3} + \gamma$$

which is used to eliminate $m_{1,1}$ from the set (22) when $j = 2$.

Numerical Procedure. Once initial conditions for the problem had been established (see discussion below), the numerical solution was advanced step by step as follows:

1 Interfacial shear τ_i, temperature T_i, and vapor-side conductive heat flux $k_v \partial T/\partial y|_i$ were set equal to upstream values.

2 The vapor-side dependent variables $f_{n,j}$, y_j, $d\psi_i/dx$, and $\Delta\psi$ were assigned their upstream values.

3 The nonlinear coefficients $A_{n,j}$, $B_{n,j}$, $C_{n,j}$, α, β, and γ were computed.

4 The thickness of the liquid film δ and, hence, the interfacial velocity u_i and mass condensation rate $\dot{m} = -d\psi_i/dx$ were extracted from a local solution of equations (5), (6), (8), (10), (11), and (15); equation (5); and equation (13), respectively.

5 The vapor-side problem, equations (22)–(25), was solved, and improved values of T_i, τ_i, and $k_v dT/dy|_i$ were calculated using equations (14) and (18).

6 Steps 4 and 5 were then repeated until successive iterates on $m_{1,i}$ were unchanging in the sixth significant digit.

7 Improved values of y_j, $d\psi_e/dx$, and $\Delta\psi$ were calculated, equations (19)–(21), and steps 3 through 6 repeated until the nonlinear coefficients $A_{n,j}$ through γ had negligible effect on $m_{1,i}$.

Technically speaking, iteration at each x-step is not required. However, it was found that excessively small marching steps Δx were required to yield sufficiently accurate, and in some instances stable, solutions when iteration was not employed. Thus it proved to be more efficient to solve a totally implicit problem. In so doing, it was imperative that nonlinear feedback effects be absent during closure of the "inner" problem (steps 4 and 5). Thus, step 7 was not executed until a reasonably accurate solution to the linearized inner problem had been effected.

Initial conditions for starting the solution were obtained as follows. First, the interfacial temperature T_i was arbitrarily assigned (usually $T_i \to T_e$). Then, the liquid-film problem was solved neglecting vapor-side heat conduction and approximating vapor drag by the asymptotic result $\tau_i = -\dot{m}u_e$ [9]. Finally, vapor boundary-layer profiles were extracted from a Couette-type analysis.

Recognizing the inherent difficulty in applying forward marching techniques to nonsimilar boundary-layer problems, the authors conducted numerous numerical experiments to ascertain the effect of various parameters of the numerical method. It was found that reliable solutions were obtained when the initial conditions were established in the interval $10^{-6} \leq x \leq 10^{-4}$ ft, marching-step size did not exceed one-half a vapor boundary-layer thickness (defined as the distance y from the interface at which $u = 0.999u_e$), and not less than 100 node points were distributed across the vapor boundary layer. The latter distribution was effected by positioning a majority of the node points in the first third of the boundary layer, the distance between the outermost pair of node points being set initially to about 5 percent of the boundary-layer thickness; the 5 percent figure was arrived at empirically and proved to give satisfactory results for the mass entrainment rate, equation (20).

The exceedingly small value of x at the starting station was dictated by uncertainties in the initially assigned interfacial temperature T_i. It was found that for $10^{-6} \leq x \leq 10^{-4}$ any arbitrariness in the initial conditions (as dictated by the choice of T_i and interfacial shear) had negligible effect on the numerical solution for $x \geq 0.01$ ft. This is illustrated for a typical case in Fig. 2, where values of $(T_i - T_w)/(T_e - T_w)$ of 0.25, 0.60, and 0.95 are seen to give virtually identical results after $x = 0.01$.

The numerical problem was coded in Fortran IV and the resulting program run on an IBM 360/91 digital computer. (Actually, two programs were developed independently by the authors. This was done to gain confidence in the results, since very little prior work had been done on the problem.) Within the constraints cited above, the maximum error in the results is less than

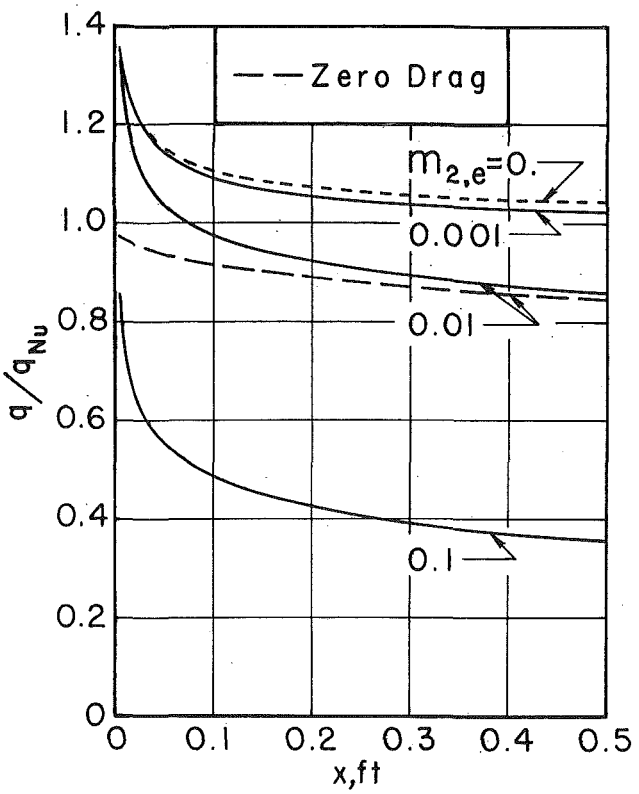

Fig. 5 Condensation heat transfer: u_e = 10 fps, T_e = 212 deg F, $T_e - T_w$ = 40 deg F

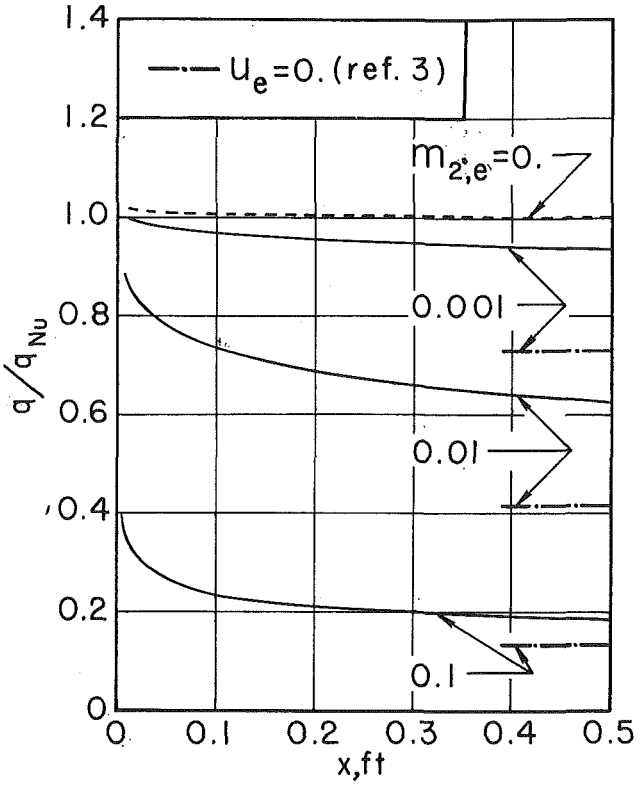

Fig. 6 Condensation heat transfer: u_e = 1 fps, T_e = 212 deg F, $T_e - T_w$ = 5 deg F

2 percent. Computational times for 6 in. of plate ranged from 30 sec for the easier cases (negligible air in the free stream) to about 20 min for the difficult cases ($m_{2,e}$ = 0.1, u_e = 0.1). We subsequently have reduced, by means of Steffenson's method, the computational time for the latter cases to about 2 min.

Thermophysical Properties. The properties ρ_l, C_{pl}, k_l, and μ_l were extracted from sources listed in [9] and evaluated by means of least-squares analysis at the reference temperature T_r. For the steam–air mixture, procedures recommended by Minkowycz [2] were followed. Briefly, mixture rules set forth by Mason and Monchik [12] were employed to evaluate, first, $\mathfrak{D}_{12}$, and then μ and k, assuming a Lennard-Jones interaction potential and using kinetic-theory parameters compiled in [13]. Pure species values for μ and k were taken from [14]. For air and steam C_p was taken, respectively, from [14] and [15]. The latent heat of vaporization, vapor pressure at saturation, and steam density were algebraically fitted according to values in [15]. Values of ρ and C_p were calculated by means of standard additive procedures, assuming air to be an ideal gas for the former.

Results and Discussion

Numerical solutions of condensation heat transfer from water-vapor–air mixtures undergoing forced flow along a vertical surface are presented, in the form q/q_{Nu} versus x, in Figs. 3–11. (Here, q_{Nu} is the classical Nusselt result based on overall temperature drop $T_e - T_w$, assuming zero drag and evaluating variable physical properties at the reference temperature $T_r = T_w + 0.33\ (T_e - T_w)$.) Pertinent parameters studied include T_e (212, 150, 100 deg F), $T_e - T_w$(5, 20, 40 deg F), u_e(0.1, 1.0, 10.0 fps), and $m_{2,e}$(0.0, 0.001, 0.01, 0.1). Evolution of typical dependent-variable profiles for the vapor phase in the near-free-convection limit is illustrated in Figs. 12(a), 12(b), and 12(c).

Major trends in the results can be explained by isolating the effect of the problem parameters on, first, the behavior of the liquid film and, second, that of the vapor boundary layer. For given $m_{2,e}$, the behavior of the liquid film is directly affected by the individual effects of u_e, $T_e - T_w$, and T_e on vapor drag and liquid viscosity. For $m_{2,e}$ = 0, these effects are effectively isolated from other considerations. Thus, for u_e = 0.1 fps, q/q_{Nu} = 1.0 and vapor drag is seen to be negligible, Figs. 9 and 10. However, at u_e = 1.0 fps, vapor drag tends to increase q/q_{Nu} as $T_e - T_w$ increases from 5 to 40 deg F, particularly near x = 0, Figs. 6–8. Finally, for u_e = 10.0 fps, vapor drag is appreciable for significant distances x, especially at elevated values of $T_e - T_w$; furthermore, the effect remains appreciable when air is present, Figs. 3–5. From these observations, it is seen that the effects of interfacial velocity and induced natural convection may be ignored as u_e becomes large, the magnitude of the vapor drag being essentially equal to the asymptotic value $\dot{m}u_e$ which is characteristic of boundary-layer flows undergoing strong suction. Since $\dot{m}\alpha[(T_e - T_w)/x]^{1/4}$ in such cases, interpretation of the trends noted above in terms of asymptotic drag is straightforward. In addition, we observe that: (a) the strong influence of drag near x = 0 is due not only to increased $\dot{m}$ but also to the added drag (above that predicted by the asymptotic result) with an $x^{-1/2}$ dependence for a zero-pressure-gradient flow, (b) the less-pronounced effect of drag at lower values of T_e ($m_{2,e}$ = 0.001 curves in Fig. 11) is primarily due to increased liquid viscosity, but near x = 0 there also is a reduction in the excess drag over the asymptotic value due to the lowered vapor density, (c) the magnitude of the vapor-drag effect exhibited by the $m_{2,e}$ = 0 curves is less pronounced with increasing $m_{2,e}$ since $(T_i - T_e) < (T_e - T_w)$.

The effects of u_e, $T_e - T_w$, and T_e on q/q_{Nu}, as determined by the behavior of the vapor-phase boundary layer, are directly related to the mechanism by which noncondensable gas accumulates at the liquid-film surface. This accumulation reflects a balance between the convective inflow as induced by the condensation process itself and the diffusive outflow established by the resulting favorable concentration gradient. In mathematical terms, this is merely a statement of the interface boundary con-

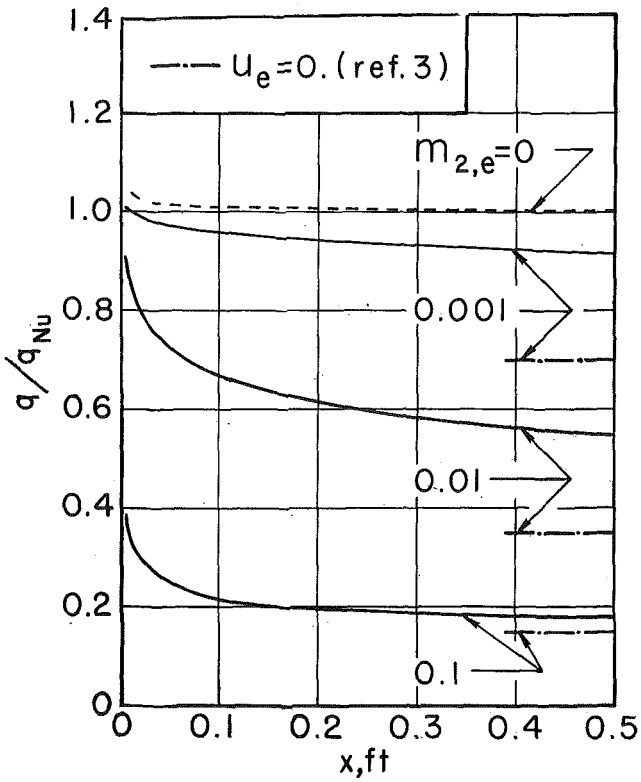

Fig. 7 Condensation heat transfer: u_e = 1 fps, T_e = 212 deg F, $T_e - T_w$ = 20 deg F

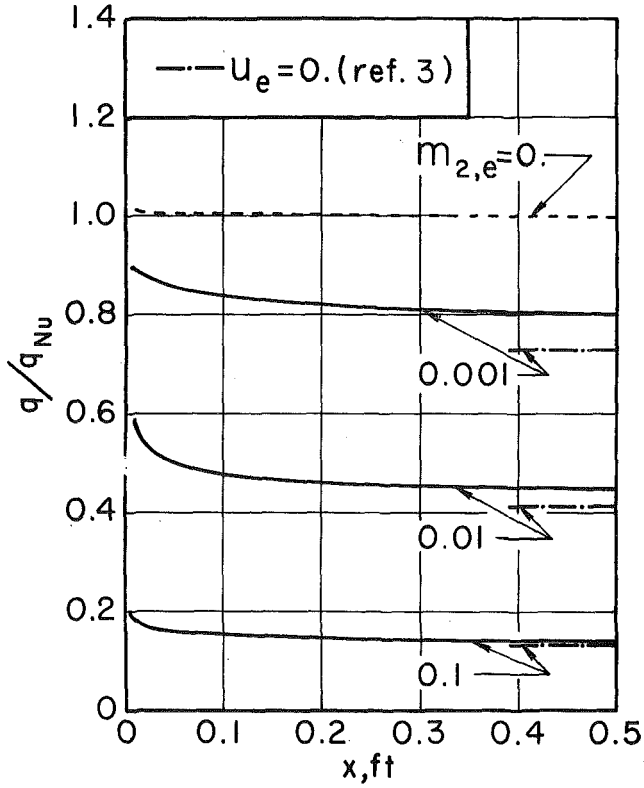

Fig. 9 Condensation heat transfer: u_e = 0.1 fps, T_e = 212 deg F, $T_e - T_w$ = 5 deg F

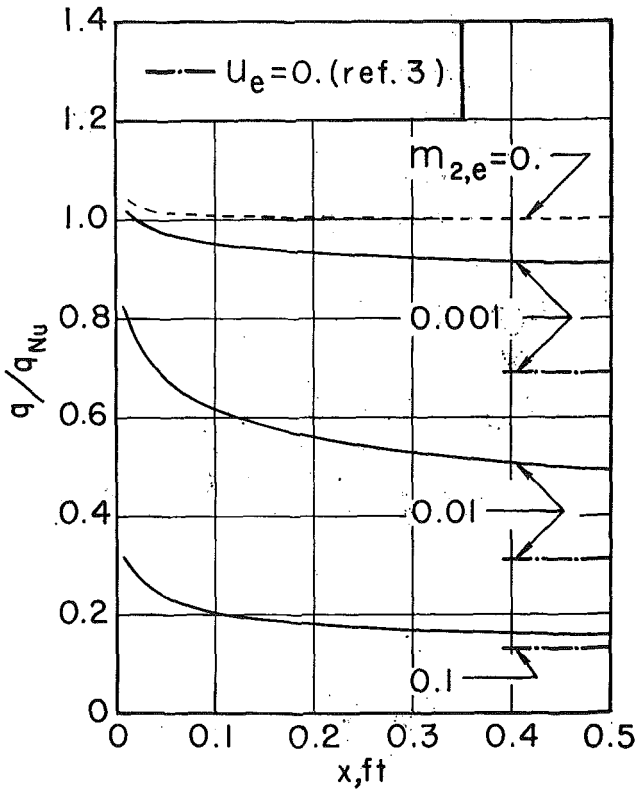

Fig. 8 Condensation heat transfer: u_e = 1 fps, T_e = 212 deg F, $T_e - T_w$ = 40 deg F

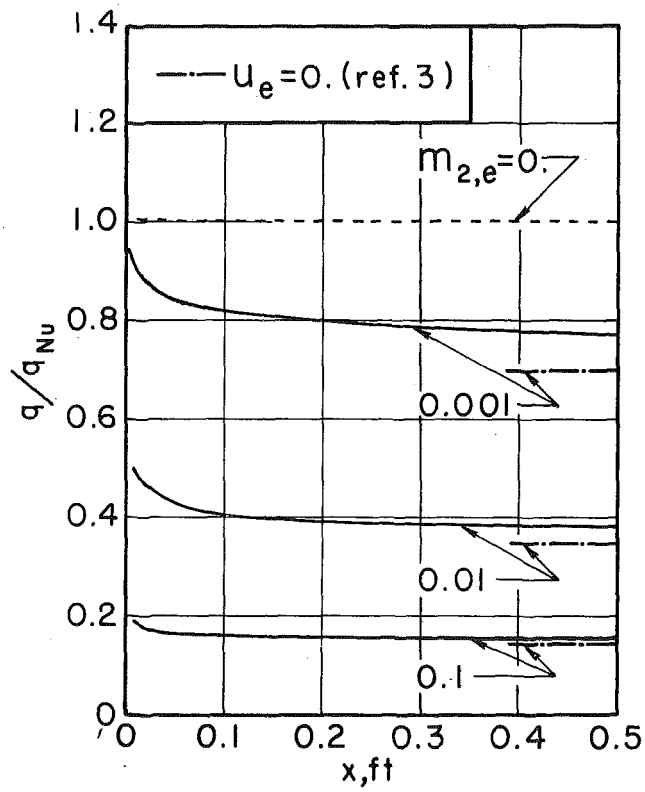

Fig. 10 Condensation heat transfer: u_e = 0.1 fps, T_e = 212 deg F, $T_e - T_w$ = 20 deg F

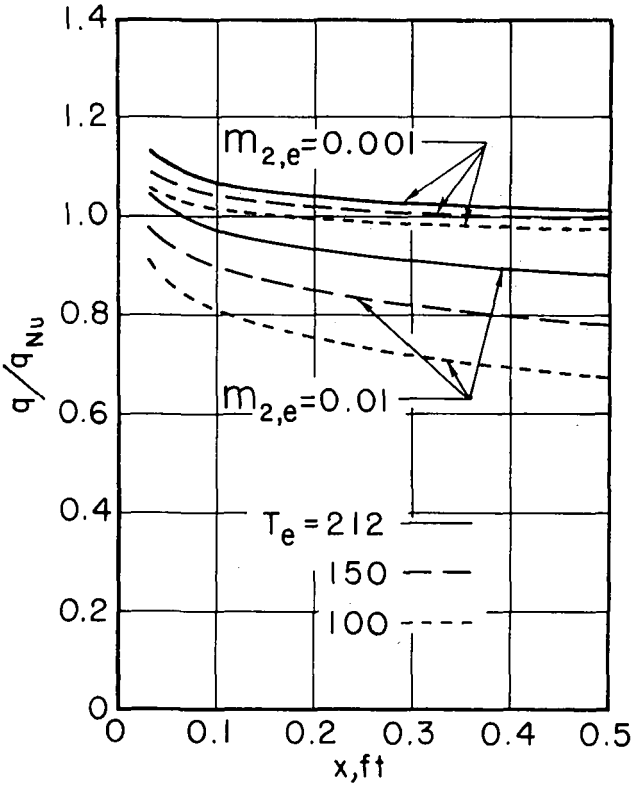

Fig. 11 Condensation heat transfer: $u_e = 10$ fps

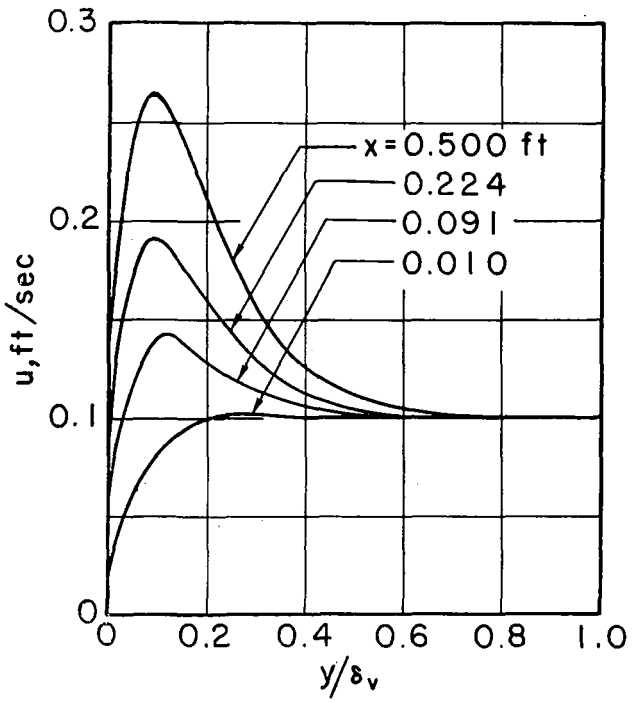

Fig. 12(a) Typical vapor-phase velocity profile: $u_e = 0.1$ fps, $m_{2,e} = 0.01$, $T_e = 212$ deg F, $T_e - T_w = 5$ deg F

dition on the species conservation equation for the gas, namely

$$n_{2,i} = \dot{m} m_{2,i} - \rho \mathfrak{D}_{12} \left. \frac{\partial m_2}{\partial y} \right|_i = 0$$

which is equivalent to equation (25). Introducing a dimensionless concentration $\phi = m_1/(m_{1,e} - m_{1,i})$ into equation (25), there is obtained

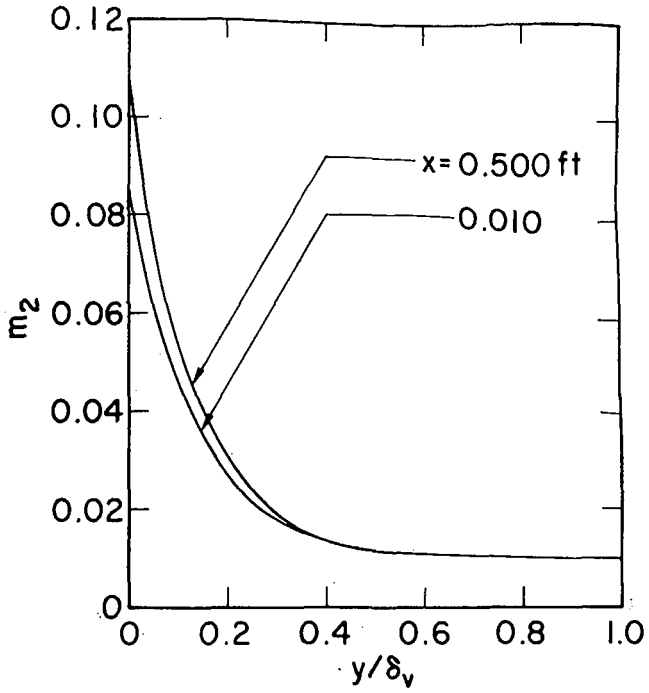

Fig. 12(b) Typical vapor-phase mass-concentration air profile: $u_e = 0.1$ fps, $m_{2,e} = 0.01$, $T_e = 212$ deg F, $T_e - T_w = 5$ deg F

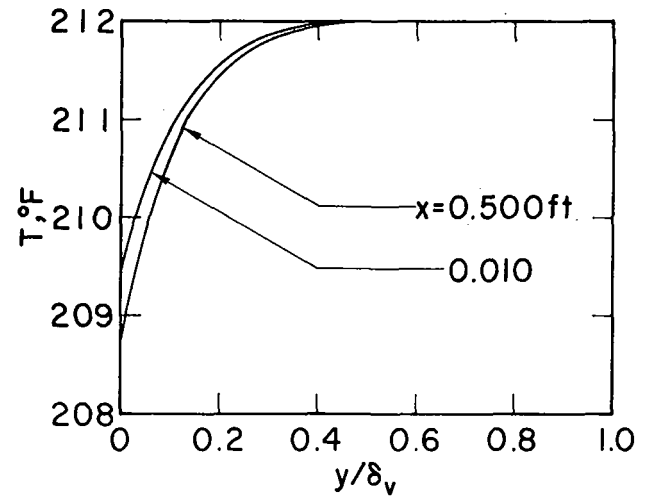

Fig. 12(c) Typical vapor-phase temperature profile: $u_e = 0.1$ fps, $m_{2,e} = 0.01$, $T_e = 212$ deg F, $T_e - T_w = 5$ deg F

$$\dot{m} = \frac{m_{1,e} - m_{1,i}}{m_{1,i} - 1} \rho \mathfrak{D}_{12} \left. \frac{\partial \phi}{\partial y} \right|_i = \mathfrak{B} g$$

where $\mathfrak{B} = (m_{1,e} - m_{1,i})/(m_{1,i} - 1)$ is the mass-transfer driving force and $g = (\rho \mathfrak{D}_{12} \partial \phi / \partial y)_i$ is the conductance as defined by Spalding [16]. Since $\dot{m} \to -\infty$ as $\mathfrak{B} \to -1$ ($m_{1,e} \to 1$), the noncondensable-gas problem involves highly nonlinear coupling between the factors $\mathfrak{B}$ and g. Nonetheless, a qualitative appreciation for the observed effects of u_e, $T_e - T_w$, and T_e may be had by examining, in turn, their influence on g.

The conductance g is primarily a function of the velocity field (u,v), its dependence on the mixture property $\rho \mathfrak{D}_{12}$ (weakly temperature-dependent) being second-order. The dynamics of the vapor boundary-layer flow are determined by two main considerations—strong suction toward the interface and variable convective flow along the interface. Of importance in the latter

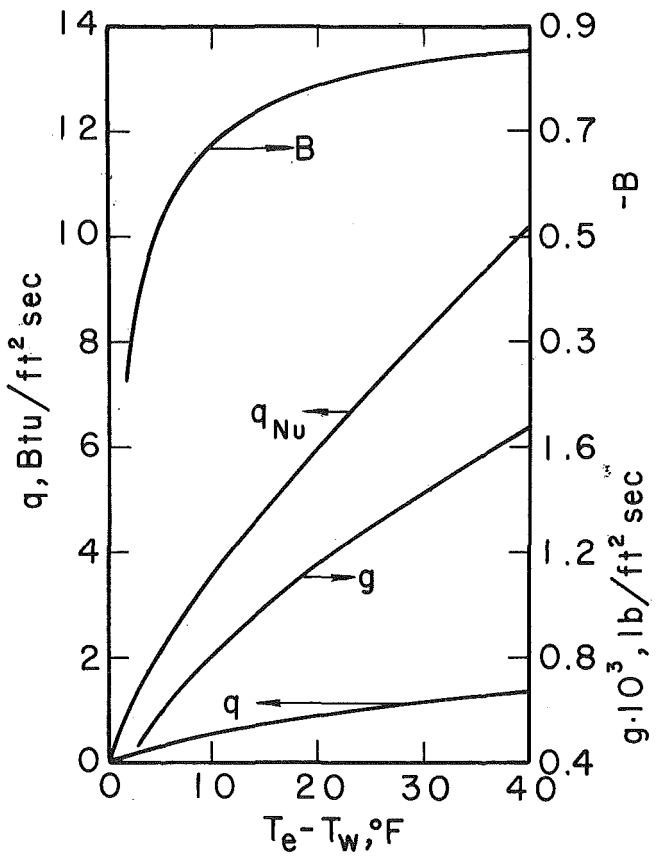

Fig. 13 Effect of $T_e - T_w$ on condensation heat transfer as drawn from data in reference [3]: $u_e = 0$, $m_{2,e} = 0.1$, $T_e = 212$ deg F

context are the relative magnitude of u_e and u_i as well as natural convection, induced by the variation of mixture density across the boundary layer. When $u_e \gg u_i$, a qualitative appreciation for the dependence of g on the flow field may be had by examining the Nusselt number for mass transfer on a flat plate in the $\dot{m} \to 0$ limit, namely,

$$\mathrm{Nu}_m = \frac{gx}{\rho \mathfrak{D}_{12}} \simeq \text{const } \mathrm{Re}^{1/2}\,\mathrm{Sc}^{1/3}$$

whence it is seen that

$$g \alpha u_e^{1/2} \rho_e^{1/2} x^{-1/2}$$

Using the above results, interpretation of the major trends exhibited by the figures is straightforward. Thus, for given T_e, $T_e - T_w$, and $m_{2,e}$ the ratio q/q_{Nu} is seen to increase with increasing u_e and to decrease with increasing x, Figs. 3, 6, 9; 4, 7, 10; and 5, 8. However, at reduced values of u_e, the effects are less pronounced, particularly at high gas concentrations, owing to the change in the convective character of the boundary layer away from forced flow. This is particularly evident in Figs. 9 and 10, where it is seen that at $u_e = 0.1$ fps and higher values of $m_{2,e}$ the results closely approach the $u_e = 0$ similar solution reported by Minkowycz and Sparrow [3]. The effects of temperature level T_e, Fig. 11, are seen to be due to the $\rho_e^{1/2}$-dependence of g, the vapor density decreasing sharply with T_e.

The effects of increased temperature drop $T_e - T_w$ (reduced wall temperature T_w) on q/q_{Nu} are best explained in terms of the increased values in the magnitude of $\mathcal{B}$ which must accompany an increase in condensation rate. However, at the lower gas concentrations (0.01, 0.001) appreciable increases in $|\mathcal{B}|$ require substantial decreases in $m_{1,i}$ since $\mathcal{B}$ already is near its asymptotic limit $-m_{1,e}$. Thus, T_i (through $m_{1,i}$) undergoes appreciable decreases and the ratio $(T_i - T_w)/(T_e - T_w)$, despite reductions in T_w, decreases with increasing $(T_e - T_w)$. Therefore, in Figs. 3–5 and 6–8 the ratio q/q_{Nu} is seen to decrease with increasing $T_e - T_w$. Exceptions to these observed trends occur at high u_e (10 fps) and low $m_{2,e}$ (0.001), as shown in Figs. 3–5, and low u_e (0.1 fps) and high $m_{2,e}$ (0.1), as shown in Figs. 9 and 10. The former exception is due to the aforementioned drag effect which more than compensates for the reductions due to reduced values of $m_{1,i}$ (reduced T_i). The latter exception, which confirms the observations of Minkowycz and Sparrow [3], is somewhat more subtle. As illustrated in Fig. 13, the mass-transfer driving force $\mathcal{B}$ is seen to drop sharply as $T_e - T_w$ approaches zero when $m_{2,e}$ is large. Thus, q increases much more rapidly with $T_e - T_w$ as $m_{2,e}$ becomes larger than would be true at reduced $m_{2,e}$ (where $\mathcal{B}$ remains near its limit value $-m_{1,e}$). Upon normalizing q with respect to q_{Nu} (which exhibits a $(T_e - T_w)^{3/4}$-dependence), it is not surprising that q/q_{Nu} approaches zero with $T_e - T_w$. Furthermore, it is evident that the ratio must approach zero as $T_e - T_w$ becomes large. Thus, a maximum value is dictated provided $m_{2,e}$ is sufficiently large.

Acknowledgments

This work was supported by the State of California through the University of California Statewide Water Resources Center on Grant No. 4-442575-20537. Computer time for the numerical calculations was provided by the Campus Computing Network of the University of California, Los Angeles.

References

1 Sparrow, E. M. and Lin, S. H., "Condensation Heat Transfer in the Presence of a Noncondensable Gas," JOURNAL OF HEAT TRANSFER, TRANS. ASME, Series C, Vol. 86, No. 3, Aug. 1964, pp. 430–436.

2 Minkowycz, W. J., "Laminar Film Condensation of Water Vapor on an Isothermal Vertical Surface," PhD dissertation, University of Minnesota, 1965.

3 Minkowycz, W. J. and Sparrow, E. M., "Condensation Heat Transfer in the Presence of Noncondensables, Interfacial Resistance, Superheating, Variable Properties and Diffusion," *International Journal of Heat and Mass Transfer*, Vol. 9, 1966, pp. 1125–1144.

4 Rose, J. W., "Condensation of a Vapour in the Presence of a Non-condensing Gas," *International Journal of Heat and Mass Transfer*, Vol. 12, 1969, pp. 233–237.

5 Hampson, H., "The Condensation of Steam on a Metal Surface," *Proceedings, General Discussion on Heat Transfer*, Institution of Mechanical Engineers, 1951, pp. 58–61.

6 Meisenburg, S. J., Boarts, R. M., and Badger, W. L., "The Influence of Small Concentrations of Air in Steam on the Steam Film Coefficient of Heat Transfer," *Trans. AIChE*, Vol. 31, 1934, pp. 622–638.

7 Othmer, D. F., "The Condensation of Steam," *Industrial and Engineering Chemistry*, Vol. 21, 1929, pp. 577–583.

8 Slegers, L., "Condensation Heat Transfer on a Vertical Surface in the Presence of Noncondensable Gas," PhD dissertation, University of California, Berkeley, 1968.

9 Denny, V. E. and Mills, A. F., "Nonsimilar Solutions for Laminar Film Condensation on a Vertical Surface," *International Journal of Heat and Mass Transfer*, Vol. 12, 1969, pp. 965–979.

10 Mills, A. F. and Seban, R. A., "The Condensation Coefficient of Water," *International Journal of Heat and Mass Transfer*, Vol. 10, 1967, pp. 1815–1827.

11 Patankar, S. V. and Spalding, D. B., "A Finite Difference Procedure for Solving the Equations of the Two-Dimensional Boundary Layer," *International Journal of Heat and Mass Transfer*, Vol. 10, 1967, pp. 1389–1411.

12 Mason, E. A. and Monchik, L., "Survey of the Equation of State and Transport Properties of Moist Gases," 1963 International Symposium on Humidity and Moisture, National Bureau of Standards, Washington, D. C., 1963.

13 Hirschfelder, J. O., Curtiss, C. F., and Bird, R. B., *Molecular Theory of Gases and Liquids*, Wiley, New York, 1954.

14 Hilsenrath, J., *Tables of Thermodynamic and Transport Properties of Gases*, Pergamon Press, New York, 1960, also National Bureau of Standards Circular No. 564, 1955.

15 Keenan, J. H. and Keyes, F. G., *Thermodynamic Properties of Steam*, Wiley, New York, 1949.

16 Spalding, D. B., *Convective Mass Transfer*, McGraw-Hill, New York, 1963.

P. C. CHIU
Senior Lecturer.

K. L. POON
Lecturer.

Department of Mechanical Engineering,
University of Hong Kong,
Hong Kong

Frequency Response of Pool Boiling Plants

Dynamic analysis of a pool boiling plant is accomplished by using small perturbation technique. Mass and energy balance equations are established by basing on the dynamic model constructed and considering additional factors such as steam voids in the liquid phase, water droplets in the steam phase, and the heat transfer behavior at heating surface. Analytical methods for the steam void and dryness fraction dynamics are developed so that their approximate numerical solutions may be readily obtained. Two small boiler plants were constructed and experimental work was carried out by varying the heat input and the valve position in a sinusoidal manner. The experimental results of pressure, steam flow, and water level frequency responses were found to be in closer agreement with the analytical results obtained from the present model than those obtained from the simple mass and energy equations.

Introduction

Boiler control has become a critical problem because of the lack of understanding of the dynamical behavior of the boiler. As a result, the control problem is mainly solved by experience, and over-use of control equipment becomes inevitable. Previous workers [1–3][1] attempted to solve the boiler dynamic problem mainly by direct use of mass and energy equations. The transfer functions so derived are often represented by single time constants of exponential lags. Doubts have been raised whether such representation is sufficient to describe the main dynamics of a boiler. Furthermore, experimental evidence has been lacking to verify the theoretical analysis derived.

The present work focussed the attention on the dynamics of pool boiling processes which would find application for boiler drums and boiling water reactors. Small perturbation method is used throughout the analytical work, which reduces nonlinear differential equations into linear ones. This is justified since the plant control limits the pressure and temperature variations to a few percent except in starting and shutting-down conditions. The additional factors considered are steam voids in the water phase, water drops in the steam phase, overall effect of boiling heat transfer behavior, and the steam control valve characteristics. The analytical work on steam void dynamics has so far been an unexploited field. This is hardly surprising. Firstly, the interphase behavior between the steam and liquid phases is an unknown field. Secondly, no useful work has been performed on the bubble flashing and collapsing dynamics during the pressure transient, although a few experimental results have been obtained which only apply to particular situations. Thirdly, only empirical formulae are available for the boiling heat transfer behavior. Consequently, the work on steam void dynamics requires unavoidable assumptions so that the problem may be reasonably analyzed.

Mass and energy balance equations are established by including the above factors and basing on the dynamic model constructed. From these, the transfer functions of steam pressure, steam flow, and liquid level due to changes of heat input, feedwater, and control valve position may be established. The effect of various parameters on the boiler responses is clearly shown.

In the experimental work, it was decided that frequency response tests would give more complete information than that from transient response tests. Accordingly, two experimental boiler plants equipped with necessary measuring devices were built. Boiler output responses, such as steam pressure, steam flow rate, and liquid level, were recorded when the heat input or the control valve setting was varied sinusoidally.

Basic Mechanism of a Pool Boiling Process

A pool boiling plant is a two-phase thermodynamic system, in which the steam phase in general contains water drops, and the water phase contains saturated steam bubbles. Before the mathematical analysis of the boiling dynamics is attempted, the basic boiling mechanisms, particularly the interphase behavior, must be clearly stated and necessary assumptions made so that the mass and energy balance equations may be established.

The pressure in the drum will vary when disturbances occur in the flow rates of mass and energy in and out of the drum. The change in pressure will define a new equilibrium state for the two-phase mixtures. As the pressure increases, the steam temperature rises immediately corresponding to the new saturation pressure. Simultaneously, the water drop in the steam

[1] Numbers in brackets designate References at end of paper.

Contributed by the Heat Transfer Division for publication (without presentation) in the Journal of Heat Transfer. Manuscript received by the Heat Transfer Division December 10, 1969; revised manuscript received July 29, 1970. Paper No. 71-HT-A.

phase evaporates and absorbs energy, which slows down the rate of pressure increase. The water, due to its incompressibility, remains at the previous temperature, and becomes subcooled corresponding to the new pressure, while the bubble behaves identically as the steam. The temperature difference between the bubble and the bulk water causes condensation of steam inside the bubble. The heat energy released from the condensation is used to heat up the bulk water to the new saturation temperature. The phenomenon known as bubble collapsing also tends to retard the pressure increase. Conversely, as the pressure decreases the condensation of steam particles at the steam phase and the flashing of steam bubbles at the water phase will both reduce the rate of pressure decrease. It is clear, therefore, that for a given change of pressure, the bubbles in the water phase and the water droplets in the steam phase always change in such a way as to oppose the above pressure change. It is one of the purposes of the present investigation to determine the damping effect caused by the above two factors.

The water droplets in the steam phase may gain or lose mass corresponding to:

Nomenclature

a = circumference of heating surfaces (ft)
a_T = thermal diffusivity of boiling liquid (ft²/hr)
A = cross-sectional area of the drum at interphase (ft²)
A_H = heat transfer area of the heaters (ft²)
A_0 = cross-sectional area of subcooling zone (ft²)
B = coefficient, see reference [5]
B_L = coefficient related to steam properties, see reference [9]
C = coefficient expressed by equation (4)
C_D = specific heat of drum material (Btu/lb deg F)
C_H = specific heat of heater material (Btu/lb deg F)
C_l = specific heat of liquid (Btu/lb deg F)
D_b = diameter of a bubble just leaving the heating surface (ft)
f = bubble frequency (1/hr)
g = gravity (ft/hr²)
h_{as} = average enthalpy of the steam phase (Btu/lb)
$h_f{}^+$ = enthalpy of feedwater (Btu/lb) (60) (60)
h_{fg} = latent heat (Btu/lb)
h_l = enthalpy of saturated liquid (Btu/lb)
h_s = enthalpy of saturated steam (Btu/lb)
h_{sat} = enthalpy of saturated water (Btu/lb)
h_{sub} = enthalpy of subcooled water (Btu/lb)
H = see equation (33)
HT = heater
k_{fg} = coefficient expressed by $\partial h_{fg}/\partial P$ $\left(\frac{\text{Btu/lb}}{\text{lbf/ft}^2}\right)$
k_{hl} = coefficient expressed by $\partial h_{sat}/\partial P$ $\left(\frac{\text{Btu/lb}}{\text{lbf/ft}^2}\right)$
k_l = thermal conductivity of liquid $\left(\frac{\text{Btu}}{\text{hr ft deg F}}\right)$
k_T = coefficient expressed by $\partial T/\partial P$ (deg F/lbf/ft²)
$k_{\rho s}$ = coefficient expressed by $\partial \rho_s/\partial P$ $\left(\frac{\text{lb/ft}^3}{\text{lbf/ft}^2}\right)$
L = steam control valve movement (divisions)
m_b = bubble mass rate leaving the water phase (lb/hr)
m_{bi} = bubble mass rate into the water phase (lb/hr)
m_c = mass transfer rate between bubble and bulk water (lb/hr)
m_d = water droplet mass rate falling down to the water phase due to steam flow (lb/hr)
m_f = feedwater mass rate (lb/hr)
m_{fe} = evaporation or formation of water droplets inside the steam phase due to pressure variation (lb/hr)
m_g = mass rate leaving subcooled zone (lb/hr)
m_r = recirculating mass rate in the water phase (lb/hr)
m_{wd} = water droplet mass rate into the water phase due to coalescence (lb/hr)
m_{wr} = water droplet mass rate from the water phase due to ebullition (lb/hr)
$m_s{}^+$ = steam flow rate (lb/hr) (12) (14)
M_b = bubble mass in the water phase (lb)
M_D = mass of the steam drum (lb)
M_H = mass of heaters (lb)
M_1 = total mass in the water phase (lb)
M_0 = water mass in the part of subcooling zone below the heater (lb)
M_s = mass of steam in the steam phase (lb)
M_T = total mass in the steam phase (lb)
M_w = mass of water droplet in the steam phase (lb)
n = population of nucleation site
P^+ = drum pressure (lb/ft²) (3744) (6048)
P_i = pressure at the entrance of the steam control valve (lbf/ft²)
P_e = pressure at the exit of the steam control valve (lbf/ft²)
P_b = pressure inside the bubble (lbf/ft²)
P_l = pressure of the liquid (lbf/ft²)
P_v = pressure of vapor (lbf/ft²)
q_{H^+} = heat transfer rate to the bulk water per unit area of heating surface (Btu/ft² hr) (11888) (13180)
Q = heat rate supplied by heaters (Btu/hr)
Q_H = heat transfer rate from heating surface to the bulk water (Btu/hr)
R = bubble radius (ft)
s = Laplace transform operator
SP = arbitrary separator to define the dead water zone
t_0 = the instant when the bubble just leaves the heating surface (hr)
t_T = the instant when the bubble just leaves the water phase (hr)
T = temperature (deg F)
T_s = temperature of the steam (deg F)
T_{sur} = temperature at heating surface (deg F)
T_{sat} = temperature of saturating water (deg F)
v_l = specific volume of liquid (ft³/lb)
v_s = specific volume of steam (ft³/lb)
v_T = bubble terminal velocity (ft/hr)
V_b = total volume of bubbles in the water phase (ft³)
V_{bs} = volume of a single bubble (ft³)
$\bar{V}_{bs}$ = average volume of a single bubble in the water phase (ft³)
V_l = volume of the liquid phase (ft³)
V_s = volume of the steam phase (ft³)
x = dryness fraction in the steam phase
y = liquid level relative to the lower edges of heaters (ft)
$\bar{y}$ = average distance traveled by bubbles in the water phase (ft)
z = distance between the lower edges of the heater and the boiling boundary (ft)
α = bubble mass fraction M_b/M_1
α' = void fraction V_b/V_l
β = contact angle (deg)
σ = surface tension (lb/ft)
ρ_{as} = average density of the steam phase (lb/ft³)
ρ_{aw} = average density of the liquid phase (lb/ft³)
ρ_l = density of saturated water (lb/ft³)
ρ_s = density of steam (lb/ft³)
ρ_v = density of vapor (lb/ft³)
Υ_1 = time constant as shown in equation (28) (hr)
Υ_f = time constant as shown in equation (29) (hr)
Υ_y = time constant as shown in equation (30) (hr)
Δ = differential of
$^+$ = first numerical value for the horizontal-type boiler, and the second for the vertical-type boiler

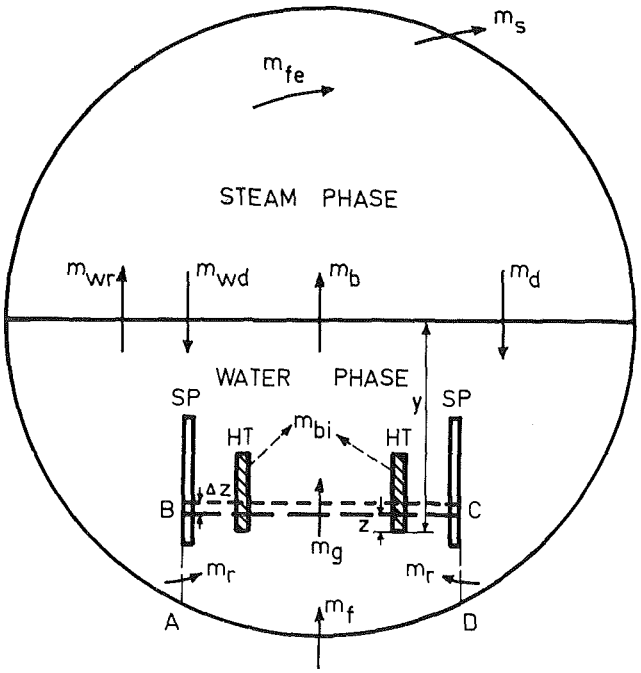

Fig. 1 Mass exchanges in a pool boiling plant

1 water droplets raised up due to ebullition m_{wr}

2 water droplets dropped down due to coalescence m_{wd}

3 formation or evaporation of water droplets due to pressure drop or rise respectively m_{fe}, and

4 water droplets falling down to the water phase due to steam flow m_d.

In the absence of a clear understanding of the interphase behavior, an assumption has to be made that the net energy and mass exchange at the interphase is the evaporation of bubble from the water phase to the steam phase; as the result

$$m_{wr} - m_{wd} - m_d = 0$$

The value of m_{fe} may be determined from mass and energy balance of the steam phase.

A Method of Predicting Steam Void Volume

A general analytical method for predicting the total steam void volume in a pool boiling plant has been lacking; even empirical formulae based on experimental methods have not been available. An approximate solution, however, may be developed by basing on the solutions for the individual bubble obtained by various workers. The following assumptions are made:

1 The bubble volume attaching at the heating surface is negligible.

2 The shape of a bubble is approximately spherical.

3 The bubble rises with a uniform terminal velocity.

4 When two or more bubbles coalesce to form a large bubble, its total volume is equal to the sum of that of all individual bubbles.

The equation of motion for a bubble of radius R in a nonviscous and incompressible liquid as a function of time is given by Rayleigh's equation

$$R\frac{d^2R}{dt^2} + \frac{3}{2}\left(\frac{dR}{dt}\right)^2 = \frac{P_v - P_l}{\rho_v} - \frac{2\sigma}{\rho_l R} \tag{1}$$

Equation (1) represents the law of mechanics relating the pressure force exerted by the bubble on the fluid to other forces, i.e., surface tension and inertia forces exerted by the fluid. The Clausius-Clapeyron equation connects the pressure difference to the temperature difference ΔT, i.e., the difference in temperature inside and at great distance from the bubble

$$(P_b - P_l) = \frac{h_{fg}}{T_s\left(\frac{1}{\rho_s} - \frac{1}{\rho_l}\right)}\Delta T \tag{2}$$

Forster and Zuber [4] obtained the approximate asymptotic solution for the growth of bubbles from equations (1) and (2) as

$$R = C\sqrt{t} \tag{3}$$

where

$$C = \frac{\rho_l\sqrt{\pi a_T}C_l(T_{\text{sur}} - T_{\text{sat}})}{h_{fg}\,\rho_s} \tag{4}$$

The term $(T_{\text{sur}} - T_{\text{sat}})$, or liquid superheat, is assumed constant. For a bubble with spherical shape its volume becomes

$$V_{bs} = \tfrac{4}{3}\pi C^3 t^{3/2} \tag{5}$$

The average size of the single bubble in the water phase may be given as

$$\bar{V}_{bs} = \frac{1}{t_T - t_0}\int_{t_0}^{t_T}\frac{4}{3}\pi C^3 t^{3/2}dt \tag{6}$$

The number of nucleate sites is given by Westwater [5] as

$$n = A_H\left(\frac{q_H}{B}\right)^2 \tag{7}$$

From equations (6) and (7), the total steam void volume may be formulated as

$$V_b = f(t_T - t_0)A_H\left(\frac{q_H}{B}\right)^2\bar{V}_{bs} \tag{8}$$

The value of $(t_T - t_0)$ may be calculated from the bubble terminal velocity which is given by Harmathy's empirical correlation [6] as

$$v_T = \frac{\bar{y}}{t_T - t_0} = 1.53\left(\frac{\sigma g}{\rho_l}\right)^{1/4} \tag{9}$$

Jakob [7] observed that the bubble frequency

$$f = \frac{920\ \text{ft/hr}}{D_b} \tag{10}$$

and D_b was found by Fritz [8] as

$$D_b = 0.01475\,\beta\sqrt{\frac{2\sigma}{g(\rho_l - \rho_s)}} \tag{11}$$

The total steam void volume therefore may be directly calculated from physical variables by substituting equations (9), (10), and (6) to (8).

Steam Void Dynamics

The steam void dynamics may be described by the change in bubble mass fraction α due to changes in various plant parameters influencing it. Basically, there are three ways that the void fraction may be changed. Firstly, the bubble mass in the water zone may be directly influenced by changing the heat transfer rate Q_H which alters the population of nucleation sites and $(T_{\text{sur}} - T_{\text{sat}})$, and the pressure which causes flashing or collapsing of bubbles. Secondly, the bubble mass may be indirectly influenced by changing the position of the boiling boundary BC as shown in Fig. 1. There are three parameters that are likely to alter the boiling boundary, i.e., the heat transfer

rate Q_H, the feedwater rate m_f, and the pressure P. Thirdly, the total mass of the water phase may be altered by changing the liquid level, which happens to change the bubble mass as well. Thus, the general equation of the steam void dynamics

$$\frac{d\alpha}{dt} = \left(\frac{\delta\alpha}{\delta P}\right)_{m_f,Q_H,y}\frac{dP}{dt} + \left(\frac{\delta\alpha}{\delta Q_H}\right)_{m_f,P,y}\frac{dQ_H}{dt} + \left(\frac{\delta\alpha}{\delta m_f}\right)_{Q_H,P,y}\frac{dm_f}{dt} + \left(\frac{\delta\alpha}{\delta y}\right)_{P,Q_H,m_f}\frac{dy}{dt} \quad (12)$$

Quantitative analysis of equation (12) is complex and may be achieved by further assumptions as follows:

1 Direct evaporating rate at the interphase is negligible in comparison with bubble mass rate.

2 During the pressure transient, the heat energy relieved from bubble collapsing or absorbed by bubble flashing is used to heat up or cool down the water to new saturation temperature.

3 The water level maintains a smooth surface.

4 The water phase is considered to have a uniform temperature T_l at the saturating zone and a uniform temperature T_{sub} at the subcooling zone.

5 The feedwater comes at a point below the heating surface; its temperature is constant and well below the boiling point.

6 Boiling heat transfer and mass exchange between bubble and bulk water take place instantaneously.

7 The cross-sectional area of the drum is constant for small variation of the water level.

8 Bubble velocity is constant.

Referring to Fig. 1 again, the water phase is divided into two zones, i.e., the saturating and subcooling zones. The latter is bounded by surfaces ABCD, the surfaces AB and CD are assumed to be fixed and the volume of the subcooling zone may only be varied by altering the position of the boiling boundary BC. The steam void dynamics may be studied by establishing the mass and energy balance equations for saturating and subcooling zones.

The bubble mass balance equation in the saturating zone is

$$\frac{d}{dt}(M_1\alpha) = m_{bi} - m_b - m_c \quad (13)$$

where m_c is considered positive for bubble collapsing and negative for bubble flashing. In differential form, the equation (13) becomes

$$M_1\frac{d\Delta\alpha}{dt} + \alpha A\rho_1\frac{d\Delta y}{dt} = \Delta m_{bi} - \Delta m_b - \Delta m_c \quad (14)$$

where

$$\Delta m_c = \frac{M_1 C_l}{h_{fg}} k_T \frac{d}{dt}(\Delta P) \quad (15)$$

steam coming out from the water phase

$$m_b = \frac{M_1\alpha}{(y-z)} v_T \quad (16)$$

and in differential form

$$\Delta m_b = \frac{M_1}{(y-z)} v_T \Delta\alpha + \left[\frac{\alpha v_T\rho_1 A}{(y-z)} - \frac{M_1\alpha v_T}{(y-z)^2}\right]\Delta y + \frac{M_1\alpha v_T}{(y-z)^2}\Delta z \quad (17)$$

also

$$\Delta m_{bi} = \frac{1}{h_{fg}}\Delta Q_H - \frac{Q_H}{h_{fg}^2}\Delta h_{fg} \quad (18)$$

Substituting equations (15), (17), and (18) to (14)

$$M_1\frac{d\Delta\alpha}{dt} + \alpha A\rho_1\frac{d\Delta y}{dt} = \frac{1}{h_{fg}}\Delta Q_H - \frac{Q_H}{h_{fg}^2}k_{fg}\Delta P - \frac{M_1 C_l}{h_{fg}}k_T\frac{d\Delta P}{dt} - \frac{M_1 v_T}{(y-z)}\Delta\alpha - \left[\frac{\alpha v_T\rho_1 A}{(y-z)} - \frac{M_1\alpha v_T}{(y-z)^2}\right]\Delta y - \frac{M_1\alpha v_T}{(y-z)^2}\Delta z \quad (19)$$

Mass balance of the subcooled zone

$$\rho_1 A_0\frac{dz}{dt} = m_f + m_r - m_g \quad (20)$$

Energy balance of the subcooled zone

$$\frac{d}{dt}(M_0 + \rho_1 A_0 z)h_{\text{sub}} = m_f h_f + m_r h_l - m_g h_l + q_H a z \quad (21)$$

Due to the large value of recirculating ratio (m_r/m_f), Δh_{sub} may be considered as zero. Substitute equation (20) to (21), eliminate m_r and m_g, and take the differential form

$$-\rho_1 A_0(h_l - h_{\text{sub}})\frac{d\Delta z}{dt} = -(h_l - h_f)\Delta m_f - m_f k_T\Delta P + q_H a\Delta z + a z\Delta q_H \quad (22)$$

Substitute equation (22) to (19) by eliminating Δz and take Laplace transform

$$M_1\left(\frac{1+\Upsilon_1 s}{\Upsilon_1}\right)\Delta\alpha = -\left[\frac{\alpha v_T\rho_1 A}{(y-z)} - \frac{M_1\alpha v_T}{(y-z)^2}\right](1+\Upsilon_y s)\Delta y + \frac{Q_H}{h_{fg}^2}k_{fg}\left(1 - \frac{M_1 C_l k_T h_{fg}}{Q_H k_{fg}}s\right)\Delta P - \frac{M_1\alpha v_T}{q_H a(y-z)^2}\frac{m_f k_T}{(1+\Upsilon_f s)}\Delta P + \left[\frac{1}{h_{fg}} - \frac{M_1\alpha v_T}{(y-z)^2} - \frac{z}{q_H A_H}\frac{1}{(1+\Upsilon_f s)}\right]\Delta Q_H - \left[\frac{M_1\alpha v_T}{(y-z)^2}\frac{(h_l - h_f)}{(1+\Upsilon_f s)q_H a}\right]\Delta m_f \quad (23)$$

Therefore

$$\frac{\Delta\alpha}{\Delta P} = \frac{\Upsilon_1}{1+\Upsilon_1 s}\left[\frac{Q_H k_{fg}}{M_1 h_{fg}^2}\left(1 - \frac{M_1 C_l k_T h_{fg}}{Q_H k_{fg}}s\right) - \frac{\alpha v_T}{q_H a(y-z)^2}\left(\frac{m_f k_T}{1+\Upsilon_f s}\right)\right] \quad (24)$$

$$\frac{\Delta\alpha}{\Delta Q_H} = \frac{\Upsilon_1}{1+\Upsilon_1 s}\left[\frac{1}{M_1 h_{fg}} - \frac{\alpha v_T}{(y-z)^2}\cdot\frac{z}{q_H A_H}\frac{1}{(1+\Upsilon_f s)}\right] \quad (25)$$

$$\frac{\Delta\alpha}{\Delta m_f} = -\frac{\Upsilon_1}{1+\Upsilon_1 s}\left[\frac{\alpha v_T}{(y-z)^2}\cdot\frac{(h_l - h_f)}{(1+\Upsilon_f s)q_H a}\right] \quad (26)$$

$$\frac{\Delta\alpha}{\Delta y} = -\frac{\Upsilon_1}{1+\Upsilon_1 s}\left[\frac{\alpha v_T\rho_1 A}{M_1(y-z)} - \frac{\alpha v_T}{(y-z)^2}\right](1+\Upsilon_y s) \quad (27)$$

where

$$\Upsilon_1 = \frac{(y-z)}{v_T} \quad (28)$$

$$\Upsilon_f = \frac{\rho_1 A_0(h_l - h_{\text{sub}})}{q_H a} \quad (29)$$

and

$$\Upsilon_y = \frac{\alpha A\rho_1}{\dfrac{\alpha v_T\rho_1 A}{(y-z)} - \dfrac{M_1\alpha v_T}{(y-z)^2}} \quad (30)$$

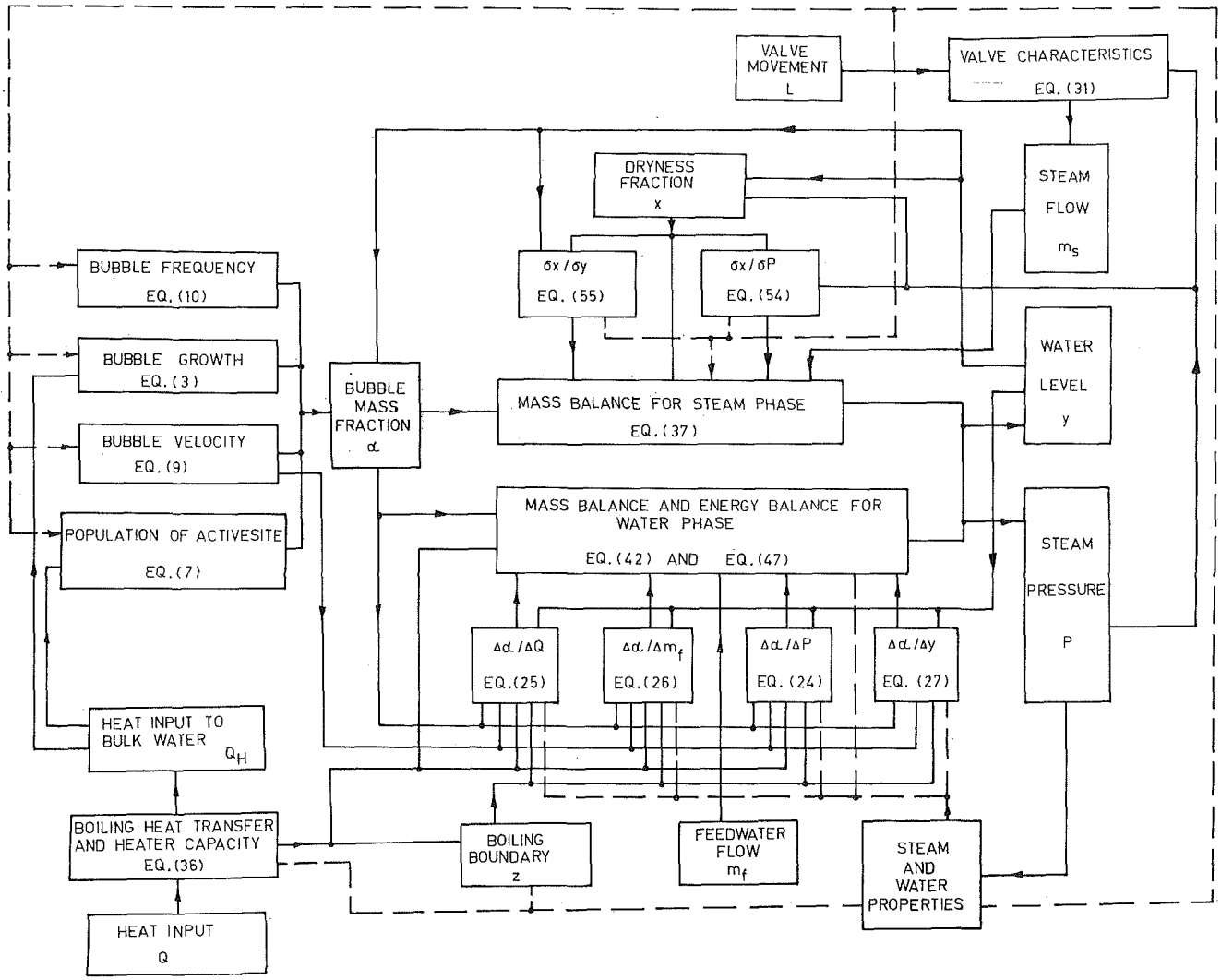

Fig. 2 Dynamic model of a pool boiling plant

Valve Characteristic Equation

The steady-state behavior of a steam control valve is well known. On the other hand, a fully satisfactory description of the dynamic behavior is still lacking. In general, the steam flow through the valve is dependent on the steam pressure before and after the valve, P_i and P_e, and valve stem position L. Thus

$$\Delta m_s = \left(\frac{\delta m_s}{\delta P_i}\right)\Delta P_i + \left(\frac{\delta m_s}{\delta P_e}\right)\Delta P_e + \left(\frac{\delta m_s}{\delta L}\right)\Delta L \quad (31)$$

where $\left(\frac{\delta m_s}{\delta P_i}\right)$, $\left(\frac{\delta m_s}{\delta P_e}\right)$, and $\left(\frac{\delta m_s}{\delta L}\right)$ are dependent on the geometrical factors of the individual valve and could be evaluated by experiments.

Dynamic Behavior of Heat Transfer Rate at Heating Surface

For simplicity, the Levy correlation [9] is employed in this investigation.

$$\frac{Q_H}{A_H} = H\frac{(T_{sur} - T_{sat})^3}{T_{sat}} \quad (32)$$

where

$$H = \frac{k_l C_l \rho_l^2}{\sigma(\rho_l - \rho_s)B_L} \quad (33)$$

On differentiating equation (32) and assuming that the boiling heat transfer is instantaneous, equation (32) becomes

$$\Delta Q_H = \frac{A_H H}{T_{sat}} 3(T_{sur} - T_{sat})^2(\Delta T_{sur} - \Delta T_{sat}) - \frac{A_H H(T_{sur} - T_{sat})^3}{T_{sat}^2} k_T \Delta P + A_H \frac{(T_{sur} - T_{sat})^3}{T_{sat}} \frac{\partial H}{\partial P}\Delta P \quad (34)$$

Energy balance in heating surface

$$\Delta Q - \Delta Q_H = M_H C_H \frac{d\Delta T_{sur}}{dt} \quad (35)$$

Combining equations (34) and (35)

$$\Delta Q_H = \frac{\Delta Q}{1 + \dfrac{M_H C_H}{\dfrac{A_H H}{T_{sat}}\, 3(T_{sur} - T_{sat})^2}\, s} - \frac{M_H C_H \left(\dfrac{(T_{sur} + 2T_{sat}}{3T_{sat}} - \dfrac{T_{sur} - T_{sat}}{3H} \dfrac{\partial H}{\partial P} \right) k_T s \Delta P}{1 + \dfrac{M_H C_H}{\dfrac{A_H H}{T_{sat}}\, 3(T_{sur} - T_{sat})^2}\, s} \quad (36)$$

Overall Mass and Energy Balance

A dynamic model for the boiling plant is constructed as shown in Fig. 2, in which the parameters influencing the mass and energy balance, the pressure, the steam flow, and the water level are clearly shown. Also, since the mass and energy exchanges at the interphase have been simplified and clearly defined, the mass and energy equations at steam and water phases may be established with the following assumptions:

1 The pressure is uniform throughout the steam and water phases.

2 There is no temperature gradient in the steam phase and the steam temperature instantaneously reaches saturation temperature corresponding to the pressure.

3 The turbulence of the steam is low and the heat transfer from the steam to the wall is negligible.

4 State equations for the steam phase are determined from the steam table and approximate the temperature, density, enthalpy, and pressure relation within a given range of values of these variables, i.e., linear relations between the aforementioned variables are obtained from the steam table.

5 The enthalpy of the water phase is equal to the saturated one corresponding to the pressure.

6 The drum wall always keeps at a temperature the same as the water phase temperature.

7 The kinetic energy of recirculating water is maintained constant.

8 Work done on bubble volume is negligible.

9 Heat lost through the drum is constant.

Steam phase mass balance

$$\frac{d}{dt}(\rho_{as} V_s) = m_b - m_s + m_{wr} - m_{wd} - m_d \quad (37)$$

Equation of state

$$\rho_{as} = \frac{\rho_s \rho_l}{x\rho_l + (1 - x)\rho_s} \quad (38)$$

On differentiating with respect to time and simplifying

$$\frac{d\rho_{as}}{dt} = \frac{x\rho_l^2 \dfrac{d\rho_s}{dt} + (\rho_s - \rho_l)\rho_s \rho_l \dfrac{dx}{dt}}{[x\rho_l + (1 - x)\rho_s]^2} \quad (39)$$

From interphase behavior

$$m_{wr} - m_{wd} - m_d = 0$$

For small changes in liquid level

$$\Delta V_s = -A\Delta y \text{ and } \Delta V_l = A\Delta y$$

Expand equations (37), substitute equation (39) to (37) and take Laplace transform

$$\frac{V_s \rho_l^2 x k_{\rho_s}}{[x\rho_l + (1 - x)\rho_s]^2} s\Delta P - \frac{V_s(\rho_l - \rho_s)\rho_s \rho_l}{[x\rho_l + (1 - x)\rho_s]^2} s\Delta x - \frac{\rho_s \rho_l A}{[x\rho_l + (1 - x)\rho_s]} s\Delta y = \Delta m_b - \Delta m_s \quad (40)$$

Steam phase energy balance

$$\frac{d}{dt}(M_T h_{as}) = (m_b - m_s)h_s + \frac{d(PV_s)}{dt} \quad (41)$$

Water phase mass balance

$$\frac{d}{dt}(\rho_{aw} V_l) = m_f - m_b - m_{wr} + m_{wd} + m_d \quad (42)$$

The average water density is given as

$$\rho_{aw} = \frac{\rho_s \rho_l}{\alpha\rho_l + (1 - \alpha)\rho_s} \quad (43)$$

where

$$\alpha = \frac{V_b \rho_s}{V_l[\rho_s \alpha' + (1 - \alpha')\rho_l]} \quad (44)$$

On differentiating with respect to time and simplifying

$$\frac{d\rho_{aw}}{dt} = \frac{\alpha\rho_l^2 \dfrac{d\rho_s}{dt} + (\rho_s - \rho_l)\rho_s \rho_l \dfrac{d\alpha}{dt}}{[\alpha\rho_l + (1 - \alpha)\rho_s]^2} \quad (45)$$

Expand equation (42), substitute equation (45) to (42) and take Laplace transform

$$\frac{V_l \rho_l^2 \alpha k_{\rho_s}}{[\alpha\rho_l + (1 - \alpha)\rho_s]^2} s\Delta P + \frac{V_l(\rho_s - \rho_l)\rho_s \rho_l}{[\alpha\rho_l + (1 - \alpha)\rho_s]^2} s\Delta\alpha + \frac{\rho_s \rho_l A}{[\alpha\rho_l + (1 - \alpha)\rho_s]} s\Delta y = \Delta m_f - \Delta m_b \quad (46)$$

Water phase energy balance

$$\frac{d(\rho_{aw} V_l h_l)}{dt} + M_D C_D \frac{dT_{sat}}{dt} = h_f m_f - Q_H - h_s m_b \quad (47)$$

Expand equation (47) and take Laplace transform

$$M_D C_D k_T s\Delta P + \frac{V_l \rho_l^2 \alpha k_{\rho_s} h_l}{[\alpha\rho_l + (1 - \alpha)\rho_s]^2} s\Delta P + \frac{V_l(\rho_s - \rho_l)\rho_s \rho_l h_l}{[\alpha\rho_l + (1 - \alpha)\rho_s]^2} s\Delta\alpha + \frac{\rho_s \rho_l A h_l}{[\alpha\rho_l + (1 - \alpha)\rho_s]} s\Delta y + \frac{V_l \rho_s \rho_l k_{hl}}{[\alpha\rho_l + (1 - \alpha)\rho_s]} s\Delta P = h_f \Delta m_f + \Delta Q_H - h_s \Delta m_b \quad (48)$$

Dynamic Behavior of Dryness Fraction

The steady-state value of the dryness fraction is dependent on the steam pressure, the liquid level, and the geometrical factors, and may be obtained from the experiments for the particular system. However, the dynamic behavior of the dryness fraction may be approached analytically with further assumptions as follows:

1 Evaporation and condensation of water droplets in the steam phase take place instantaneously corresponding to the pressure change.

2 Separation by the scrubber is perfect.

3 The dryness fraction is uniform in the steam phase.

In general, the dynamic behavior of the dryness fraction may be expressed as

$$\frac{dx}{dt} = \left(\frac{\delta x}{\delta P}\right)_y \frac{dP}{dt} + \left(\frac{\delta x}{\delta y}\right)_P \frac{dy}{dt} \quad (49)$$

From the definition of $x = M_s/M_T$

$$\frac{dx}{dt} = \frac{1}{M_T^2}\left(M_w \frac{dM_T}{dt} - M_T \frac{dM_w}{dt}\right) \quad (50)$$

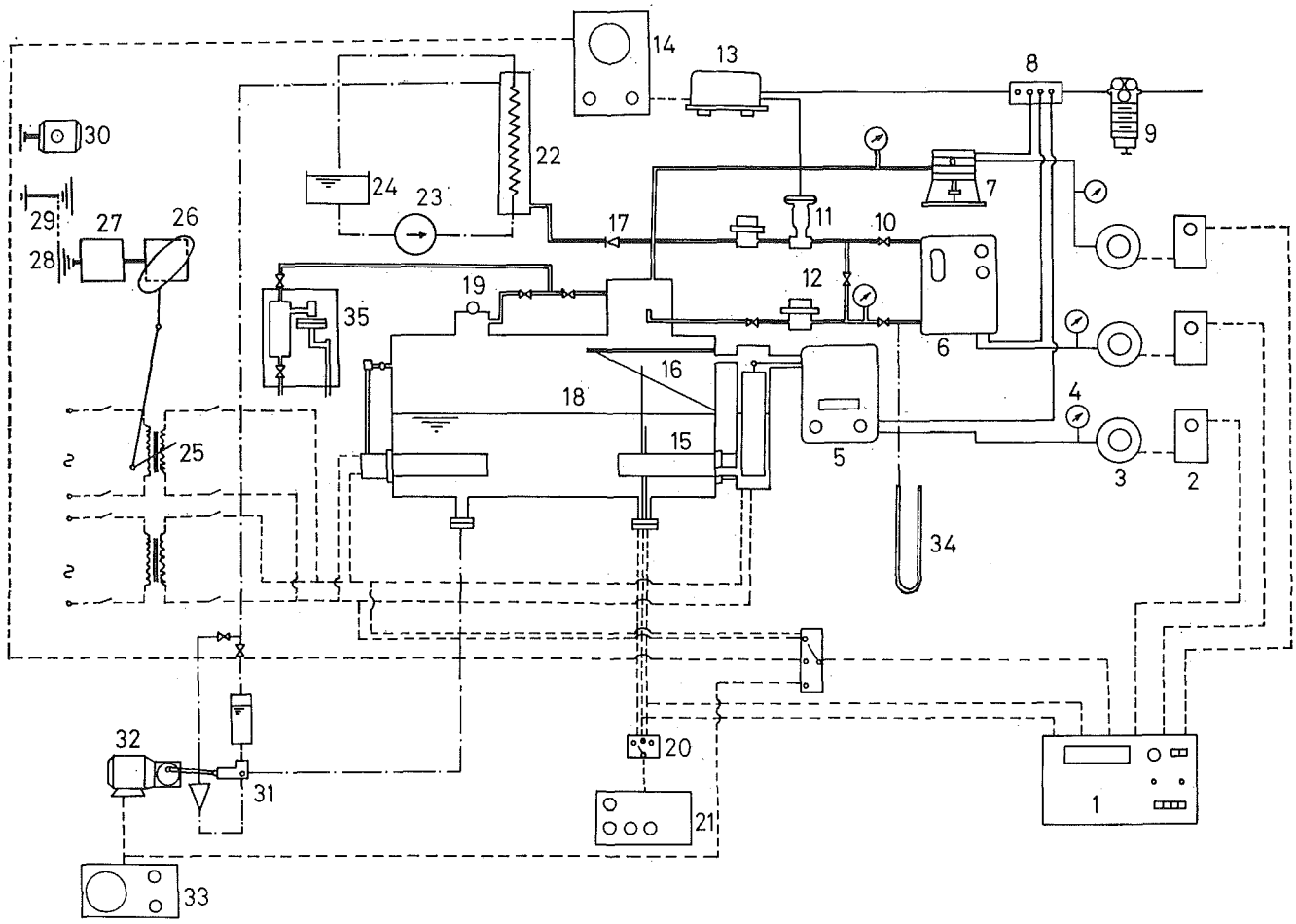

Fig. 3 Schematic layout of the test plant: 1 ultraviolet light recorder type SE.3006; 2 electrostatic charge amplifier model 566 multirange; 3 low-pressure quartz transducer; 4 standard air-pressure gauge; 5 displacement-type liquid-level instrument model 782; 6 V/A Thruflo meter series 10A 1430; 7 steam pressure transducer; 8 air distributor; 9 air regulator and filter; 10 steam valve; 11 pneumatic control valve; 12 pressure-reducing valve series 95; 13 electro-pneumatic transducer model 701T; 14 waveform generator feedback type TWG 300; 15 heater; 16 0.5-mm dia nickel-chromium/nickel-aluminum thermocouple; 17 steam check valve; 18 horizontal boiler; 19 safety valve; 20 thermocouple switch; 21 thermocouple test set; 22 condenser; 23 cooling water pump; 24 water tank; 25 variable transformer; 26 cam for sinusoidal heat input; 27 gear box; 28 V-belt pulley; 29 V-belts; 30 1-hp a-c single-phase motor; 31 feedwater pump; 32 d-c motor; 33 electronic motor speed control unit; 34 manometer; 35 separating and throttling calorimeter; ═══ steam flow; —— pneumatic path; - - - - - electrical wire; — · — · — water flow

Evaluate $\frac{dM_T}{dt}$ as in equation (40), and from the mass and energy balance equations (37) and (41)

$$\frac{dM_T}{dt} = \frac{V_s\rho_1^2 x k_{\rho_s}}{[x\rho_1 + (1-x)\rho_s]^2}\frac{dP}{dt} - \frac{V_s(\rho_1-\rho_s)\rho_s\rho_1}{[x\rho_1 + (1-x)\rho_s]^2}\frac{dx}{dt} - \frac{\rho_s\rho_1 A}{x\rho_1 + (1-x)\rho_s}\frac{dy}{dt} \quad (51)$$

and

$$\frac{dM_w}{dt} = \frac{1}{h_{fg}}\left(M_s\frac{\delta h_s}{\delta P} + M_w\frac{\delta h_l}{\delta P} - V_s\right)\frac{dP}{dt} - \frac{PA}{h_{fg}}\frac{dy}{dt} \quad (52)$$

Substitute equations (51) and (52) to (50) and rearrange

$$\frac{dx}{dt} = \left\{\frac{1}{1 + \frac{(1-x)V_s(\rho_1-\rho_s)\rho_s\rho_1}{M_T[x\rho_1 + (1-x)\rho_s]^2}}\right\}\left\{\frac{(1-x)V_s\rho_1^2 x k_{\rho_s}}{M_T[x\rho_1 + (1-x)\rho_s]^2} - \frac{1}{h_{fg}}\left[x\frac{\delta h_s}{\delta P} + (1-x)\frac{\delta h_l}{\delta P} - \frac{V_s}{M_T}\right]\right\}\frac{dP}{dt}$$

$$+ \left\{\frac{1}{1 + \frac{(1-x)V_s(\rho_1-\rho_s)\rho_s\rho_1}{M_T[x\rho_1 + (1-x)\rho_s]^2}}\right\}\left\{-\frac{PA}{M_T h_{fg}} - \frac{(1-x)\rho_s\rho_1 A}{M_T[x\rho_1 + (1-x)\rho_s]}\right\}\frac{dy}{dt} \quad (53)$$

Therefore

$$\frac{\delta x}{\delta P} = \left\{\frac{1}{1 + \frac{(1-x)V_s(\rho_1-\rho_s)\rho_s\rho_1}{M_T[x\rho_1 + (1-x)\rho_s]^2}}\right\}\left\{\frac{(1-x)V_s\rho_1^2 x k_{\rho_s}}{M_T[x\rho_1 + (1-x)\rho_s]^2} - \frac{1}{h_{fg}}\left[x\frac{\delta h_s}{\delta P} + (1-x)\frac{\delta h_l}{\delta P} - \frac{V_s}{M_T}\right]\right\} \quad (54)$$

$$\frac{\delta x}{\delta y} = -\left\{\frac{1}{1 + \frac{(1-x)V_s(\rho_1-\rho_s)\rho_s\rho_1}{M_T[x\rho_1 + (1-x)\rho_s]^2}}\right\}\left\{\frac{PA}{M_T h_{fg}} + \frac{(1-x)\rho_s\rho_1 A}{M_T[x\rho_1 + (1-x)\rho_s]}\right\} \quad (55)$$

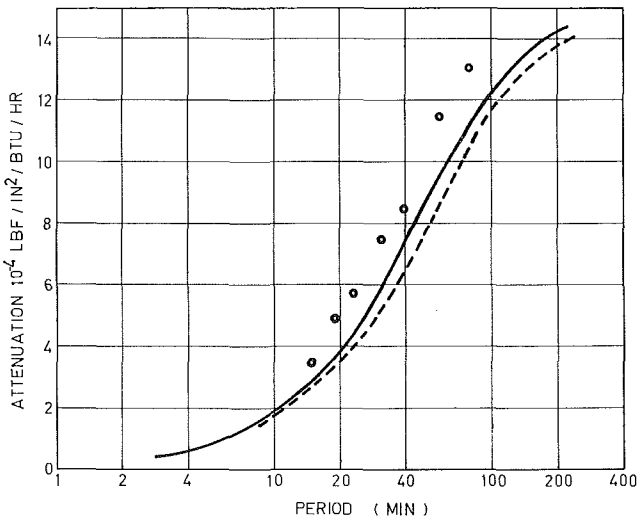

Fig. 4(a) Attenuation diagram for transfer function $\Delta P/\Delta Q$ for high liquid level; o o experimental result; —— theoretical result from the dynamical model; - - - - theoretical result from the simple mass and energy equations

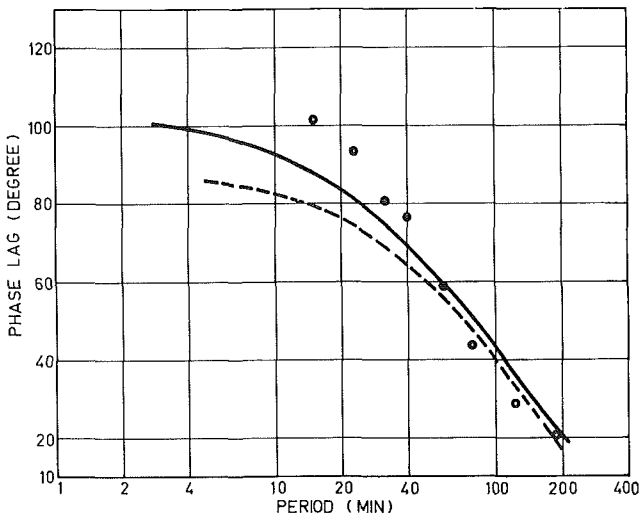

Fig. 4(b) Phase diagram for transfer function $\Delta P/\Delta Q$ for high liquid level; o o experimental result; —— theoretical result from the dynamical model; - - - - theoretical result from the simple mass and energy equations

Description of Apparatus

The general plant layout is shown in Fig. 3. A boiler of the horizontal-drum type with diameter 24 in. and length 40 in. was designed and constructed with a necessary safety valve and a direct water level indicator. The output steam passed through a steam cut-off valve, a pressure reducing valve, a pneumatically operated steam control valve, a V/A Thruflo meter for steam flow measurement, and was condensed in a tube-and-shell heat exchanger. The condensate was then driven back to the boiler by a feedwater pump. Thus, during the experiment, the water mass inside the boiler was practically maintained constant.

Heat input to the boiler was provided by four electric heaters, two of 4 kw each and the other two of 2 kw each. The output of two heaters with total capacity of 6 kw was enabled to vary in a sinusoidal manner by means of a specially designed mechanism consisting of a cam, two gear boxes, a 6-kva variable transformer with its output terminal connected to the two heaters, two series of V-belts, a 1-hp single-phase motor, and other accessories. The cam profile was designed in such a way that the output voltage of the transformer varied according to the square root of sine function. The power output of the heaters was thus varied with sine function, since power is proportional to the square of voltage output. The frequencies of sinusoidal inputs were achieved by various arrangement of the belt drive. The opening of the steam control valve was varied sinusoidally by means of an electrical waveform generator and an electropneumatic transducer.

The boiler outputs, i.e., the steam pressure and the steam flow rate, were measured by a steam pressure transmitter and a V/A Thruflo transmitter respectively. The outputs of the transmitters were both in pneumatic signals and were transduced to electric signals by means of two sets of piezo-transducers and electrostatic charge amplifiers. Input and output signals were simultaneously recorded by a 6-channel ultraviolet light recorder. A separating and throttling calorimeter was placed as shown in Fig. 3 to measure the steady-state dryness fraction.

Owing to the large ratio of the interphase cross-sectional area and the liquid level height, the liquid level responses due to the sinusoidal variation of heat input and control valve position were found to be negligibly small. A second vertical-type boiler of 5 in. by 9 in. in cross section and 8 ft in height was then constructed. Four heaters of total capacity 12 kw were fitted in two rows near the bottom of the boiler, and two glass windows of 12 in. in height were fitted to the sides of the boiler at about 6 ft from the bottom of the boiler. The liquid level responses were then taken by photographing the level positions through the glass window at regular intervals. All measuring instruments and accessories fitted to the previous boiler were used for this one except that the liquid level transducer was discarded.

Discussion of Results

Equations (23), (31), (36), (40), (46), (48), and (53) may be combined together to form transfer functions relating the inputs, i.e., heat input, steam valve position, and feedwater flow, to the outputs, steam pressure, steam flow, and liquid level. Numerical solutions of the transfer functions for the particular plants under testing are shown in Appendix 1. Analysis shows that the major dynamics of a pool boiling plant are provided by that of the water phase. This would be so even for a high-pressure plant. Exceptional cases are that the steam pressure is extremely high and water level low. In general, the transfer functions related to the steam pressure and the steam flow may be represented by three poles and one zero. The existence of second and higher poles and a zero is associated with the steam void dynamics in which the change of heat transfer rate ΔQ_H and particularly the change of pressure ΔP play the dominant parts. Referring to equation (24), one part of the void dynamics is that the variation of bubble mass fraction is proportional to the rate of change of pressure and the proportionality is a linear function of the bubble travel time in the water phase Υ_1. This term is a result of bubble collapsing and flashing during the pressure transient, and contributes one important damping effect to pressure response and swelling effect of the water level due to sudden control valve opening. The fact that the phase lags of theoretical frequency response curves exceed 90 deg is also mainly due to the existence of this term. Numerical analysis also shows that the parts of steam void dynamics due to change of the boiling boundary and change of water level are in general rather small except for extreme plant geometries. As the dryness fraction only influences the dynamics of the steam phase, the damping effect on the overall responses is again small and is clearly shown in equation (53).

Appendix 2 shows the equations from which the transfer functions may be derived by using the simple mass and energy balance. The frequency response curves obtained from both theories are plotted together with the experimental results and are illustrated in Figs. 4 to 8. Figs. 4 and 5 are the frequency

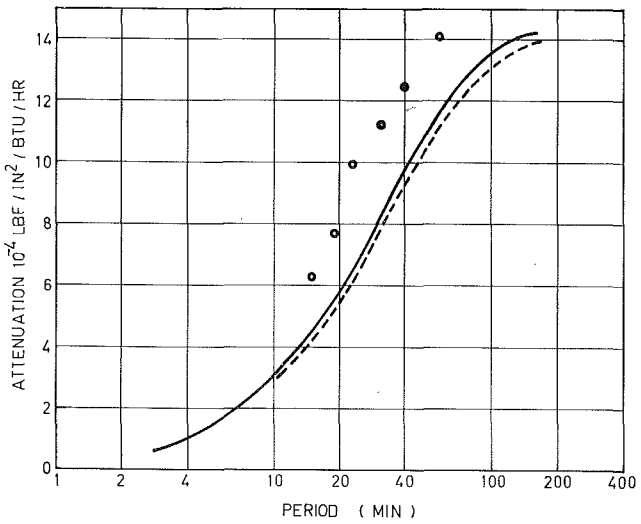

Fig. 5(a) Attenuation diagram for transfer function $\Delta P/\Delta Q$ for low liquid level

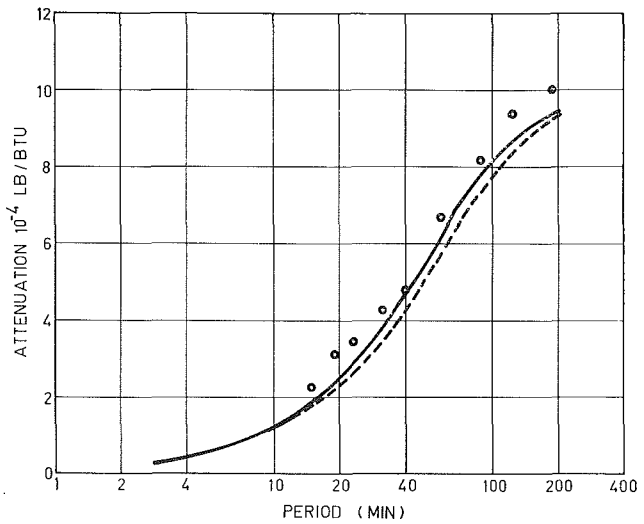

Fig. 6(a) Attenuation diagram for transfer function $\Delta m_s/\Delta Q$ for high liquid level

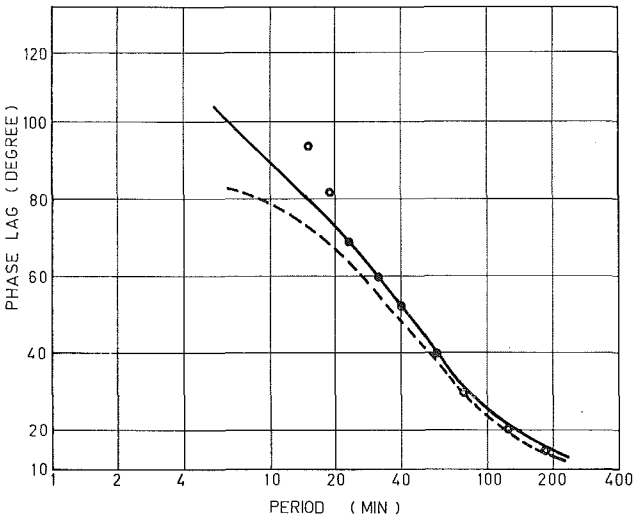

Fig. 5(b) Phase diagram for transfer function $\Delta P/\Delta Q$ for low liquid level

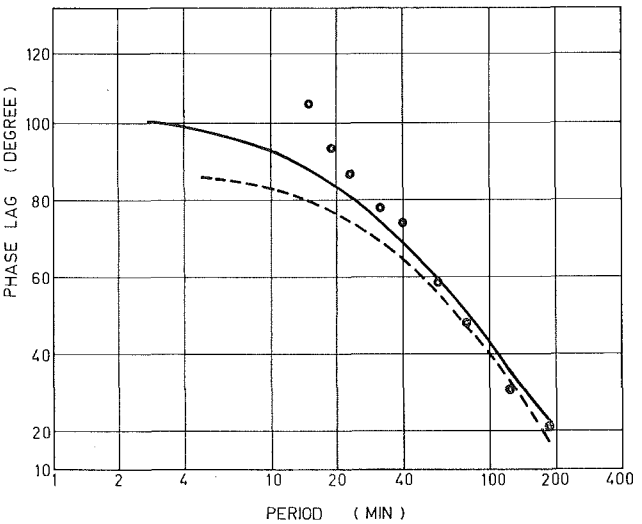

Fig. 6(b) Phase diagram for transfer function $\Delta m_s/\Delta Q$ for high liquid level

response curves of $\Delta P/\Delta Q$ at high and low levels respectively. The present theory agrees with the experimental results in that the phase lags exceed 90 deg at higher frequencies, but the experimental results show greater amplitude. Nevertheless, the curves from present theory are closer to the experimental ones. This suggests that other additional factors may exist but have not been accounted for in the present theory. One of them could be the boiling heat transfer dynamics due to changes of pressure and heat transfer rate ΔQ_H. The other could be the bubble growth dynamics due to change of pressure. However, the present knowledge of each is inadequate to make useful analysis on their dynamic behavior.

As shown in Fig. 7, the frequency response curves of $\Delta P/\Delta L$ obtained from the present theory agree closely with the experimental result. This indicates that the bubble flashing and collapsing are the dominant dynamics in comparison with those unaccounted for.

In order to demonstrate the effect of steam voids in the water phase on water level responses, experiments were conducted on the vertical-type boiler by varying the valve position sinusoidally and measuring water level responses. Fig. 8 shows the frequency response curves of $\Delta y/\Delta L$. The analytical results based on simple mass and energy balance show that water level responses are negligible. The analytical results based on the present theory tend to overestimate the water level amplitudes; this is due to the assumptions made in estimating the bubble volume, and particularly the assumptions that a bubble is spherical and the total bubble volume is the sum of individual bubbles. However, the important finding is that the present theory is able to predict the water level dynamics with reasonable accuracy, since the shape of experimental and analytical attenuation curves are similar and the phase curves are reasonably close. The fact that the theoretical phase curve shows phase-lead tendency indicates that the present theory is able to predict the swell effect of the water level when the control valve is suddenly opened. However, further study is necessary to improve its accuracy.

Conclusion

Theoretical analysis shows that the steam void, besides exerting a significant damping effect on the overall responses, is a dominant factor in estimating water level responses, but the damping effect of the dryness fraction is negligible. In general, the frequency responses derived from present theory are closer to the experimental results than those based on simple mass and

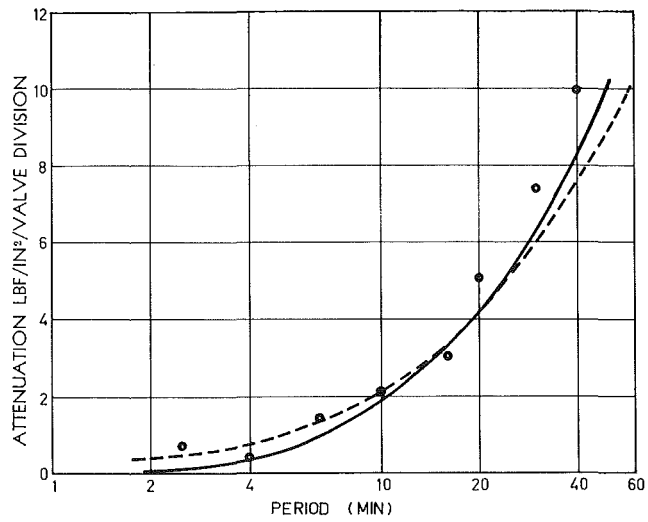

Fig. 7(a) Attenuation diagram for transfer function $\Delta P/\Delta L$ for high liquid level

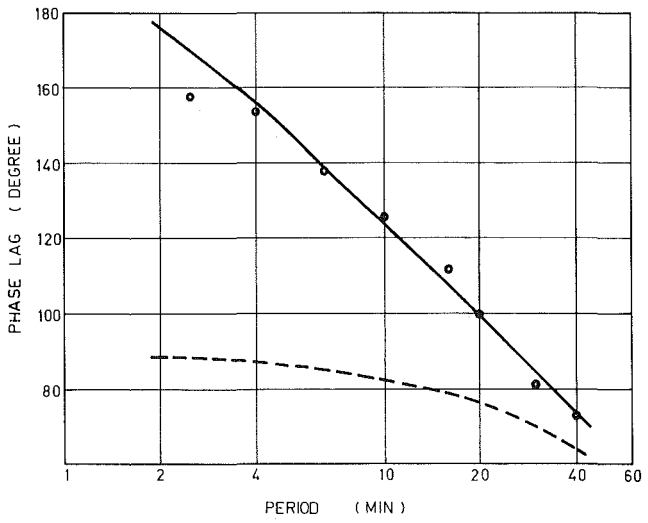

Fig. 7(b) Phase diagram for transfer function $\Delta P/\Delta L$ for high liquid level

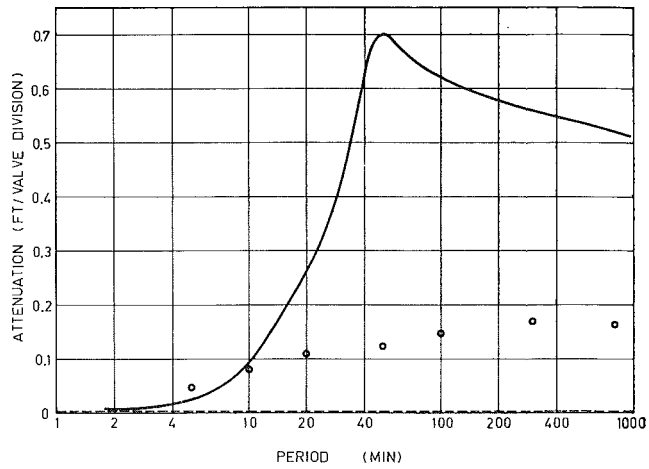

Fig. 8(a) Attenuation diagram for transfer function $\Delta y/\Delta L$ for the vertical-type boiler

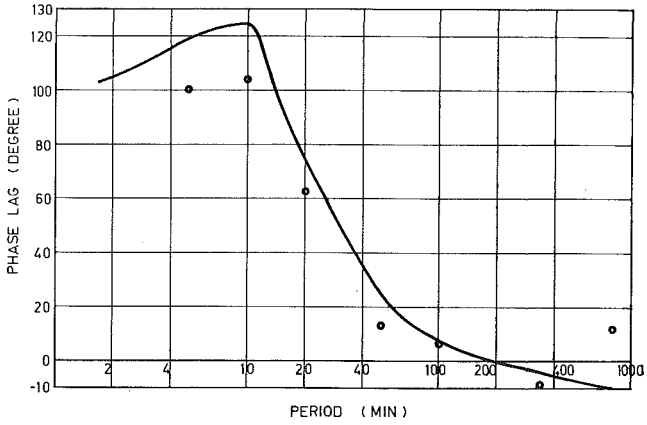

Fig. 8(b) Phase diagram for transfer function $\Delta y/\Delta L$ for the vertical-type boiler

energy balance, both in the low- and high-frequency regions, and particularly for the case of rapid steam valve opening or closing during which the bubble flashing or collapsing contributes important dynamics to the overall responses. The dynamic model tends to overestimate the amplitudes of water level responses; this is mainly due to the assumptions made in calculating the bubble volume in the water phase.

Acknowledgment

The project was financially supported by a research grant from the University of Hong Kong.

References

1 Chien, K. L., Ergin, E. I., et al., "Dynamic Analysis of a Boiler," TRANS. ASME, Vol. 80, 1958, pp. 1809–1819.

2 McPherson, P. K., "A Mathematic Model for Steam Drums," U. K. Atomic Energy Establishment, Winfrith Report No. 366.

3 Daniels, J. H., Enns, M., and Hottenstine, R. D., "Dynamic Representation of a Large Boiler Turbine Unit," ASME Paper No. 61-SA-69, 1961.

4 Forster, H. K., and Zuber, N., "Dynamics of Vapor Bubbles and Boiling Heat Transfer," *AIChE Journal*, 1955.

5 Gaertner, R. F., and Westwater, I. W., "Populations of Active Sites in Nucleate Boiling Heat Transfer," AIChE Preprint 105, 3rd National Heat Transfer Conference, 1959.

6 Harmathy, T. Z., "Velocity of Large Drops and Bubbles in Media of Infinite and Restricted Extent," *AIChE Journal*, Vol. 6, 1960, p. 281.

7 Jakob, M., and Linke, W., "Heat Transfer from a Horizontal Plate," *Forsh. Gebiet Ingenier*, Vol. 4, No. 2, 1933, pp. 75–81.

8 Fritz, W., "Maximum Volume of Vapor Bubbles," *Physikaliske Zeitshrift*, 1935, pp. 379–384.

9 Levy, S., "Generalized Correlation of Boiling Heat Transfer," JOURNAL OF HEAT TRANSFER, TRANS. ASME, Series C, Vol. 81, No. 1, Feb. 1959, pp. 37–42.

APPENDIX 1

Numerical Solutions for the Tested Plants

$$\frac{\Delta P}{\Delta Q} = \frac{16.64 \times 10^{-8}s^3 - 0.7 \times 10^{-4}s^2 + 0.105s + 1}{3.36 \times 10^{-8}s^5 + 2.92 \times 10^{-4}s^4 + 0.717s^3 + 117s^2 + 924s + 657.5}$$

$$\approx \frac{0.105s + 1}{0.717s^3 + 117s^2 + 924s + 657.5}$$

$$\frac{\Delta P}{\Delta L} = \frac{11598}{3.36 \times 10^{-8}s^5 + 2.92 \times 10^{-4}s^4 + 0.717s^3 + 117s^2 + 924s + 657.5}$$

$$\approx \frac{11598}{0.717s^3 + 117s^2 + 924s + 657.5}$$

$$\frac{\Delta m_s}{\Delta Q} = \frac{11.14 \times 10^{-8}s^3 - 0.469 \times 10^{-4}s^2 + 0.07s + 0.67}{3.36 \times 10^{-8}s^5 + 2.92 \times 10^{-4}s^4 + 0.717s^3 + 117s^2 + 924s + 657.5}$$

$$\approx \frac{0.07s + 0.67}{0.717s^3 + 117s^2 + 924s + 657.5}$$

For lower level

$$\frac{\Delta P}{\Delta Q} = \frac{0.337 \times 10^{-5}s^2 + 0.013s + 1}{0.856 \times 10^{-9}s^4 + 0.15s^3 + 27s^2 + 556.7s + 680.3}$$

$$\approx \frac{0.013s + 1}{0.15s^3 + 27s^2 + 556.7s + 680.3}$$

For the vertical-type boiler

$$\frac{\Delta y}{\Delta L} = \frac{0.16 \times 10^{-4}s^4 + 0.024s^3 + 11.73s^2 + 1905.6s + 4058}{0.09 \times 10^{-5}s^5 + 0.87 \times 10^{-3}s^4 + 0.31s^3 + 33s^2 + 3349s + 11130}$$

APPENDIX 2

Simple Mass and Energy Balance Equations Including the Heater Dynamics

1 Mass balance for the steam space

$$\frac{d}{dt}(V_s\rho_s) = m_b - m_s \tag{2.1}$$

Use small perturbation technique and, at equilibrium condition, put $m_b = m_s$

$$\therefore \rho_s \frac{d}{dt}\Delta V_s + V_s \frac{d}{dt}\Delta\rho_s = \Delta m_b - \Delta m_s$$

Put $\Delta V_s = -A\Delta y$, and $\Delta\rho_s = k_{\rho s}\Delta P$.

Assume A constant for small perturbation and take Laplace transform

$$-\rho_s A s\Delta y + V_s k_{\rho s} s\Delta P = \Delta m_b - \Delta m_s \tag{2.2}$$

2 Mass balance for the water space

$$\frac{d}{dt}(V_l\rho_l) = m_f - m_b \tag{2.3}$$

Put $\Delta V_l = A\Delta y$, assume A and ρ_l constant, and take differential

$$\rho_l A s\Delta y = \Delta m_f - \Delta m_b \tag{2.4}$$

3 Energy balance of the water phase

$$M_D C_D \frac{dT_{sat}}{dt} + \frac{d}{dt}(M_l h_l) = m_f h_f + Q - m_b h_s \tag{2.5}$$

Equation (2.5) assumes that the water and drum wall temperatures are equal to the saturation temperature T_{sat}. Again take differential form, and put $\Delta M_l = A\rho_l\Delta y$ and $\Delta h_l = k_{hl}\Delta P$.

$$M_D C_D k_{Ts}\Delta P + h_l\rho_l A s\Delta y + M_l k_{hl} s\Delta P = h_f\Delta m_f + \Delta Q - h_s\Delta m_b \tag{2.6}$$

4 Valve characteristic equation.

In general, the valve characteristic equation may be represented by equation (31). For the test boiling plants, $P_i = P$ and $P_e = 0$, and the valve characteristic equation may be expressed as

$$\left.\begin{aligned} \Delta m_s &= 0.00465\,\Delta P + 10\,\Delta L \quad \text{for high water level} \\ \Delta m_s &= 0.00493\,\Delta P + 10\,\Delta L \quad \text{for low water level} \end{aligned}\right\} \tag{2.7}$$

The transfer functions relating drum pressure, water level, and steam flow to the heat input, the valve position, and the feedwater rate may be obtained by solving equations (2.2), (2.4), (2.6), (2.7), and (36).

journal of heat transfer

discussion

Heat Transfer From the Rear of a Cylinder in Transverse Flow[1]

Nomenclature

d = cylinder diameter
M = upper bound for N_{Pe} introduced in equation (5)
N_{Nu} = Nusselt number, hd/k
N_{Pe} = Peclet number, dU/α
N_{Re} = Reynolds number, dU/ν
N_{Sr} = Strouhal number, d/UT
T = Strouhal cycle period
u = velocity characteristic of penetration depth δ, see equation (1)
U, U_∞ = main flow velocity
α = thermal diffusivity
δ = penetration depth ($\sim\sqrt{\alpha T}$)

M. Ghil.[2] The author presents a badly needed model for the heat transfer from the rear face of a cylinder. The model is that of penetration theory, exhibiting some points of similarity with the inviscid, potential flow solutions proposed recently for the heat transfer from cylinders and spheres to liquid metals (e.g., [11][3]). All these models arrive at a square-root dependence of the Nusselt number on the Peclet number ($N_{Nu} \sim N_{Pe}^{1/2}$).

Let us now take a closer look at the relevance of the model proposed to the problem at hand, which is defined (by the author's Fig. 1) for a range $N_{Re} = 10$–10^5.[4]

As pointed out by the author himself, the validity of the model relies most heavily upon two assumptions:

1 Molecular transport is predominant, which in turn implies that convection is negligible with respect to conduction, or

$$\delta u/\alpha \ll 1 \tag{1}$$

where δ is the penetration depth in one Strouhal (vortex-shedding) cycle T, u is a velocity characteristic of a region of thickness δ, and α is the thermal diffusivity.

2 The ratio of penetration depth as proposed by the author, $\delta = 4\sqrt{\alpha T}$, to eddy diameter, say $d/2$, is small

$$\delta/(d/2) \ll 1 \tag{2}$$

where d is the cylinder diameter. For the sake of simplicity, we shall also use, throughout the Reynolds number range involved, the author's equation (3) to eliminate T, implicit in (1) and (2)

$$T = \frac{d}{N_{Sr}U} = 5d/U \tag{3}$$

where $N_{Sr} = 0.2$ is the Strouhal number. Condition (2) obviously leads, substituting (3) into δ, to

$$N_{Pe} \gg 320 \tag{4}$$

Condition (1) poses a problem as to the ratio u/U, where U is the main flow velocity, but its form indicates that the Peclet number $N_{Pe} = dU/\alpha$ must be smaller than some quantity M,

$$N_{Pe} \ll M \tag{5}$$

which compared with (3) is rather puzzling. The measurements of Hanson and Richardson in air [12] show that for $N_{Pe} = 53{,}000$ and a distance from the cylinder $0.02d$, which is even smaller than the author's estimate for δ, $\delta = 4\sqrt{5}\, N_{Pe}^{-1/2}\, d \approx 0.04d$, the ratio of local mean to free-flow velocity $|U|/U_\infty$ (author's u/U) does not fall below 0.1. This result enables us to restate (5) expressing $\delta u/\alpha$ in (1) as

$$\frac{\delta u}{\alpha} = \frac{u}{U}\frac{\delta}{d}\frac{dU}{\alpha} = 0.1 \times 4\sqrt{5}\, N_{Pe}^{-1/2} \times N_{Pe} \ll 1 \tag{5a}$$

which yields

$$N_{Pe} \ll 1.25 \tag{6}$$

This stands in clear contradiction to (4), or leaves the range of applicability of the model void.

The paradox is easily explained if we consider the influence of U for given d and α. On the one hand

$$\delta/(d/2) = 8N_{Sr}^{-1/2}\sqrt{\alpha/d}\; U^{-1/2}$$

On the other

$$\delta/(\alpha/u) = 0.4N_{Sr}^{-1/2}\sqrt{d/\alpha}\; U^{1/2}$$

Indeed, if U increases, the ratio of penetration thickness to eddy diameter decreases as the Strouhal cycle shortens, whereas it stands to reason that the ratio of convection to conduction increases with increasing U. The underlying basic fact is that for "common" Prandtl numbers (gases and non-metallic liquids) viscous effects in the boundary layer, ignored by penetration theory, can not be neglected.

To conclude, we consider that a satisfactory theoretical explanation of the rather large and ever-increasing experimental knowledge of heat transfer in the separated region behind a cylinder in cross-flow is still to be given.

Additional References

11 Hsu, C.-J., "Analytical Study of Heat Transfer to Liquid Metals in Cross Flow Through Rod Bundles," *International Journal of Heat and Mass Transfer*, Vol. 7, 1964, pp. 431–446.

12 Hanson, F. B., and Richardson, P. D., "The Near-Wake of a Circular Cylinder in Crossflow," JOURNAL OF BASIC ENGINEERING, TRANS. ASME, Series D, Vol. 90, No. 4, Dec. 1968, pp. 476–484.

---

[1] By P. S. Virk, published in the February, 1970, issue of the JOURNAL OF HEAT TRANSFER, TRANS. ASME, Series C, Vol. 92, No. 1, pp. 206–207.

[2] Research Assistant, Faculty of Mechanical Engineering, Technion—Israel Institute of Technology, Haifa, Israel.

[3] Numbers in brackets designate Additional References at end of discussion.

[4] And for Prandtl numbers which are not very low (as in liquid metals). The latter are not included by the author in the experimental evidence cited and have to be discussed separately.

Lindon C. Thomas.[5] I would like to offer the following remarks regarding the technical brief by P. S. Virk entitled "Heat Transfer From the Rear of a Cylinder in Transverse Flow," in which he discussed the formulation of an eddy penetration model to heat transfer in the rear of a cylinder. This type model was adapted to turbulent mass transfer processes at a fluid-fluid interface by Danckwerts [13] in 1951 and has sometimes been known as the surface renewal and penetration model. Whereas Virk assumed that all eddies remain in contact with the surface for the same length of time, Danckwerts employed a random age distribution. Although the basic surface renewal and penetration model appears to be fairly representative of turbulent transport processes, difficulty has generally been encountered in the formulation of reasonable expressions for the period T. Virk assumed that eddies remain in contact with the rear surface of a cylinder for a period of time equal to the reciprocal of the shedding frequency f.

In regard to the significances of f, experimental evidence by Bellhouse and Schultz [14], Dimopolous and Hanratty [15], and Son and Hanratty [16] indicate that the vorticity oscillation has little effect on heat and mass transfer for flow past cylinders. These investigators reported the existence of sinusoidal oscillations of essentially constant frequency over the front portion of cylinders and irregular fluctuations superimposed upon periodic oscillations over the rear of the cylinders. However, the use of a splitter plate behind each cylinder was reported to have eliminated the regular sinusoidal fluctuations over the entire surface without appreciably altering the local transfer rates. Hence, some question arises concerning the validity of the assumption that the period T may be set equal to f.

It should further be pointed out that an identical analysis for heat transfer to a cylinder in transverse flow has been presented by Sano and Nishikawa [17]. (These investigators also considered the effect of surface curvature.) However, Sano and Nishikawa assumed that T can be set equal to f for the forward and rear surfaces. A similar analysis has also been applied to mass transfer to flow past a cylinder by Ototake [18]. This worker merely applied conventional boundary layer theory to the forward section of the cylinder and the surface renewal and penetration model as presented by Sano and Nishikawa and Virk to the turbulent region.

Additional References

13 Danckwerts, P. V., "Significance of Liquid-Film Coefficients in Gas Absorption," *AIChE Journal*, Vol. 43, 1951, p. 1460.

14 Bellhouse, B. J., and Schultz, D. L., "Determination of Mean and Dynamic Skin Friction, Separation and Transition in Low-Speed Flow with a Thin-Film Heated Element," *Journal of Fluid Mechanics*, Vol. 24, 1966, pp. 379–400.

15 Dimopoulos, H. G., and Hanratty, T. J., "Velocity Gradients at the Wall for Flow Around a Cylinder for Reynolds Numbers Between 60 and 360," *Journal of Fluid Mechanics*, Vol. 33, 1968, pp. 303–319.

16 Son, J. S., and Hanratty, T. J., "Velocity Gradients at the Wall for Flow Around a Cylinder at Reynolds Numbers from 5×10^3 to 10^5," Department of Chemistry and Chemical Engineering, University of Illinois, 1968.

17 Sano, Y., and Nishikawa, S., "Analysis of Heat Transfer of a Cylinder in Cross Flow Fluid by the Intermittent Penetration Theory," *Kagaku Kogaku*, Vol. 28, 1964, p. 10.

18 Ototake, N., "Forced Convection Transfer Coefficient from a Uniformly Concentrated Cylinder," *Kagaku Kogaku*, Vol. 32, 1968, p. 61.

[5] Associate Professor of Mechanical Engineering, University of Akron, Akron, Ohio.

Author's Closure

The author is grateful to Mr. Ghil and Professor Thomas for their comments.

Mr. Ghil correctly emphasizes, as did the original paper, that the assumptions involved in the eddy penetration model cause compensating errors. However, his analysis is seriously in error owing to his neglect of the variation in the deadwater to free-stream velocity ratio (u/U) with N_{Re}. Referring to air, $N_{Pr} \sim 1$, the data of Hanson and Richardson [12] show (u/U) of order 0.1 at N_{Re} $(\sim N_{Pe}) = 5.3 \times 10^4$ but at $N_{Re} = 10^4$, (u/U) is less than 0.02; data are unavailable at lower N_{Re} but those of Kovasznay [19] suggest $(u/U) < 0.01$ at $N_{Re} \sim 50$ while the numerical results of Son and Hanratty [20] show (u/U) of order 0.01 or less for $N_{Re} < 500$. In short, over the bulk of the N_{Re} range of interest, (u/U) is no greater than 0.01 so the ratio of convection to conduction, $[\delta u/\alpha] = (\delta/d)(u/U)(dU/\alpha) \sim 0.01\ (\delta/d)N_{Pe}$. By previous reasoning, the penetration distance $\delta \propto \sqrt{\alpha T}$ so $(\delta/d) = CN_{Pe}{}^{-1/2}$ and thence $[\delta u/\alpha] = 0.01\, CN_{Pe}{}^{1/2}$ where C is a proportionality constant. Now for conduction to exceed convection $[\delta u/\alpha] < 1$, whereas for penetration distance small with respect to eddy size $[\delta/d] < 1$ so the composite condition yielding the range of validity of the model is $C < N_{Pe}{}^{1/2} < 100/C$. The numerical value of C depends upon how one picks a penetration distance; if $\delta \sim 4\sqrt{\alpha T}$, as in the original, then $C \sim 9$ and the range of validity is $80 < N_{Pe} < 120$; however, $\delta \sim 4\sqrt{\alpha T}$ corresponds to a rather stringent accomplishment (>98 percent) of the temperature step and if a value $\delta \sim 2\sqrt{\alpha T}$ (~60 percent accomplishment) is chosen then the model is valid for $30 < N_{Pe} < 500$. Therefore, contrary to Ghil's assertions, both the main assumptions of the model should hold reasonably for a decade or so of N_{Pe} in the neighborhood $N_{Pe} \sim 100$.

In this connection it should further be pointed out that the eddy penetration concept stems from the physics of the shedding process regardless of the conductivity, whether molecular or turbulent, of the eddy. The molecular thermal conductivity is evidently appropriate at the lower end of the shedding regime, say $N_{Re} < 10^3$, so long as the shear layer shed stays essentially laminar, and in Fig. 1 of the original paper the theory based on this simplest of assumptions was shown to predict the order of magnitude of the transport from the rear face. At the upper end of the shedding regime, say $10^3 < \mathrm{Re} < 10^5$, the shear layer shed

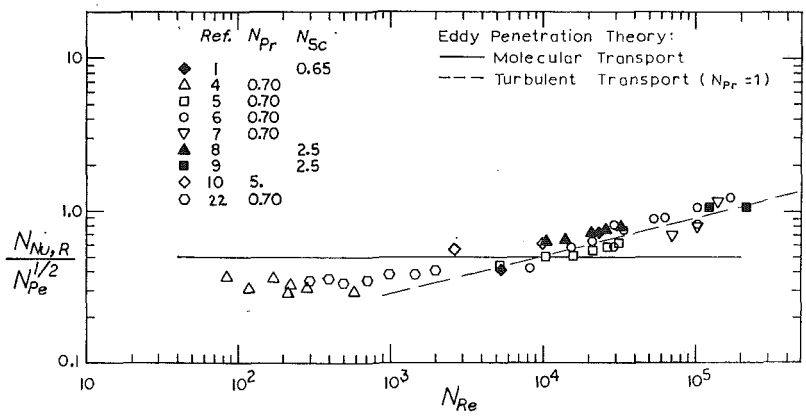

Fig. 1(a) Comparison of improved eddy penetration model with experimental data

becomes turbulent right from the separation point and in this regime the simple theory could be improved by employing a suitable "eddy" conductivity $\rho c\epsilon$ instead of k where ϵ is the eddy diffusivity (considered equal for momentum, heat, or mass transport). The previous logic then yields, in place of the original equation (4),

$$N_{\mathrm{Nu,R}} = 0.50 N_{\mathrm{Pe}}^{1/2}[\epsilon/\alpha]^{1/2} \tag{1}$$

The eddy diffusivity $\epsilon \sim v'l$ where v' and l are characteristic turbulent velocity and length scales; the turbulent intensity in a shear layer is of order 0.1 so $v' \sim 0.05U$ whereas l should be of the order of shear layer thickness, i.e., the momentum thickness Δ of the separating boundary layer. From boundary-layer theory [21], one has $(\Delta/d)N_{\mathrm{Re}}^{1/2} = 0.25$ at separation so

$$(\epsilon/\nu) = (v'l/\nu) \sim 0.05U\Delta/\nu = 0.01 N_{\mathrm{Re}}^{1/2} \tag{2}$$

whence, via (1),

$$(N_{\mathrm{Nu,R}}/N_{\mathrm{Pe}}^{1/2}) = 0.05 N_{\mathrm{Re}}^{1/4} N_{\mathrm{Pr}}^{1/2} \tag{3}$$

while the penetration criterion $(\delta/d) \sim N_{\mathrm{Re}}^{-1/4} \ll 1$ is also satisfied. Fig. 1(a) compares the improved eddy penetration model with experiment; the solid line represents the original model based on molecular transport while the dashed line represents equation (3) (with $N_{\mathrm{Pr}} = 1$ since most of the data refer to air) based on turbulent transport. In accordance with expectation, the trends of the experimental data are better followed by the former limiting cases (solid line) for $N_{\mathrm{Re}} < 10^3$ and by the latter limiting case (dashed line) for $N_{\mathrm{Re}} > 10^4$.

Professor Thomas rightfully questions the basic connection between the shedding process and the transport from the rear face. The evidence for this, while less than conclusive, consists of three basic observations: (a) hot-wire data, e.g., Collis and Williams [23], which show that the onset of shedding markedly increases the *overall* heat transfer and inasmuch as the shedding scarcely affects the transport on the leading face this implies a large increase in rear-face transport due to shedding, (b) frequency spectra of overall and local heat fluxes in the shedding regime are clearly dominated by contributions at the shedding frequency, and (c) if one considers the local heat transfer coefficient to consist of time-average and time-dependent components $\bar{h}$ and $\tilde{h}$ (the latter of frequency f) then the amplitude ratio $(\tilde{h}/\bar{h})$ tends to be small on the leading face but very much larger on the trailing face [10, 16].

Professor Thomas also notes that other workers [17] have accounted for the curvature of the cylinder surface. While I have not seen the work referenced, it is physically obvious that the curvature will have no effect at the short penetration time relevant to the present. Analytically, the respective expressions for time-average heat flux from the plane $x = 0$ to the region $0 < x < \infty$ and the cylindrical surface $r = (d/2)$ to the region $(d/2) < r < \infty$ are:

Plane:

$$q = \frac{2\theta k}{d\sqrt{\pi}} \left(\left[\frac{d^2}{\alpha T} \right]^{1/2} \right)$$

Cylindrical:

$$q = \frac{2\theta k}{d\sqrt{\pi}} \left(\left[\frac{d^2}{\alpha T} \right]^{1/2} + \frac{\sqrt{\pi}}{2} - \frac{1}{3} \left[\frac{\alpha T}{d^2} \right]^{1/2} + \cdots \right)$$

For penetration theory to apply $[d/\sqrt{\alpha T}] \gg 1$, in which case the bracket for the cylindrical surface is dominated by the leading term, making the two expressions equivalent.

Additional References

19 Kovasznay, L. S. G., *Proc. Royal Society*, Ser. A, Vol. 198, London, 1949, p. 174.

20 Son, J. S., and Hanratty, T. J., *Journal of Fluid Mechanics*, Vol. 35, 1969, p. 353.

21 Schlichting, H., *Boundary Layer Theory*, 4th ed., McGraw-Hill, New York, 1960.

22 Churchill, S. W., and Brier, J. C., *Chem. Eng. Prog. Symp. Series*, Vol. 51, No. 17, 1955, p. 57.

23 Collis, D. C., and Williams, M. J., *Journal of Fluid Mechanics*, Vol. 6, 1959, p. 357.

Surface Wetting Through Capillary Grooves[1]

P. R. Pujado[2] and L. E. Scriven.[3]

According to the paper by Bressler and Wyatt, the shape of a vapor–liquid interface in mechanical equilibrium in a capillary groove can be found by solving the equation

$$gz\Delta\rho = \sigma[z_{xx}(1 + z_x^2)^{-2} + z_{yy}(1 + z_y^2)^{-2}] \times [1 + z_x^2 + z_y^2]^{1/2} \tag{7}[4]$$

for the mathematical surface $z(x, y)$ subject to the following boundary conditions:

1 Along the vapor–liquid–solid phase boundary (contact line)

$$z_x \sin\phi - z_y \cos\phi = \cot\alpha \tag{8}$$

where α is the contact angle, taken as a constant, and ϕ is the angle between the horizontal x-direction and a horizontal tangent to the groove surface (see authors' Fig. 1).

2 In the vicinity of certain lines $y = 3d$ and $x = 3w/2$ (see authors' Fig. 1, where $y = 2d$), the vapor–liquid interface approaches the contour given by the authors' equation (5). This, it should be pointed out, is the well-known equation of the separating elastica [1].[5]

3 Along a certain centerline in the groove, $z_x = 0$ (authors' unnumbered equation), corresponding to the existence of a plane of symmetry. In addition, at the vertex ($x = 0$, $y = 0$) of a triangular groove, $z_y = -\cot\alpha$ (authors' unnumbered equation).

We find that the differential equation and first boundary condition are incorrect and that the third boundary condition is questionable in the case of a triangular groove.

The question of meniscus configuration in three dimensions is an important one and the corresponding mathematical problem is not a trivial one. Only recently have a few numerical solutions appeared, based on the method of local variations [2]. Owing to fairly widespread interest in the problem it is desirable to dispel any misconceptions or confusion the subject paper might produce. Standard references cited by the authors are silent in this area [3, 4].

The general equation of an interface in mechanical equilibrium is quite complex, unnecessarily so for most practical purposes [5]. By discarding terms that are usually unimportant one arrives at the time-honored Laplace-Young equation of capillarity:

$$2H\sigma = 2H_0\sigma + g(z - z_0)\Delta\rho \tag{D-1}$$

where z_0 and H_0 refer to a real or hypothetical reference point on the meniscus and H is the local mean curvature of the surface [6, 7]

$$H = \frac{1}{2}(\kappa_1 + \kappa_2) = \frac{1}{2}\left(\frac{1}{R_1} + \frac{1}{R_2}\right). \tag{D-2}$$

[1] By R. G. Bressler and P. W. Wyatt, published in the February, 1970, issue of the JOURNAL OF HEAT TRANSFER, TRANS. ASME, Series C, Vol. 92, No. 1, pp. 126–132.

[2] Research Assistant, Department of Chemical Engineering and Materials Science, University of Minnesota, Minneapolis, Minn.

[3] Professor, Department of Chemical Engineering and Materials Science, University of Minnesota, Minneapolis, Minn.

[4] Equations (7) and (8) are from the paper under discussion.

[5] Numbers in brackets designate References at end of discussion.

becomes turbulent right from the separation point and in this regime the simple theory could be improved by employing a suitable "eddy" conductivity $\rho c\epsilon$ instead of k where ϵ is the eddy diffusivity (considered equal for momentum, heat, or mass transport). The previous logic then yields, in place of the original equation (4),

$$N_{\mathrm{Nu,R}} = 0.50 N_{\mathrm{Pe}}^{1/2}[\epsilon/\alpha]^{1/2} \tag{1}$$

The eddy diffusivity $\epsilon \sim v'l$ where v' and l are characteristic turbulent velocity and length scales; the turbulent intensity in a shear layer is of order 0.1 so $v' \sim 0.05U$ whereas l should be of the order of shear layer thickness, i.e., the momentum thickness Δ of the separating boundary layer. From boundary-layer theory [21], one has $(\Delta/d)N_{\mathrm{Re}}^{1/2} = 0.25$ at separation so

$$(\epsilon/\nu) = (v'l/\nu) \sim 0.05U\Delta/\nu = 0.01 N_{\mathrm{Re}}^{1/2} \tag{2}$$

whence, via (1),

$$(N_{\mathrm{Nu,R}}/N_{\mathrm{Pe}}^{1/2}) = 0.05 N_{\mathrm{Re}}^{1/4} N_{\mathrm{Pr}}^{1/2} \tag{3}$$

while the penetration criterion $(\delta/d) \sim N_{\mathrm{Re}}^{-1/4} \ll 1$ is also satisfied. Fig. 1(a) compares the improved eddy penetration model with experiment; the solid line represents the original model based on molecular transport while the dashed line represents equation (3) (with $N_{\mathrm{Pr}} = 1$ since most of the data refer to air) based on turbulent transport. In accordance with expectation, the trends of the experimental data are better followed by the former limiting cases (solid line) for $N_{\mathrm{Re}} < 10^3$ and by the latter limiting case (dashed line) for $N_{\mathrm{Re}} > 10^4$.

Professor Thomas rightfully questions the basic connection between the shedding process and the transport from the rear face. The evidence for this, while less than conclusive, consists of three basic observations: (a) hot-wire data, e.g., Collis and Williams [23], which show that the onset of shedding markedly increases the *overall* heat transfer and inasmuch as the shedding scarcely affects the transport on the leading face this implies a large increase in rear-face transport due to shedding, (b) frequency spectra of overall and local heat fluxes in the shedding regime are clearly dominated by contributions at the shedding frequency, and (c) if one considers the local heat transfer coefficient to consist of time-average and time-dependent components $\bar{h}$ and $\tilde{h}$ (the latter of frequency f) then the amplitude ratio $(\tilde{h}/\bar{h})$ tends to be small on the leading face but very much larger on the trailing face [10, 16].

Professor Thomas also notes that other workers [17] have accounted for the curvature of the cylinder surface. While I have not seen the work referenced, it is physically obvious that the curvature will have no effect at the short penetration time relevant to the present. Analytically, the respective expressions for time-average heat flux from the plane $x = 0$ to the region $0 < x < \infty$ and the cylindrical surface $r = (d/2)$ to the region $(d/2) < r < \infty$ are:

Plane:

$$q = \frac{2\theta k}{d\sqrt{\pi}} \left(\left[\frac{d^2}{\alpha T} \right]^{1/2} \right)$$

Cylindrical:

$$q = \frac{2\theta k}{d\sqrt{\pi}} \left(\left[\frac{d^2}{\alpha T} \right]^{1/2} + \frac{\sqrt{\pi}}{2} - \frac{1}{3} \left[\frac{\alpha T}{d^2} \right]^{1/2} + \cdots \right)$$

For penetration theory to apply $[d/\sqrt{\alpha T}] \gg 1$, in which case the bracket for the cylindrical surface is dominated by the leading term, making the two expressions equivalent.

Additional References

19 Kovasznay, L. S. G., *Proc. Royal Society*, Ser. A, Vol. 198, London, 1949, p. 174.

20 Son, J. S., and Hanratty, T. J., *Journal of Fluid Mechanics*, Vol. 35, 1969, p. 353.

21 Schlichting, H., *Boundary Layer Theory*, 4th ed., McGraw-Hill, New York, 1960.

22 Churchill, S. W., and Brier, J. C., *Chem. Eng. Prog. Symp. Series*, Vol. 51, No. 17, 1955, p. 57.

23 Collis, D. C., and Williams, M. J., *Journal of Fluid Mechanics*, Vol. 6, 1959, p. 357.

Surface Wetting Through Capillary Grooves[1]

P. R. Pujado[2] and L. E. Scriven.[3]

According to the paper by Bressler and Wyatt, the shape of a vapor–liquid interface in mechanical equilibrium in a capillary groove can be found by solving the equation

$$gz\Delta\rho = \sigma[z_{xx}(1 + z_x^2)^{-2} + z_{yy}(1 + z_y^2)^{-2}] \times [1 + z_x^2 + z_y^2]^{1/2} \tag{7}[4]$$

for the mathematical surface $z(x, y)$ subject to the following boundary conditions:

1 Along the vapor–liquid–solid phase boundary (contact line)

$$z_x \sin\phi - z_y \cos\phi = \cot\alpha \tag{8}$$

where α is the contact angle, taken as a constant, and ϕ is the angle between the horizontal x-direction and a horizontal tangent to the groove surface (see authors' Fig. 1).

2 In the vicinity of certain lines $y = 3d$ and $x = 3w/2$ (see authors' Fig. 1, where $y = 2d$), the vapor–liquid interface approaches the contour given by the authors' equation (5). This, it should be pointed out, is the well-known equation of the separating elastica [1].[5]

3 Along a certain centerline in the groove, $z_x = 0$ (authors' unnumbered equation), corresponding to the existence of a plane of symmetry. In addition, at the vertex ($x = 0$, $y = 0$) of a triangular groove, $z_y = -\cot\alpha$ (authors' unnumbered equation).

We find that the differential equation and first boundary condition are incorrect and that the third boundary condition is questionable in the case of a triangular groove.

The question of meniscus configuration in three dimensions is an important one and the corresponding mathematical problem is not a trivial one. Only recently have a few numerical solutions appeared, based on the method of local variations [2]. Owing to fairly widespread interest in the problem it is desirable to dispel any misconceptions or confusion the subject paper might produce. Standard references cited by the authors are silent in this area [3, 4].

The general equation of an interface in mechanical equilibrium is quite complex, unnecessarily so for most practical purposes [5]. By discarding terms that are usually unimportant one arrives at the time-honored Laplace-Young equation of capillarity:

$$2H\sigma = 2H_0\sigma + g(z - z_0)\Delta\rho \tag{D-1}$$

where z_0 and H_0 refer to a real or hypothetical reference point on the meniscus and H is the local mean curvature of the surface [6, 7]

$$H = \frac{1}{2}(\kappa_1 + \kappa_2) = \frac{1}{2}\left(\frac{1}{R_1} + \frac{1}{R_2}\right). \tag{D-2}$$

[1] By R. G. Bressler and P. W. Wyatt, published in the February, 1970, issue of the JOURNAL OF HEAT TRANSFER, TRANS. ASME, Series C, Vol. 92, No. 1, pp. 126–132.

[2] Research Assistant, Department of Chemical Engineering and Materials Science, University of Minnesota, Minneapolis, Minn.

[3] Professor, Department of Chemical Engineering and Materials Science, University of Minnesota, Minneapolis, Minn.

[4] Equations (7) and (8) are from the paper under discussion.

[5] Numbers in brackets designate References at end of discussion.

Here $\varkappa_1$ and $\varkappa_2$ are the principal curvatures in mutually perpendicular directions tangent to the surface, and R_1 and R_2 are the corresponding radii of curvature. Twice the mean curvature, $2H$, is the trace of the curvature tensor, $\mathbf{b}$ (i.e., the first invariant of the curvature tensor [7]), and the surface divergence of the field of normals, $\mathbf{N}$, to the surface [8] (the minus sign appears by convention):

$$2H \equiv \text{trace } \mathbf{b} = -\nabla_{II} \cdot \mathbf{N}. \tag{D-3}$$

In cartesian coordinates the expression for $2H$ is *not* as in equation (7); rather, it is [6, 7]

$$2H = \nabla_2 \cdot \left[\frac{\nabla_2 z}{W}\right] = \frac{\partial}{\partial x}\left(\frac{z_x}{W}\right) + \frac{\partial}{\partial y}\left(\frac{z_y}{W}\right) \tag{D-4}$$

i.e.,

$$2H = \frac{z_{xx}[1 + z_y^2] - 2z_x z_y z_{xy} + z_{yy}[1 + z_x^2]}{[1 + z_x^2 + z_y^2]^{3/2}} \tag{D-5}$$

where

$$W = [1 + z_x^2 + z_y^2]^{1/2} \tag{D-6}$$

$$\nabla_2 = \mathbf{i}\frac{\partial}{\partial x} + \mathbf{j}\frac{\partial}{\partial y}. \tag{D-7}$$

In polar coordinates, which may be appropriate for analyzing menisci in triangular grooves, the correct expression is

$$2H = \frac{1}{r}\frac{\partial}{\partial r}\left[\frac{rz_r}{(1 + z_r^2 + r^{-2}z_\theta^2)^{1/2}}\right] + \frac{1}{r^2}\frac{\partial}{\partial \theta}\left[\frac{z_\theta}{(1 + z_r^2 + r^{-2}z_\theta^2)^{1/2}}\right]. \tag{D-8}$$

The contact angle is defined as the angle between respective normals to two interfaces at a point on the contact line in which they intersect [9]. If $\mathbf{n}$ is the normal to the solid surface, then the angle it makes with the normal to the interface $z(x, y)$ is given not by equation (8) but by

$$\cos \alpha = \mathbf{n} \cdot \mathbf{N} = \mathbf{n} \cdot \frac{\nabla_2 z}{W} = \frac{z_x \sin \phi - z_y \cos \phi}{(1 + z_x^2 + z_y^2)^{1/2}}. \tag{D-9}$$

At corners, including the vertex of a triangular groove, the contact angle is undefined but may be set equal to the contact angle made by the meniscus with each of two converging walls of identical wetting character, provided the meniscus actually reaches the corner between them. It is not generally true that $z_y = -\cot \alpha$ at the vertex of a triangular groove; rather, $z_y = -\cos \alpha/(\cos^2 \phi - \cos^2 \alpha)^{1/2}$, if the meniscus reaches the vertex. Furthermore, in a corner of angular opening 2β, a bounded solution of the Laplace-Young equation exists if

$$\alpha + \beta \geq \frac{\pi}{2}$$

but otherwise the solution is either unbounded or fails to exist. This was pointed out by Tyupsov, according to Petrov and Chernous'ko [2], who verified the fact by numerical computation. It was proved theoretically by Concus and Finn [10]. An early study of the corner meniscus was reported by Ferguson and Vogel [11]. A detailed treatment appeared recently [12]. All of these papers are relevant to the present problem.

Collective experience with numerical solutions of the Laplace-Young equation in three dimensions is still so limited that reports of new solutions should include details of the computational procedure and error studies.

In non-isothermal systems there is of course an added complication in that surface tension varies significantly with temperature. (Contact angle also depends on temperature, although only weakly in many cases [3].) Although this can be accommodated in the Laplace-Young equation, there are temperature fields in which it is impossible to establish a fluid interface at mechanical equilibrium: Flows driven by surface-tension gradients are bound to occur [13].

References

1 Greenhill, A. G., *The Application of Elliptic Functions*, 1892, Dover, 1959, pp. 87–89.

2 Petrov, V. M., and Chernous'ko, F. L., "Determining the Equilibrium Form of a Liquid Subject to Gravity Forces and Surface Tension," *Fluid Dynamics*, Faraday Press, Vol. 1, No. 5, 1966, pp. 109–112.

3 Adamson, A. W., *Physical Chemistry of Surfaces*, 2nd ed., Wiley Interscience, 1967.

4 Bikerman, J. J., *Surface Chemistry; Theory and Applications*, 2nd ed., Academic Press, 1958.

5 Murphy, C. L., "Thermodynamics of Low Tension and Highly Curved Interfaces," PhD thesis, University of Minnesota, Minneapolis, Minn., 1966.

6 McConnell, A. J., *Applications of Tensor Calculus*, Blackie, 1931, Dover, 1957, pp. 203–211.

7 Aris, R. A., *Vectors, Tensors, and the Basic Equations of Fluid Mechanics*, Prentice-Hall, 1962, pp. 26, 217–221.

8 Weatherburn, C. E., *Differential Geometry of Three Dimensions*, Cambridge University Press, 1939, pp. 264 ff.

9 Huh, C., and Scriven, L. E., "Hydrodynamic Model of Steady Movement of a Solid/Liquid/Gas Contact Line," *Journal of Colloid Interface Science*, Vol. 35, No. 1, 1971, pp. 85–101.

10 Concus, P., and Finn, R., "On the Behavior of a Capillary Surface in a Wedge," *Proceedings of the National Academy of Sciences*, Vol. 63, No. 2, 1969, pp. 292–299.

11 Ferguson, A., and Vogel, I., "On the 'Hyperbola' Method for the Measurement of Surface Tensions," *Proceedings of the Physical Society* (London), Vol. 38, 1925–26, pp. 193–203.

12 Concus, P., and Finn, R., "On a Class of Capillary Surfaces," *J. Analyse Math.*, Vol. 23, 1970, pp. 65–70.

13 Scriven, L. E., and Sterling, C. V., "The Marangoni Effects," *Nature*, Vol. 187, 1960, pp. 186–188.

Authors' Closure

The authors agree completely with the discussers that equation (7) of the paper is mathematically not correct, and that this point needs further clarification. In the derivation of equation (7), the curvatures were basically developed from intersections of the interfaces with planes which were parallel to the z-axis. Instead, a correct derivation should have been based on planes normal to the liquid–vapor interfaces, as outlined in the discussion by Pujado and Scriven, as well as in earlier analyses of related problems.

Since the angles between the planes normal to the surface and those parallel to the z-axis were usually small in the examined cases, the actual differences between curvatures computed from equation (D-5) of the discussion and from the simulating equation (7) of the paper were small enough to be neglected for the purpose of this study. Results from numerical evaluations of equation (7) have been compared with optical observations and photographs of menisci in capillary grooves on vertical planes. In particular, a "fully-wetted" height and other characteristic points have been experimentally located and measured for different fluids and surface materials. In addition, tests were made with transparent walls, colored fluids, and solidified interfaces to facilitate a better observation. Comparison of all available data showed fair agreement between the real interfaces and those computed from equation (7) of the paper. Supplementary details have been reported in *Journal of Basic Engineering*, TRANS. ASME, Series D, Vol. 93, No. 1, March 1971, pp. 87–89.

An Analytical Investigation of Free Convection Heat Transfer to Supercritical Water[1]

R. J. Simoneau[2] and R. C. Hendricks.[2]

The discussers agree that the authors' work is a logical extension of the work of Fritsch and Grosh [5] and should be done. The authors are to be com-

[1] By E. S. Nowak and A. K. Konanur, published in the August, 1970, issue of the JOURNAL OF HEAT TRANSFER, TRANS. ASME, Series C, Vol. 92, No. 3, pp. 345–350.

[2] Aerospace Research Engineer, NASA–Lewis Research Center, Cleveland, Ohio.

Here $\varkappa_1$ and $\varkappa_2$ are the principal curvatures in mutually perpendicular directions tangent to the surface, and R_1 and R_2 are the corresponding radii of curvature. Twice the mean curvature, $2H$, is the trace of the curvature tensor, $\mathbf{b}$ (i.e., the first invariant of the curvature tensor [7]), and the surface divergence of the field of normals, $\mathbf{N}$, to the surface [8] (the minus sign appears by convention):

$$2H \equiv \text{trace } \mathbf{b} = -\nabla_{II} \cdot \mathbf{N}. \tag{D-3}$$

In cartesian coordinates the expression for $2H$ is *not* as in equation (7); rather, it is [6, 7]

$$2H = \nabla_2 \cdot \left[\frac{\nabla_2 z}{W}\right] = \frac{\partial}{\partial x}\left(\frac{z_x}{W}\right) + \frac{\partial}{\partial y}\left(\frac{z_y}{W}\right) \tag{D-4}$$

i.e.,

$$2H = \frac{z_{xx}[1 + z_y^2] - 2z_x z_y z_{xy} + z_{yy}[1 + z_x^2]}{[1 + z_x^2 + z_y^2]^{3/2}} \tag{D-5}$$

where

$$W = [1 + z_x^2 + z_y^2]^{1/2} \tag{D-6}$$

$$\nabla_2 = \mathbf{i}\frac{\partial}{\partial x} + \mathbf{j}\frac{\partial}{\partial y}. \tag{D-7}$$

In polar coordinates, which may be appropriate for analyzing menisci in triangular grooves, the correct expression is

$$2H = \frac{1}{r}\frac{\partial}{\partial r}\left[\frac{rz_r}{(1 + z_r^2 + r^{-2}z_\theta^2)^{1/2}}\right] + \frac{1}{r^2}\frac{\partial}{\partial \theta}\left[\frac{z_\theta}{(1 + z_r^2 + r^{-2}z_\theta^2)^{1/2}}\right]. \tag{D-8}$$

The contact angle is defined as the angle between respective normals to two interfaces at a point on the contact line in which they intersect [9]. If $\mathbf{n}$ is the normal to the solid surface, then the angle it makes with the normal to the interface $z(x, y)$ is given not by equation (8) but by

$$\cos \alpha = \mathbf{n} \cdot \mathbf{N} = \mathbf{n} \cdot \frac{\nabla_2 z}{W} = \frac{z_x \sin \phi - z_y \cos \phi}{(1 + z_x^2 + z_y^2)^{1/2}}. \tag{D-9}$$

At corners, including the vertex of a triangular groove, the contact angle is undefined but may be set equal to the contact angle made by the meniscus with each of two converging walls of identical wetting character, provided the meniscus actually reaches the corner between them. It is not generally true that $z_y = -\cot \alpha$ at the vertex of a triangular groove; rather, $z_y = -\cos \alpha/(\cos^2 \phi - \cos^2 \alpha)^{1/2}$, if the meniscus reaches the vertex. Furthermore, in a corner of angular opening 2β, a bounded solution of the Laplace-Young equation exists if

$$\alpha + \beta \geq \frac{\pi}{2}$$

but otherwise the solution is either unbounded or fails to exist. This was pointed out by Tyupsov, according to Petrov and Chernous'ko [2], who verified the fact by numerical computation. It was proved theoretically by Concus and Finn [10]. An early study of the corner meniscus was reported by Ferguson and Vogel [11]. A detailed treatment appeared recently [12]. All of these papers are relevant to the present problem.

Collective experience with numerical solutions of the Laplace-Young equation in three dimensions is still so limited that reports of new solutions should include details of the computational procedure and error studies.

In non-isothermal systems there is of course an added complication in that surface tension varies significantly with temperature. (Contact angle also depends on temperature, although only weakly in many cases [3].) Although this can be accommodated in the Laplace-Young equation, there are temperature fields in which it is impossible to establish a fluid interface at mechanical equilibrium: Flows driven by surface-tension gradients are bound to occur [13].

References

1 Greenhill, A. G., *The Application of Elliptic Functions*, 1892, Dover, 1959, pp. 87–89.

2 Petrov, V. M., and Chernous'ko, F. L., "Determining the Equilibrium Form of a Liquid Subject to Gravity Forces and Surface Tension," *Fluid Dynamics*, Faraday Press, Vol. 1, No. 5, 1966, pp. 109–112.

3 Adamson, A. W., *Physical Chemistry of Surfaces*, 2nd ed., Wiley Interscience, 1967.

4 Bikerman, J. J., *Surface Chemistry; Theory and Applications*, 2nd ed., Academic Press, 1958.

5 Murphy, C. L., "Thermodynamics of Low Tension and Highly Curved Interfaces," PhD thesis, University of Minnesota, Minneapolis, Minn., 1966.

6 McConnell, A. J., *Applications of Tensor Calculus*, Blackie, 1931, Dover, 1957, pp. 203–211.

7 Aris, R. A., *Vectors, Tensors, and the Basic Equations of Fluid Mechanics*, Prentice-Hall, 1962, pp. 26, 217–221.

8 Weatherburn, C. E., *Differential Geometry of Three Dimensions*, Cambridge University Press, 1939, pp. 264 ff.

9 Huh, C., and Scriven, L. E., "Hydrodynamic Model of Steady Movement of a Solid/Liquid/Gas Contact Line," *Journal of Colloid Interface Science*, Vol. 35, No. 1, 1971, pp. 85–101.

10 Concus, P., and Finn, R., "On the Behavior of a Capillary Surface in a Wedge," *Proceedings of the National Academy of Sciences*, Vol. 63, No. 2, 1969, pp. 292–299.

11 Ferguson, A., and Vogel, I., "On the 'Hyperbola' Method for the Measurement of Surface Tensions," *Proceedings of the Physical Society* (London), Vol. 38, 1925–26, pp. 193–203.

12 Concus, P., and Finn, R., "On a Class of Capillary Surfaces," *J. Analyse Math.*, Vol. 23, 1970, pp. 65–70.

13 Scriven, L. E., and Sterling, C. V., "The Marangoni Effects," *Nature*, Vol. 187, 1960, pp. 186–188.

Authors' Closure

The authors agree completely with the discussers that equation (7) of the paper is mathematically not correct, and that this point needs further clarification. In the derivation of equation (7), the curvatures were basically developed from intersections of the interfaces with planes which were parallel to the z-axis. Instead, a correct derivation should have been based on planes normal to the liquid–vapor interfaces, as outlined in the discussion by Pujado and Scriven, as well as in earlier analyses of related problems.

Since the angles between the planes normal to the surface and those parallel to the z-axis were usually small in the examined cases, the actual differences between curvatures computed from equation (D-5) of the discussion and from the simulating equation (7) of the paper were small enough to be neglected for the purpose of this study. Results from numerical evaluations of equation (7) have been compared with optical observations and photographs of menisci in capillary grooves on vertical planes. In particular, a "fully-wetted" height and other characteristic points have been experimentally located and measured for different fluids and surface materials. In addition, tests were made with transparent walls, colored fluids, and solidified interfaces to facilitate a better observation. Comparison of all available data showed fair agreement between the real interfaces and those computed from equation (7) of the paper. Supplementary details have been reported in *Journal of Basic Engineering*, TRANS. ASME, Series D, Vol. 93, No. 1, March 1971, pp. 87–89.

An Analytical Investigation of Free Convection Heat Transfer to Supercritical Water[1]

R. J. Simoneau[2] and R. C. Hendricks.[2]

The discussers agree that the authors' work is a logical extension of the work of Fritsch and Grosh [5] and should be done. The authors are to be com-

[1] By E. S. Nowak and A. K. Konanur, published in the August, 1970, issue of the JOURNAL OF HEAT TRANSFER, TRANS. ASME, Series C, Vol. 92, No. 3, pp. 345–350.

[2] Aerospace Research Engineer, NASA–Lewis Research Center, Cleveland, Ohio.

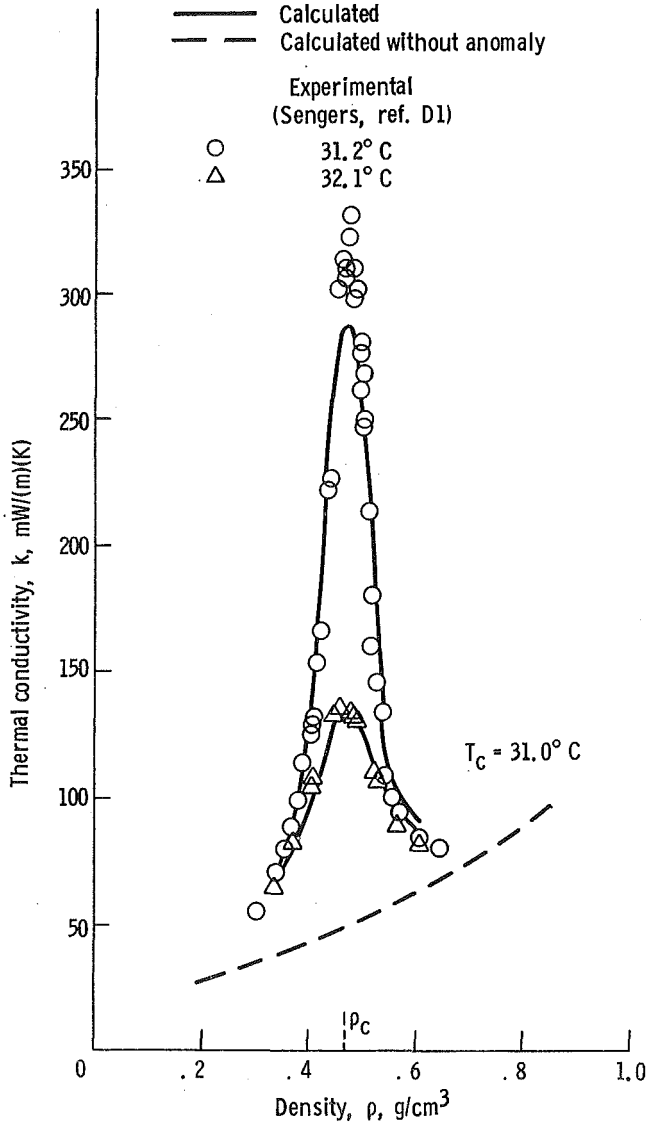

Fig. 1 Calculated and experimental thermal conductivities of carbon dioxide, from reference [18].

mended for basing their conclusions on the complete variable property results even though the partial variable property computations, using a free stream reference temperature, came closer to the data. The discussers agree, in general, with the authors' conclusions; however, they feel the paper could benefit from an expanded discussion in some areas. Specifically they would like to raise two questions.

First, have the authors made any attempt to take into account the anomalous spike that occurs in thermal conductivity near the critical point? The measurements of Sengers [13] in carbon dioxide show convincingly that the thermal conductivity peaks sharply in the near critical region. Subsequent measurements in argon [14], ammonia [15], methane [16], and hydrogen [17] have pretty well established the general occurrence of the phenomenon. While it has not to our knowledge been shown, there is no reason to believe the phenomenon does not occur in water. The absence of data, however, requires that the spike be computed—an admittedly difficult task. Brokaw [18] has successfully computed Sengers' data by treating the fluid as a dissociating polymer and the results are shown in Fig. 1. The computation requires an equation of state with accurate derivatives. For several fluids a recent equation of state by Bender [19] has been successfully employed in computing the spike [20], using Brokaw's theory. The discussers have no experience with water.

Very recently Sengers and Keyes [21] have published a scaling relationship for excess conductivity using Sengers' CO_2 data [13].

In the opinion of the discussers, if the influence of the anomalous spike is going to be important, it will be most important in free convection. Here the fluid dynamics are governed by the thermodynamics and the system is free to adjust to changes in thermal properties.

The second question is whether any computations were carried out with the free stream temperature below the transposed critical temperature? Since Fritsch and Grosh [3] report data with free stream temperature below the transposed critical temperature, it would be interesting to see the results of the partial variable property computations under these circumstances. The influence of the reference temperature might become clearer.

Additional References

13 Sengers, J. V., "Thermal Conductivity Measurements at Elevated Gas Densities Including the Critical Region," PhD thesis, University of Amsterdam, The Netherlands, 1962. (See also *Physica*, Vol. 28, pp. 1201–1264).

14 Bailey, B. J., and Kellner, K., "Thermal Conductivity of Argon Near the Critical Point," *British Journal of Applied Physics*, Vol. 18, 1967, pp. 1645–1647.

15 Golubev, I. F., and Sokolova, V. P., "The Thermal Conductivity of Ammonia at Various Temperatures and Pressures," *Thermal Engineering*, Vol. 11, No. 9, 1964, pp. 78–82.

16 Sokolova, V. P., and Golubev, I. F., "Thermal Conductivity of Methane at Different Temperatures and Pressures," *Thermal Engineering*, Vol. 14, No. 4, 1967, pp. 123–126.

17 Diller, D. E., and Roder, H. M., "Thermal Conductivity Measurements on Fluid Hydrogen at 17 to 200 K and Pressures to 100 Atm.," *Advances in Cryogenic Engineering*, Vol. 15, K. D. Timmerhaus, ed., Plenum Press, 1970, pp. 58–64.

18 Brokaw, Richard S., "Statistical Mechanical Theories of Transport Properties," presented at the International Conference on the Properties of Steam, Tokyo, Japan, Sept. 9–13, 1968. (NASA TMX-52478).

19 Bender, E., "Equations of State Exactly Representing the Phase Behavior of Pure Substances," *Proceedings of Fifth Symposium on Thermophysical Properties*, C. F. Bonilla, ed., ASME, New York, 1970, pp. 227–235.

20 Hendricks, R. C., Baron, A., Peller, I., and Pew, K. J., "GASP—A Properties Package for Eight Fluids—Helium, Methane, Neon, Nitrogen, Carbon Monoxide, Oxygen, Argon, Carbon Dioxide," paper submitted to the 13th International Congress of Refrigeration, Aug. 1971.

21 Sengers, J. V., and Keyes, P. H., "Scaling of the Thermal Conductivity Near the Gas-Liquid Critical Point," *Physical Review Letters*, Vol. 26, No. 2, 1971, pp. 70–73.

Authors' Closure

The senior author (E.S.N.) would like to thank the discussers for their review and thought-provoking remarks.

The authors have made no attempt to take into account the so-called anomalous spike in the thermal conductivity near the critical point, the reason for this being that as of this writing the spike in thermal conductivity has not been conclusively demonstrated for the case of steam. However, if the spike in fact exists for steam then the authors concur with the discussers that it could have a significant effect on free convection heat transfer.

The authors are initiating a study in which the plate temperature is higher than the transposed critical temperature and the free stream temperature is lower than the transposed critical temperature. The discussers are correct in stating that the influence of the reference temperature might become clearer.